Additive Manufacturing of Magnetocaloric Materials: Assessing and Adapting DLD and BJ3DP Fabrication Methods

by

Erica Stevens

B.S. in Materials Science and Engineering

University of Pittsburgh, 2015

Submitted to the Graduate Faculty of

the Swanson School of Engineering in partial fulfillment

of the requirements for the degree of

Doctor of Philosophy

University of Pittsburgh

2020

UNIVERSITY OF PITTSBURGH

SWANSON SCHOOL OF ENGINEERING

This dissertation was presented

by

Erica Stevens

It was defended on

October 6, 2020

and approved by

Markus Chmielus, Ph.D., Associate Professor, Department of Mechanical Engineering and Materials Science

Jörg Wiezorek, Ph.D., Professor, Department of Mechanical Engineering and Materials Science

Ian Nettleship, Ph.D., Professor, Department of Mechanical Engineering and Materials Science

Marc DeGraef, Ph.D., Professor at Carnegie Mellon University, Department of Materials Science and Engineering

Dissertation Director: Markus Chmielus, Ph.D., Associate Professor, Department of Mechanical Engineering and Materials Science

Additive Manufacturing of Magnetocaloric Materials: Assessing and Adapting DLD and BJ3DP Fabrication Methods

Erica Stevens, PhD

University of Pittsburgh, 2020

Solid-state cooling by means of magnetocaloric heat pumps is a promising alternative to current cooling technologies which are inefficient and environmentally-harmful. One major barrier to realizing the full potential of magnetocaloric heat exchangers is effective fabrication methods that enable geometric freedom while maintaining beneficial microstructures and combating the challenges these typically-brittle materials pose during machining. An ideal fabrication method would result in a heat exchanger with optimized heat transfer properties, low pressure drop in the heat transfer fluid, gradient transformation temperature, and reasonable manufacturing cost. Additive manufacturing has the capacity to realize all of these aims. This investigation explores the direct laser deposition and binder jet 3D printing additive manufacturing methods to produce functional parts using materials with magnetocaloric properties. Both direct laser deposition and binder jet 3D printing, after a necessary post-processing step, were found capable of producing parts with favorable magnetocaloric properties. A powder bed binder jet 3D printer was designed and fabricated to produce multi-material layered parts, with a goal of gradient transformation temperatures within a single part. Layering materials with various transformation temperatures extends the working temperature range and increases magnetocaloric heat exchanger performance. The results presented in this dissertation answer key technical questions about manufacturing process feasibility for fabricating magnetocaloric heat pumps with additive methods. Finally, an outlook is presented, collecting and examining the knowledge gained to predict the direction and prospects for additive manufacturing of magnetocaloric heat pumps.

Keywords: Magnetocaloric, Magnetic refrigeration, Additive manufacturing, Direct laser deposition, Binder jet, 3D printing.

Table of Contents

List of Tables

List of Figures

Preface

While I was writing this document, I asked Markus how to acknowledge the fact that this work was not wholly done by me. I consulted, I accepted advice, I absorbed others' expertise, and I led other researchers in efforts to collect or analyze data. He told me that though a dissertation has one name on it, it is the culmination of a long collection of knowledge. He said I am the center-brain, but there are strings connecting me to every person I've interacted with along the way who has given me a piece of their experience to help me: Chmielus Lab inhabitants, especially Amir Mostafaei, Jakub Toman, Katerina Kimes, Aaron Acierno, Rafael Rodriguez, Pierangeli Rodriguez, Jeff Martin, and Emma Dickinson; EHU/UPV and BCMaterials faculty, students, and employees including Volodymyr Chernenko, Daniel Salazar, Patricia Lázpita, Anabel Pérez, Jorge Feuchtwanger, and Iñaki Orue; PINSE NFCF staff including Esta Abelev, Mike McDonald, Susheng Tan, and Dan Lamont.

There are also those that contributed unending emotional support: my amazingly patient fiancé and partner in life - John Erickson - for going on a million walks so I could clear my head, letting me talk through my research, and being my daily inspiration; my parents Rich and Patty and sister Becca for providing a stable base of support and love; dear friends and role models like Dhanu, Jessica, and Sarah to whom I turned for a smile when my days were dreary; my editing guru Chris Dumm; and the many people I met and bonded with during my PhD program. Especially vital to my PhD adventures were the two organizations that I dedicated my heart to while my brain was preoccupied with research: the Pitt Engineering Graduate Student Organization (EGSO) and the Microscopy Society of America Student Council (MSA StC). In addition to providing essential leadership skills, EGSO and the MSA StC were where I found some of my greatest friends and mentors. The last five years would not have been the same without my fellow leaders: Alvaro and our early-years weekly meetings and life therapy sessions, Kevin with his persistent optimism and constant motivation during our virtual writing sessions, Stephanie sharing her unrelenting energy and drive, Janet spouting insightful wisdom and brilliant professionalism, and Cameron displaying direct practicality tempered with extreme caring. There are many others I had the privilege of interacting with and being inspired by through EGSO and MSA StC whose names could fill several pages.

The final thanks - I put off writing this the longest because words just never felt like enough - is to my advisor, Markus Chmielus. My senior year of undergrad, I hated research and never wanted to do it again. Then one day my overly-energetic lab professor came over to my friend group and turned an extra armchair sideways. He sat in it with his legs over the arm and happily asked if any of us wanted to work for him over the summer. I thought he seemed cool, and I thought “why not?”. I gave research one more chance because I thought maybe Markus could be the one to change my mind, and he did. His enthusiasm and never-ending curiosity helped me realize how exciting research can be. He taught me to re-frame problems as challenges, to not take setbacks too seriously, and to always look for the next mutually-beneficial collaboration. I have been through the entire evolution of Markus’s lab with him, and he has been through the full processes of my undergraduate thesis and dissertation work with me. He’s been professor, advisor, and friend. I cannot imagine my dissertation journey, or the last 6 years, without him.

Thank you all, from my center-brain to your brilliant minds and supportive hearts.

This project was supported in part by a fellowship award through the National Defense Science and Engineering Graduate (NDSEG) Fellowship Program, sponsored by the Air Force Research Laboratory (AFRL), the Office of Naval Research (ONR) and the Army Research Office (ARO). Partial results of this work have been accepted by Additive Manufacturing published by Elsevier (accepted August 2020) and are in preparation for submission to HardwareX published by Elsevier. Partial results have been published in the Journal of Manufacturing Science and Engineering published by ASME (online May 6, 2020) and are reprinted with the permission of the original publisher: E. Stevens, K. Kimes, V. Chernenko, P. Lázpita, A. Wojcik, W. Maziarz, J. Toman, M. Chmielus, Effect of Homogenization on the Microstructure and Magnetic Properties of Direct Laser-Deposited Magnetocaloric Ni43Co7Mn39Sn11, J. Manuf. Sci. Eng. 142 (2020) 1–8., reproduced with permission. In addition, related work has been published in the Supplement for Microscopy & Microanalysis published by Cambridge University Press (2016, 2018, 2019, and 2020). In each

of these publications, I was first author and had some level of direct participation in all of the research activities, through experimentation, analysis, or both. Gratitude is extended to Daniel Salazar for conducting the BJ3DP sample cycling direct MCE measurements, to Patricia Lázpita for DLD sample XRD analysis, and E3 beamline scientists for neutron diffraction experiments. For the design of the manual printer, special acknowledgement must go to Jeff Martin and Grant Merkel for their design and fabrication efforts. For some designs and efforts mentioned in the Future Works, many phenomenal Pitt Mechanical Engineering and Materials Science (MEMS) Senior Design teams (far too many names to list here) have earned the credit.

1.0 Introduction and Motivation

Refrigeration and space cooling are among the foremost contributors to electricity use in both domestic and commercial settings, with space cooling alone accounting for almost 20% of the world's total electricity use [1]. The World Energy Outlook 2019 report published by the International Energy Agency (IEA) predicts that "cooling is set to be one of the most important factors in determining the extent of future energy demand" [2]. According to the most recent World Energy Outlook report with detailed United States data (2017), 24.6% of electricity consumed by the US commercial sector was used for refrigeration/freezing. Refrigeration alone accounted for the largest percentage of annual electricity use in the commercial sector. This usage pattern is matched in residential electricity consumption; in US homes, space heating and refrigeration/freezing combined accounted for 24.2% of the total electricity consumption. On average, 14.3% of a home's electricity cost was from air conditioning ($27.28 billion cost for all US homes), and 5.5% was from refrigeration ($12.07 billion cost for all US homes) - a total of 19.8% of the average household's electricity bill stemming from cooling-related electricity [3]. There is a need for efficient refrigeration and cooling technologies that can contribute significantly to a decrease in future energy demand.

One promising solution for efficient cooling is the magnetic refrigeration process. In a magnetic refrigerator, the heat pump system contains a heat exchanger made from a solid-state magnetocaloric material which, in a simplistic view, spontaneously changes its temperature when exposed to a changing magnetic field. The incumbent and established vapor-compression refrigeration systems are relatively inefficient, achieving a stable 30-40% of Carnot efficiency (the theoretical maximum efficiency of a heat engine or refrigeration cycle that satisfies the second law of thermodynamics). In contrast, magnetic refrigeration has been theoretically shown to reach 60% of Carnot efficiency [4–6]. Improved efficiency (a higher coefficient of performance, in formal refrigeration terminology) naturally reduces energy consumption and thus marginal cost of use. An analysis by Shah et al. in 2015 calculated that a 30% improvement in global air conditioning performance, which could theoretically be achieved through magnetic refrigeration, would reduce electricity peak load by an amount equivalent to 710 mid-sized coal power plants [1, 7].

Vapor-compression refrigeration units also have environmental disadvantages including both noise pollution and ozone-depleting chemicals [1]. Though most consumers would not consider their home refrigerators to be loud, the quietest consumer refrigerators generate a sound pressure level around 48 dBA [8, 9]. The United States Environmental Protection Agency reported that above 45 dBA indoors, speech intelligibility is adversely impacted [10]. However, a 2007 study where participants qualitatively rated the acceptability of refrigerator noises found that a sound pressure level of 33 dBA was the threshold of annoyance [11]. By comparison, a modern magnetic refrigerator (MRS400, Ubiblue/Cooltech Applications, 2016) is marketed as generating noise below 35 dB, the approximate loudness of a whisper [12]. Beyond the relative annoyance of noise, the working fluids of vapor-compression refrigeration are detrimental to health and the environment: chlorofluorocarbons (CFCs) and hydrochlorofluorocarbons (HCFCs). These chemicals are toxic and have been found to contribute to a depleting ozone layer, and thus were regulated by the Montreal Protocol in 1987 [13]. Magnetic refrigeration requires no CFCs or HCFCs to operate, and can use fluids as innocuous as water or a water and salt mixture as a coolant.

While magnetic refrigeration is still an emerging technology as of 2020, several companies have debuted proof-of-concept systems and commercial products. The technical features, strengths, and weaknesses of a few of these systems are worth reviewing:

- General Electric Applications, before being purchased by Haier in 2016, used 50 stages (each stage using a magnetocaloric material to change the temperature of the fluid by a small amount) to reduce fluid temperatures by 80 °F (44 °C) overall. At that time, reduction in the number of stages required was a primary development topic [14].
- Cooltech Applications released a proof-of-concept commercial system in 2016 (MRS400) with 400 W of cooling power intended to keep temperatures between 35.6 °F and 41 °F (2 °C to 5 °C), safe for food storage. This machine was beta tested in three locations [12, 14, 15].
- Camfridge claims a 40% reduction in energy consumption for technology targeting small appliances, though they do not yet offer a commercial product [16].

- Cooltech Applications (now Ubiblue after Cooltech Applications declared bankruptcy in 2018) reported a prototype design in 2018 that boasted a temperature span of over 20 K and a cooling capacity of 15 kW. In this proof-of-concept design, 2 regenerators and 5.5 kg of magnetocaloric parallel-plate Gd and Gd alloys were used. [17].
- In 2018, Cooltech Applications and Vacuumschmelze GmbH published a paper detailing their promising experiments with LaFeSi-based magnetocaloric materials for magnetic refrigeration [18].

Recent estimates put commercialization of magnetic refrigeration technology about 5 years away [19]. Commercialization efforts are limited in part because materials with the physical properties that enable magnetic refrigeration are still relative unknowns in terms of functional mechanisms and practical, scalable use in applications. This work addresses the present uncertainty in optimal processing methods for a family of these materials. Increased familiarity with processing methods and the ability to repeatably fabricate these materials enables design of components for commercial-scale applications such as magnetic refrigerators. Since heat exchangers typically utilize a fluid flowing over the surface of a solid material to enhance heat transport, the processing and shaping of magnetic refrigeration materials into high surface-to-volume ratio configurations is a vital step towards realizing a maximum-efficiency magnetocaloric heat exchanger that can compete with the established vapor-compression systems [5, 20]. One way of achieving such configurations could be additive manufacturing which, along with magnetic refrigeration, was recognized as one of the *8 trends set to transform our industry* identified in the *Future Focus* May 2018 issue of HVAC&R Nation's magazine [21]. Elimination of vapor-compression technology allows for radical design changes that could be implemented by additive manufacturing, a fabrication technique that is lenient with geometry requirements and offers a great deal of design freedom.

2.0 Background

2.1 History

In 1860, William Thomson (Lord Kelvin) was the first to demonstrate that, thermodynamically, magnetization could change the temperature of a material [22]. The magnetocaloric effect (MCE) is often reported as being discovered in 1881 by Emil Warburg, and described in his German manuscript *Über einige Wirkungen Coërcivkraft* [23]. The discoverer is disputed; in 2013 Anders Smith argued that Pierre-Earnest Weiss and Auguste Piccard should be credited for the discovery of the MCE within the context of their work on nickel in 1917-1918 [24, 25]. In short, Smith argues that instrumentation in 1881 was not sophisticated enough to measure the effect, and Warburg's work simply laid the groundwork for the actual discovery of the MCE. Weiss and Piccard also coined the term *magnetocaloric* and were the first to observe the reversibility of the MCE and the fact that it peaks near the Curie temperature - both of which are vital to current exploitation of the effect.

In the 1920s, some work was done by Peter Debye and William Giauque - independently of each other - on the adiabatic demagnetization of paramagnetic salts, a concept related to the MCE [26, 27]. Neither was aware of Weiss and Piccard's work. By 1933, Giauque was able to demonstrate adiabatic demagnetization for temperatures as low as 1 K, winning him the Nobel Prize in Chemistry [28].

Urbain, Wiess, and Trombe reported in 1935 that gadolinium had a Curie temperature near room temperature, which led to G.V Brown developing a Gd-based room-temperature magnetocaloric material in 1976 [29, 30]. Brown's work invigorated research on magnetocaloric materials and was followed by a highly cited review and outlook article by Pecharsky and Gschneidner in 1999 [4].

2.2 Magnetism and the Magnetocaloric Effect

2.2.1 Magnetism Overview

Magnetism occurs because the quantum nature of electrons dictates that they have a magnetic field pointing either *up* or *down*. This magnetic dipole moment is caused by a combination of the electron's spin and its orbital angular momentum. With only one electron in the system, the contributions from the spin and from the orbital angular momentum interact, resulting in *spin-orbit coupling*. With more electrons, there are more interactions: spin-orbit coupling, spin-spin coupling, and orbit-orbit coupling. The overall magnetic behavior is calculated by vector addition [31].

There are several types of magnetism; simple examples include ferromagnetism and paramagnetism. A ferromagnetic material has magnetic moments that align with an applied field and each other, even when the field is removed. A paramagnetic material has randomized magnetic moments. These moments will tend to align with an applied field, but return to their initial randomized state when the field is removed. A magnetic material of any type loses its permanent magnetization and becomes paramagnetic above a temperature threshold known as the Curie temperature (T_C), which is a material property.

2.2.2 Thermodynamics of the Magnetocaloric Effect

Magnetic refrigeration is enabled through taking advantage of the magnetocaloric effect (MCE). The MCE refers to a physical phenomenon: a material exhibiting the MCE responds to a changing magnetic field with a sharp change in entropy. In an adiabatic system, this change in entropy can be characterized and measured as either a change in entropy ($\Delta S_{magnetic}$, ΔS_m, or ΔS_M) or as a change in temperature ($\Delta T_{adiabatic}$ or ΔT_{ad}).

In an adiabatic system, total entropy (S_{total}) is conserved. In broad terms, this entropy is the sum of a magnetic entropy ($S_{magnetic}$), thermal entropy arising from lattice vibrations ($S_{thermal}$), and an electronic entropy ($S_{electronic}$):

$$S_{total}(T, H) = S_{magnetic}(T, H) + S_{thermal}(T) + S_{electronic}(T) \tag{2.1}$$

Often, $S_{electronic}$ is negligible, since it and its relative change are generally very small [32, 33]. Equation 2.1 highlights the coupling between $S_{magnetic}$ and $S_{thermal}$ - if $S_{electronic}$ is considered to be quite small, and an external factor affects $S_{magnetic}$, then $S_{thermal}$ must either increase or decrease to compensate and keep S_{total} constant. This $\Delta S_{thermal}$ causes a change in material temperature (lattice vibrations). The simplest way for $S_{magnetic}$ to change is a realignment of magnetic moments upon introduction to the magnetic field, i.e. when the magnetic moments are caused to align due to an applied field, $S_{magnetic}$ decreases and $S_{thermal}$ increases. In most cases, the heating effect of this change in $S_{thermal}$ is practically undetectable and would not be useful for cooling applications.

However, the so-called *giant magnetocaloric effect* does create an easily detectable and useful change in material temperature through a combination of first and second order phase transitions, increasing energy density at the transformation [34]. First order phase transitions occur when there is a sudden change in the Gibbs free energy of the system, resulting in a discontinuity in the order parameter at the transition. Relevant to MCE materials, this order parameter could refer to magnetization, volume, heat capacity, or entropy [6, 35]. Second order phase transitions occur when the Gibbs free energy changes gradually (rather than suddenly, as in a first-order transition). Due to the gradual change in free energy, the order parameter is continuous all the way through the transition. In contrast with the previous example where $S_{magnetic}$ changed due to a realignment of magnetic moments - causing a second order magnetic transformation - the giant MCE is achieved through a magnetostructural phase transformation, a combination of first and second order transitions. In practical terms, this requires a coincident structural phase transition and Curie temperature.

There are two different types of giant MCE: positive and negative. In both, application of a magnetic field causes a shift of the first order phase transition temperature, expanding the temperature range of the more magnetic phase by shifting the transition temperature towards the less-magnetic phase. Positive MCE materials have a low-temperature highly magnetic phase, meaning that the application of a magnetic field causes a phase transition shift to higher temperatures. Negative MCE materials have a high-temperature highly magnetic phase, meaning that application of a magnetic field causes a phase transition shift to lower temperatures. These two types are described in thermodynamic detail in Sections 2.2.2.1 and

2.2.2.2. The existence of two types of MCE arises due to the entropic contributions mentioned in Equation 2.1. Though the thermal and magnetic entropy terms are inextricably coupled for a particular material, the type and magnitude of MCE that a material exhibits is dependent on whether these entropic contributions happen to be constructive or destructive [32, 36].

2.2.2.1 Positive MCE A material exhibiting a positive MCE heats up upon adiabatic magnetization and cools down upon adiabatic demagnetization.

The impact of positive MCE can be understood with a simple, highly visual example. Consider how the heat capacity changes in a positive MCE material with first-order phase transition when the material is shifted from a low magnetic field state (H_1) to a high magnetic field state (H_2). Magnetic entropy change is then the area between the heat capacity curves:

$$\Delta S_m(T)_{\Delta H,P} = \int_0^T \frac{[C(T)_{H_2} - C(T)_{H_1}]_P}{T} dT \tag{2.2}$$

where P indicates an isobaric process, $\Delta H = H_2 - H_1$, and $H_2 > H_1$. Equation 2.2 was derived from the second law of thermodynamics in [37].

In a material that exhibits the positive MCE, an application of magnetic field shifts the first order phase transition to a higher temperature. Consequences of this transition temperature shift on the heat capacity and ΔS_m are shown in Figure 2.1.

In order to understand the ramifications of this shift in the heat capacity curve, Figure 2.1 can be separated into five segments (pt refers to phase transition):

1. $0 - T_{pt,H_1}$: Heat capacity *with field* and *without field* are almost the same, though heat capacity with field is slightly lower. The integral between low and high field curves is slightly (but increasingly) negative.
2. T_{pt,H_1}: Heat capacity for the *without field* curve reaches its transition point. In the ideal case, the material transforms instantaneously and produces an infinitely high peak in C_p. In a real material, there will be a finite peak with a finite but large (negative) integral between low and high field curves.

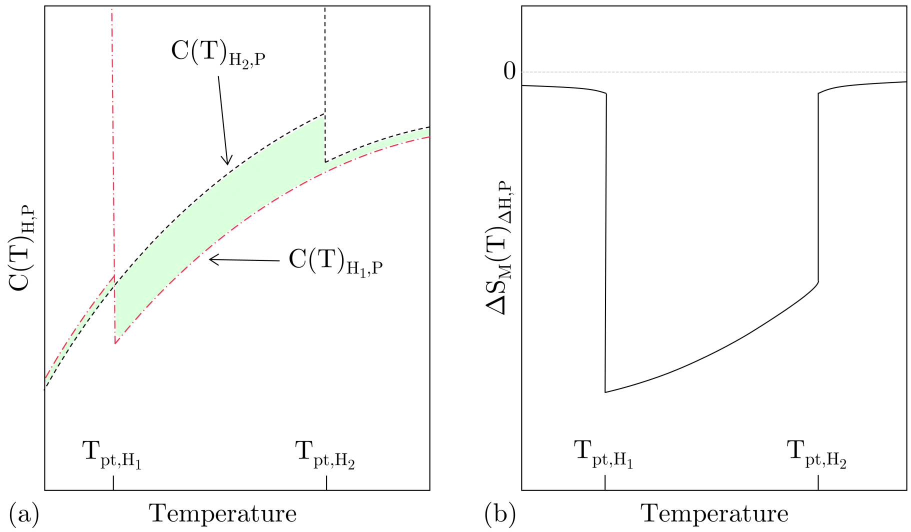

Figure 2.1: Plot of heat capacity and entropy change for positive MCE, idealized with $H_2 > H_1 = 0$. (a) shows the heat capacity curves, which each have a discontinuity at the transformation point. (b) shows the entropy change curve, which is proportional to the area between the two heat capacity curves, colored in green in (a). Plots modified from [37].

3. $T_{pt,H_1} - T_{pt,H_2}$: *With field*, the material has not yet transformed and follows the initial trajectory. *Without field*, the material has transformed and is at a lower C_p, so the area between the low and high field curves is moderately positive.
4. T_{pt,H_2}: Heat capacity with field reaches its transition point. The material transforms instantaneously and produces an infinitely high peak in C_p. Similar to segment 2, there is in reality a finite peak with a finite but large (positive) integral between low and high field curves.
5. $T_{pt,H_2} - \infty$: Both curves return to approximately the same level and no significant changes to the total integral occur.

Largest among these contributions to the heat capacity curve is the very large negative integral in segment 2. With an overall $\Delta S_{magnetic} < 0$, $S_{thermal}$ increases to compensate, and the material temperature rises upon adiabatic magnetization.

2.2.2.2 Negative MCE Materials that exhibit a negative MCE cool down upon adiabatic magnetization and heat up upon adiabatic demagnetization. The description of the MCE involving the integrals of the heat capacity curves is nearly identical to that in 2.2.2.1, except that the *with field* and *without field* curves are reversed. With this reversal, all of the segments that had a negative integral value are now positive and vice versa. Therefore, largest among the integral contributions is the very large positive integral in segment 2. With an overall $\Delta S_{magnetic} > 0$, $S_{thermal}$ decreases to compensate, and the material temperature decreases upon adiabatic magnetization.

2.2.2.3 Using the MCE in a Heat Pump Applications of the MCE in magnetic refrigeration and cooling can be understood at a basic level through a simple cycle involving a second-order MCE material, shown in Figure 2.2. In the first stage, the material begins at some nominal temperature. A magnetic field is then applied under adiabatic conditions, reducing ΔS_m (magnetic entropy) by aligning magnetic dipoles in the material. A reduction in ΔS_m in a constant-entropy system (adiabatic) causes the other entropy contributions to increase to compensate, namely ΔS_t (thermal entropy). This increase in ΔS_t manifests as an increase in sample temperature ΔT_{ad}. While the external magnetic field continues to

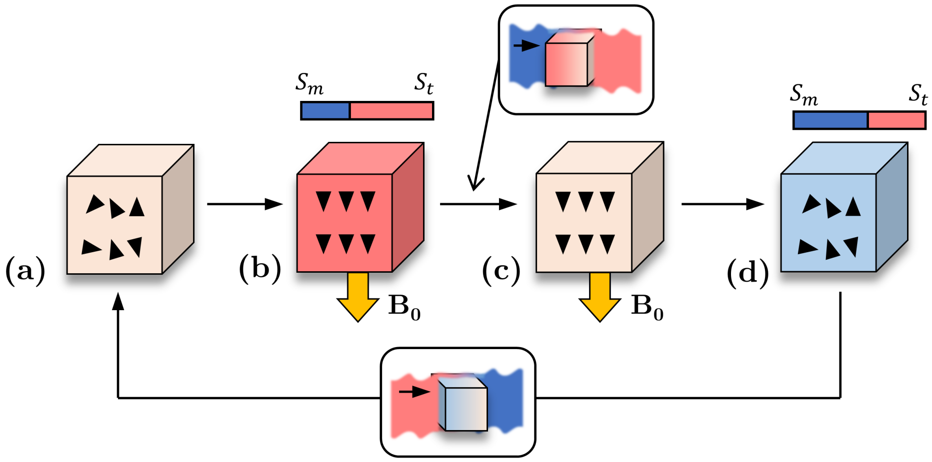

Figure 2.2: Simple representation of a cooling cycle utilizing the MCE: (a) The magnetocaloric heat exchanger begins at a nominal temperature with disordered magnetic dipoles. (b) An applied magnetic field aligns the magnetic dipoles, reducing magnetic entropy and causing thermal entropy to increase to compensate. (c) After a heat transfer fluid removes heat from the exchanger, its temperature is reduced and dipoles are still aligned. (d) Removing the magnetic field allows the magnetic dipoles to return to their misaligned state, increasing magnetic entropy and causing thermal entropy to decrease to compensate. To begin the cycle again, the heat transfer fluid brings in heat from the load (e.g. a refrigerator or air conditioner) which heats up the exchanger back to nominal temperature.

maintain magnetic alignment in the material, the excess heat generated by increasing ΔS_t is removed by some external means (a heat transfer fluid), leaving the material still magnetized but at a temperature near nominal. Finally, the magnetic field is removed adiabatically, and magnetic dipoles spontaneously return to their disordered state, increasing ΔS_m and thus decreasing ΔS_t and material temperature.

Leveraging the MCE for heat pump applications requires three basic components: a magnetocaloric material (the refrigerant), heat exchangers, heat transfer fluid (working fluid), and a magnetizing/demagnetizing component. There are two heat exchangers: hot and cold. The working fluid transfers heat between these two exchangers. The magnetizing/demagnetizing component is used to activate the MCE and manipulate the temperature of the refrigerant. With a combination of three thermodynamic process types, different established thermodynamic cycles could be realized in magnetic cooling [38]. The three component thermodynamic processes are as follows:

1. **Isothermal (de)magnetization**: the refrigerant is (de)magnetized at a constant temperature, giving rise to a ΔS_m.
2. **Adiabatic (de)magnetization**: the refrigerant is (de)magnetized in adiabatic conditions, giving rise to a ΔT_{ad}.
3. **Isofield temperature change**: a change in temperature initiated in constant magnetic field conditions.

With these three processes, thermodynamic cycles can be constructed for magnetic cooling, e.g. Carnot cycle, Brayton cycle, Ericsson cycle. Most focus is placed however on cycles with an active magnetic regenerator (AMR). In an AMR cycle, the magnetocaloric material is not only the refrigerant, but also the heat exchanger [38]. Also, testing new thermodynamic cycles in magnetic refrigerator systems is a unique opportunity that is not available for vapor-compression refrigeration. Presented in Figure 2.3, Kitanovski illustrated eight different combination AMR cycles that exhibit how much the cycle can be modified [39].

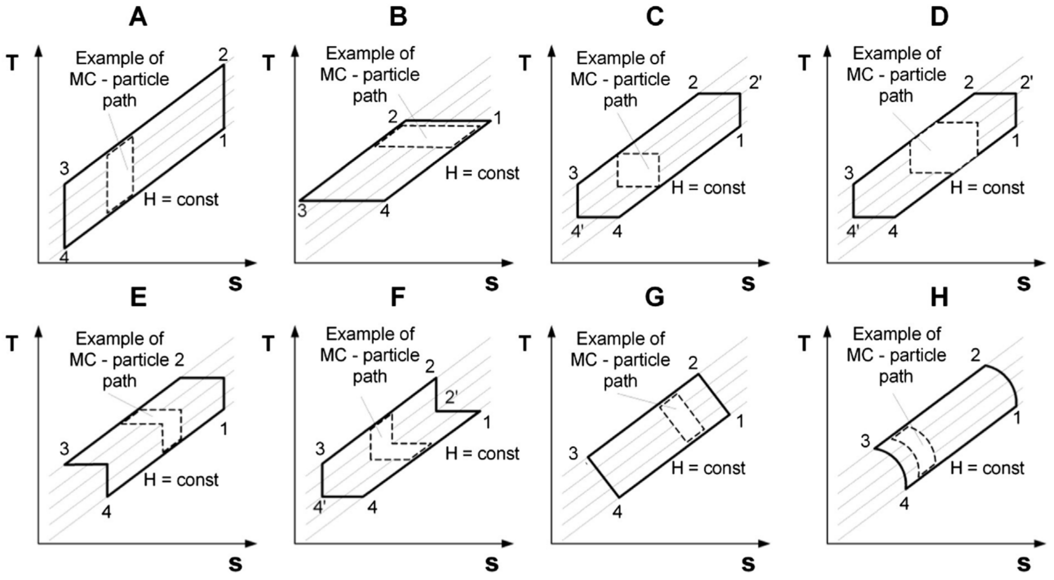

Figure 2.3: Thermodynamic cycle examples, each with an AMR: (A) Brayton, (B) Ericsson, (C) Carnot, (D), Hybrid Brayton-Ericcson, (E-H) potential new cycles. Reprinted from [39], Copyright 2013, with permission from Elsevier.

2.3 Measuring the Magnetocaloric Effect

Directly comparing material properties reported in literature for magnetocaloric materials can lead to inaccurate conclusions. Several studies have demonstrated that sample history, measurement technique, and even the number of measurement cycles can significantly change the material property evaluation value [40–42]. A quality comparison of material property measurements for this class of materials must take measurement methods and sample history into account. There are two types of measurement techniques to quantify the magnitude of the MCE, termed *direct* and *indirect* [43]. Direct measurements generally evaluate the ΔT_{ad}, while indirect measurements calculate the ΔS_m value from measured magnetic behavior over a temperature range.

2.3.1 Direct MCE Measurements

Direct thermal MCE measurements are obtained by directly measuring the temperature change of the sample in a changing magnetic field. No commercial systems are available for these measurements. The existing direct measurement literature is based on use of custom-built research instruments designed to measure ΔT_{ad} in magnetocaloric materials [44]. These systems are quite complex and pose major fabrication challenges, in large part arising from difficulty in maintaining proper thermal conditions for the sample. As a result, direct MCE measurements are only rarely reported in the existing literature. One simple setup, developed by Alvarez et al. [45], used a temperature sensor attached to a sample enclosed in a vacuum chamber and is shown in Figure 2.4.

Another method of direct MCE assessment does not require temperature measurements. Entropy change of the sample can be directly measured by enclosing the sample in a modified calorimeter and exposing the system to a changing magnetic field. This is even less common than direct thermal MCE measurements, but is a powerful tool for probing first order phase transition materials [46–48].

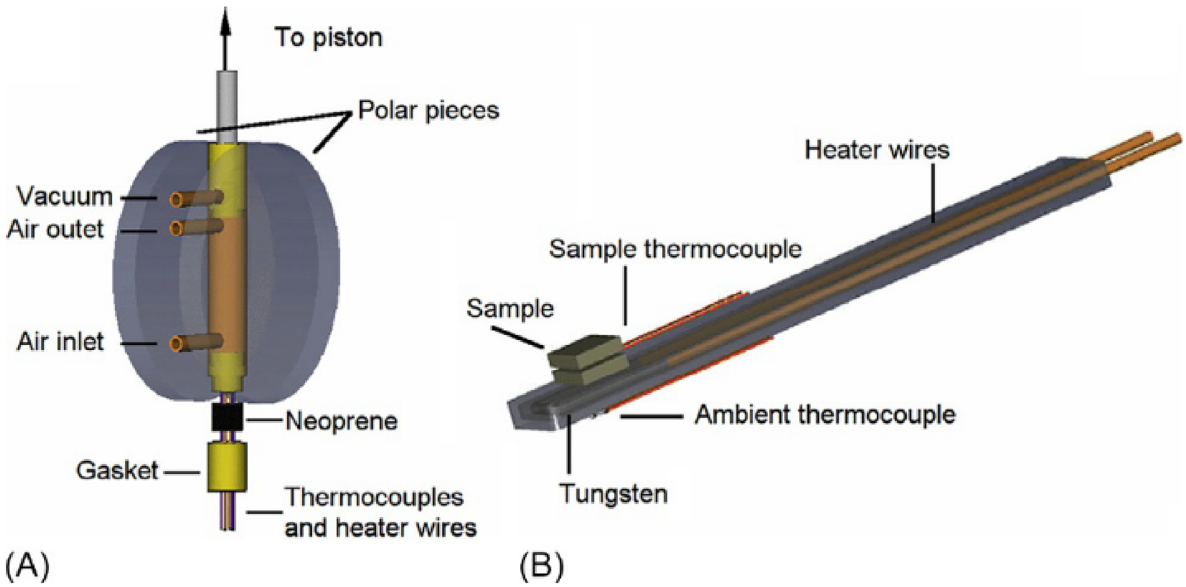

Figure 2.4: Schematic of an experimental setup used for measuring ΔT_{ad}. (A) shows the setup, and (B) shows the sample holder which is attached to the piston shown in (A). Reprinted from [45] with kind permission of TransTech Publications.

2.3.2 Indirect MCE Measurements

Indirect MCE measurements use magnetic data to calculate the entropy change within a material. Most frequently, the Maxwell relation (Equation 2.3) is integrated over the change in magnetic field for isothermal magnetization vs. field $M(H)$ curves or isofield magnetization vs. temperature $M(T)$ curves. For experimental evaluation with discrete measurement data, this relation can be integrated numerically, e.g. with trapezoidal integration.

$$\Delta S_m = \int_{H_1}^{H_2} \frac{\delta M}{\delta T} dH \tag{2.3}$$

Indirect measurements are controversial in the research field due to phase coexistence and $\delta M/\delta T$ discontinuity at the first order phase transition. Improper use of the Maxwell relation has led to claims of a colossal MCE, which were later found to be erroneous [49, 50]. Some authors argue that the Maxwell relation cannot produce correct results because it is not an accurate physical representation due to the heat capacity discontinuity and it does not account for the phase composition within the system. The Clausius-Clapeyron equation (Equation 2.4) has sometimes been used to account for the heat capacity discontinuity present in first order materials at the phase transition as well as the volume fraction of phases present [50, 51].

$$\Delta S = -\Delta M \cdot \frac{dH}{dT} \tag{2.4}$$

However, Mañosa et al. and Casanova et al. found good agreement between properly-executed Maxwell relation results and Clausius-Clapeyron results. They argue that the use of the Maxwell relation in carefully controlled circumstances is justified [52, 53]. There are several measurement protocols that may be used to ensure accurate Maxwell relation calculations, and in each the material must be *saturated* - returned to a fully uniform phase distribution - by either heating or cooling well past the transition point - before each isothermal or isofield measurement [54, 55].

2.3.3 Factors Affecting Changes in MCE Effectiveness

Experimental variation is a major challenge for research into magnetocaloric materials. Measured results are extremely sensitive to experimental conditions, which are difficult to control. Some common causes for variation are:

1. the use of various calculation methods for MCE magnitude (discussed in Section 2.3)
2. fabrication or measurement procedures performed slightly differently by independent operators
3. variation in powder distribution for a packed powder bed device
4. composition discrepancy, even slight, between two melts of an alloy

These factors affect results for MCE parameters, which can make even simple replication of a published study difficult. Variations due to seemingly small physical changes can all be attributed to differences in coupling mechanisms at several length scales, shown graphically in Figure 2.5 [56]. Broadly, coupling mechanisms can fall into the categories: atomic coupling, stress coupling, and magnetostatic coupling. Within atomic coupling, magnon-phonon, thermo-chemical, and chemo-magnetic coupling have an effect on transition temperature and magnetization. Stress coupling within the volume, at surface defects, and in thin films has an effect on all aspects of the MCE: transition temperature, magnetization, incomplete transformation, nucleation sites for the transition, and width of the transition. Magnetostatic coupling takes place between particles and across cracks and gaps, and affects transition temperature, nucleation sites, and width of the transition. Overall, all types of coupling have an effect on transition temperature, which is likely why variations of transition temperature are reported even in similar literature.

Magnetic refrigeration performance indices are a better indication of true in-service performance and measure more than MCE parameters like ΔT_{ad} or ΔS_m. Even these performance indices have multiple versions however, and researchers must be attentive during comparisons. To test magnetocaloric materials in situations closer to applicability, the refrigerant capacity (RC) parameter was developed, where a high RC parameter indicates better performance. RC has been defined in several ways, first by Wood and Potter (Equation 2.5)

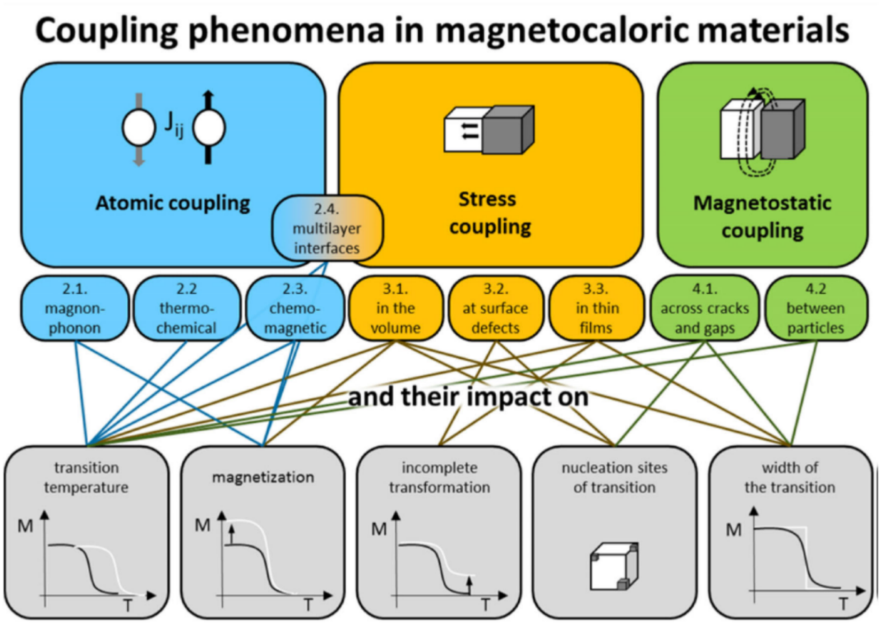

Figure 2.5: Coupling mechanisms in magnetocaloric materials and their effects. Reproduced with permission from [56], Copyright 2018 The Authors. Published by Wiley-VCH Verlag GmbH & Co. KGaA.

as a rectangle spanning the working temperature ($\Delta T = T_{hot} - T_{cold}$) range and bounded by ΔS_C, the magnetic entropy change at T_{cold} [57]. Gschneidner proposed defining RC as the area under the $|\Delta S_m(T, H)|$ curve (Equation 2.6), with the temperature span being defined as full-width at half-maximum (FWHM). Finally, relative cooling power (RCP) is defined by Gschneidner as a rectangle enclosing the entire $|\Delta S_m(T, H)|$ curve at FWHM (Equation 2.7) [58]. The relative results of these equations are compared schematically in Figure 2.6 [42].

$$RC_{W\&P} = |\Delta S_m| \cdot \Delta T \tag{2.5}$$

$$RC_{Gschneidner} = \int_{T_{cold}}^{T_{hot}} |\Delta S_m| dT \tag{2.6}$$

$$RCP = |\Delta S_m|^{max} \cdot \delta T_{FWHM} \tag{2.7}$$

2.4 Heusler Alloys as Magnetocaloric Materials

The discovery of magnetocaloric response of Gd initiated the contemporary search for materials that exhibit magnetocaloric effects at room temperature. Many specific alloys have since emerged that are functional due to varying material responses. Lyubina suggests categorizing these into second order phase transition (SOPT), strong first order phase transition (FOPT), and weak FOPT materials [6]. SOPT materials experience only a gradual magnetic phase transition. Strong FOPT materials generally have strong magnetostructural coupling, and are distinguished by their high transition barrier energy. In contrast, weak FOPT materials have a magneto-elastic phase transition with a sudden change in lattice parameter though the unit cell type remains the same [59]. Weak FOPT materials have a lower energy barrier, and a gradual shift from FOPT to SOPT. Since hysteresis size is inherently related to transformation barrier energy, strong FOPT materials show a larger hysteresis than weak FOPT or SOPT materials.

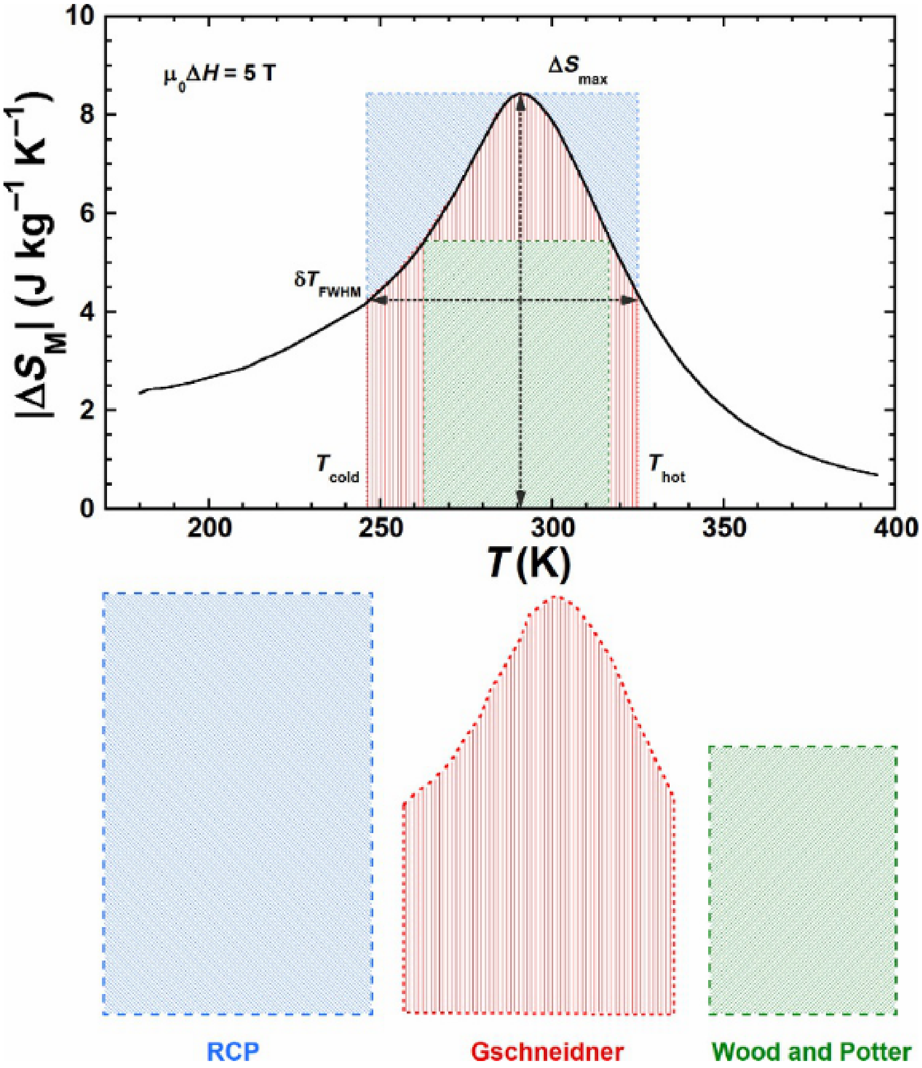

Figure 2.6: Schematic of RC calculation methods, showing their differences in defined area. Reprinted from [42], Copyright 2018, with permission from Elsevier.

Magnetocaloric materials could also be categorized as crystalline or amorphous, as well as rare-earth-containing and rare-earth-free [60]. Categorization efforts should also make a clear distinction between materials that exhibit positive MCE, negative MCE, or both depending on the operating temperature. While many compositions are under active investigation as of 2020, Waske et al. considered three first-order-type materials to be most relevant due to their combination of properties, cost, and availability: Mn-Fe-P-Si, La-Fe-Si-H, and Ni-Mn-In-Co [32].

The promising material Ni-Mn-In-Co is part of a class of alloys discovered by Friedrich (Fritz) Heusler. In 1901, Heusler wrote a note to the Deutsche Physikalische Gesellschaft (German Physical Society) regarding his discovery of compounds containing Mn that were magnetic, despite containing only non-magnetic elements [61]. Two years later, in 1903, the one-page note was published along with two longer related articles [62, 63].

Heusler alloys have the chemical formula X_2YZ, where X and Y are usually transition metals or rare earth metals, and Z is a non-metal or a non-magnetic metal. These are ferromagnetic materials that exhibit four interpenetrating face-centered cubic (fcc) lattices. If ordered, this results in the $L2_1$ cubic Heusler phase ($Fm\bar{3}m$, no. 225). One common form of disorder is a Y/Z B2-type disorder, resulting in a simple cubic lattice ($Pm\bar{3}m$, no. 221) [64].

Heusler's discovery of these magnetic alloys was sufficiently interesting to prompt the investigation of an eponymous category of similar alloys. In 1903, Heusler discovered that Cu_2MnAl was ferromagnetic, though none of its elements were [62]. Modern investigations of Heusler alloys commonly focus on Ni_2MnGa and its off-stoichiometric variations, investigated for magnetic shape memory or magnetocaloric applications. The magnetism in Ni-Mn-based Heusler alloys is carried primarily in the Mn atoms, which have the highest magnetic moment of all the transition metals [60]. In stoichiometric Ni_2MnGa, the Mn sublattice accounts for over 85% of the saturation magnetization (3.5 μ_B of the total 4.1 μ_B). The large magnetic contribution of Mn is contingent however on Mn occupying its own sublattice. An excess of Mn begins to occupy the non-Mn sublattices and couples antiferromagnetically with the Mn sublattice atoms, decreasing the overall saturation magnetization [65].

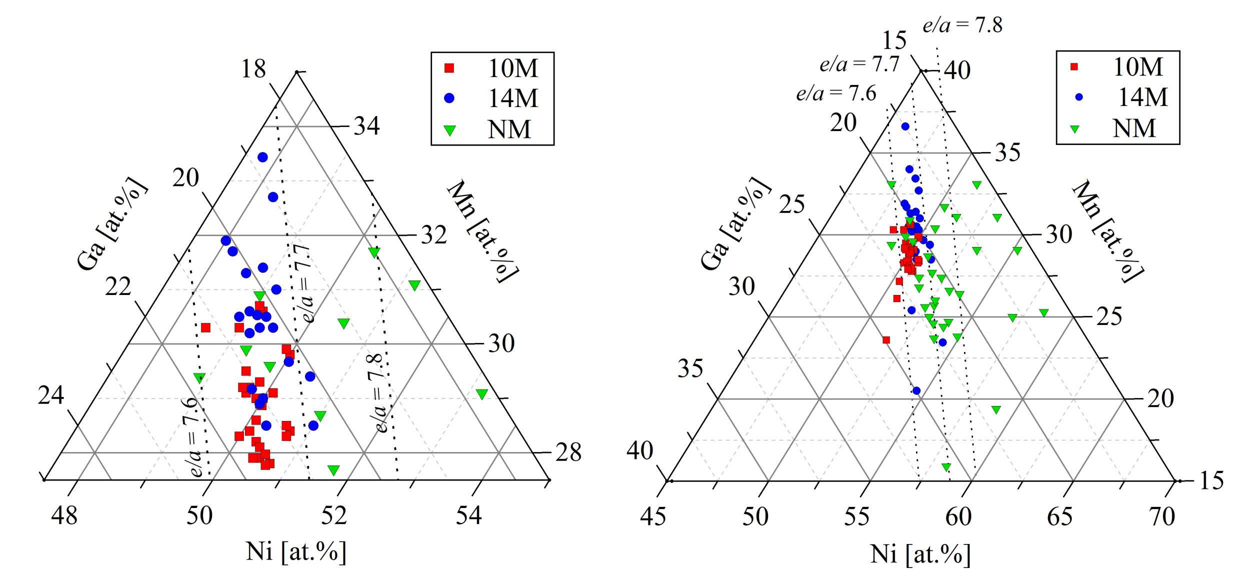

Figure 2.7: Ni-Mn-Ga phase diagram (right) and magnified critical portion (left), showing valence electrons per atom e/a and phase formed (10M, 14M, and NM). Data from [67–73].

For these Heusler magnetic functional materials (that exhibit a change in physical properties in response to application of an external magnetic field), it is commonly accepted that a deciding factor for what phases form is the ratio of valence electrons to atoms (e/a) [64]. Monitoring the e/a ratio is critical because seemingly slight changes to alloy composition can change e/a and the phases that will form. A small difference in composition can mean the difference between a functional and non-functional Heusler alloy. Figure 2.7 (a ternary phase diagram for Ni-Mn-Ga at room temperature) demonstrates how small deviations in the e/a ratio can alter the phases that form and where transformations occur [66].

Within Heusler alloys like Ni-Mn-Ga, a structural transformation occurs, considered to be a martensitic transformation. At high temperatures, a cubic austenite phase is present. Cooling through the martensitic transformation temperature induces a phase change to a tetragonal, pseudo-tetragonal monoclinic, or pseudo-orthorhombic monoclinic martensite phase. As with all martensitic transformations, this phase change is a diffusionless, displacive solid-state transformation that distorts the lattice and is driven by strain energy [74]. For such transformations, which are constrained due to bulk or external forces, a shearing must occur in order to leave the lattice invariant; this shear can be achieved through either slip or twinning. In Ni-Mn-based alloys, twinning is observed, forming a self-accommodated martensitic structure [75].

Ni_2MnGa and its off-stoichiometric alloys have several possible unit cell structure types, and each structure can be classified differently depending on the desired amount of symmetry or simplicity. Other Ni-Mn-based Heusler alloys such as Ni-Mn-Co-Sn share many of these same unit cells, though the largest body of literature exists specifically for Ni_2MnGa. The most relevant unit cell structure types for magnetic functional purposes are: non-modulated, modulated 10M (also referred to as 5M), and modulated 14M (also called 7M). This naming convention uses M to designate a martensite phase. In both the modulated 10M and 14M structures, the number refers to the amount of atomic planes before an exact duplicate repeated plane. In the case of 5M and 7M designations, the plane of atoms 5 or 7 planes away has atom sites at the same locations on the lattice but some elements are switched within those sites from the initial plane [76].

Off-stoichiometric Ni_2MnGa has magnetocaloric properties, but with no doping elements, the alloy tends to have a large thermal hysteresis and losses, as well as a high field required to initiate the structural transformation [35,60,77]. As a result, a primary research goal in the field is developing materials with narrowed thermal hysteresis and the ability to transform under modest magnetic fields [35,77]. One important recent advance is the discovery of partial transformation loops (originally termed *minor loops*) that can increase reversibility and lower transformation field for Heusler alloys [78,79].

2.4.1 Ni-Mn-Co-Sn

Ni-Mn-Co-Sn metamagnetic shape memory alloys (MMSMAs) exhibit inverse, or negative, MCE behavior. MMSMAs exhibit a decrease in martensite transformation temperature in response to an increased applied magnetic field.

Research into Ni-Mn-Sn alloys began in 2005 with a report by Krenke et al. on the discovery of inverse MCE in $Ni_{50}Mn_{37}Sn_{13}$ [80]. Ni-Mn-Sn shows an inverse transformation because (in contrast with Ni-Mn-Ga Heusler alloys) Mn atoms in Ni-Mn-Sn show antiferromagnetic coupling in the martensite phase. At specific compositions, a metamagnetostructural transformation from antiferromagnetic martensite to ferromagnetic austenite is observed [60]. In ternary Ni-Mn-Sn, an increase in e/a increases transition temperature, but alloying elements break this trend [81, 82]. Substituting Co for Ni reduces the transformation temperature, affects the T_C of the austenitic phase, increases the magnetic moment, and slightly reduces thermal hysteresis [83–85]. Bruno et al. conducted a systematic study on heat treatment of Ni-Mn-Co-Sn alloys, showing that a faster cooling rate increases atomic disorder, which in turn improves lattice coherence and decreases thermal hysteresis [86].

2.4.2 Ni-Mn-Cu-Ga

Unlike Ni-Mn-Co-Sn, most Ni-Mn-Ga-based ferromagnetic shape memory alloys (FSMA) show a positive MCE. FSMAs exhibit a increase in martensite transformation temperature in response to an increased applied magnetic field. Changing the composition of Ni-Mn-Ga shifts the martensitic transformation and Curie temperatures, and coincidence of these phase changes is beneficial for the MCE. Shown in Figure 2.8, in Ni-rich $Ni_{2+x}Mn_{1-x}Ga$, T_M and T_C are expected to coincide for $0.18 < x < 0.27$ ($7.635 < e/a < 7.7025$). In Figure 2.8, it is clear that for ternary alloys, the transformation temperature increases with e/a (line 1), while for added transition elements, the transformation temperature decreases with e/a (lines 2 and 3). Adding non-transition elements such as Sn have no significant effect on e/a but do affect transition temperature (line 4, Figure 2.8).

Stadler et al. reported magnetocaloric properties with Cu substitution for Mn in a polycrystalline alloy of $Ni_2Mn_{1-x}CuGa$, showing a $-\Delta S_m$ of around 29 J/(kg · K) at 2 T [88]. There have been several attempts to increase MCE by altering the composition, changing Mn slightly [89] or adding Fe/Ge [90], but neither had much effect. In 2010, Kataoka published a phase diagram of $Ni_2Mn_{1-x}Cu_xGa$, shown in Figure 2.9, elucidating the region where $T_C = T_M$. Recently, in 2016, Sarkar et al. conducted a systematic study of Cu variation in $Ni_{50}Mn_{25-x}Cu_xGa_{25}$ wt.% (x = 1, 1.25, 2.5, 3.75, 6.0, 6.2, 6.25, 6.5, 7.0) [91]. Their results showed that T_C decreased with Cu substitution while T_M increased, explained by the

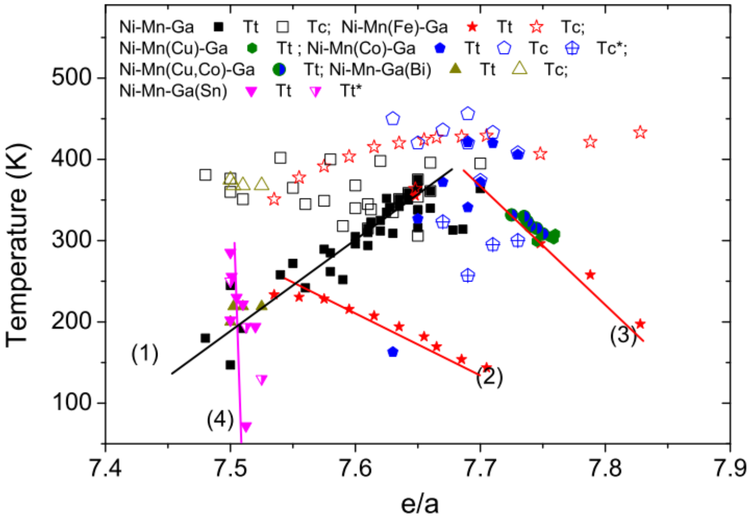

Figure 2.8: Variation in Ni-Mn-Ga(-X) transition (T_t) and Curie (T_C) temperatures due to element content and e/a. Reprinted from [60] Copyright 2018, with permission from Elsevier.

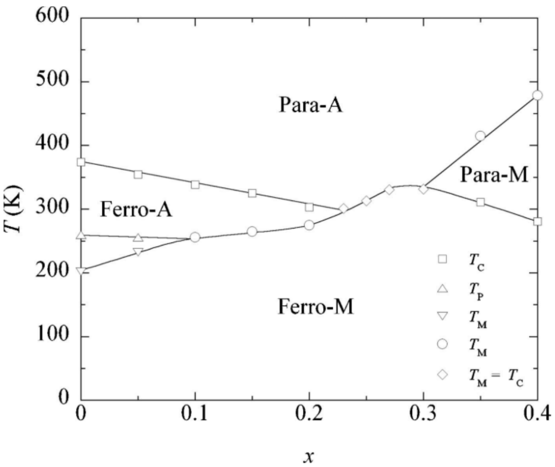

Figure 2.9: $Ni_2Mn_{1-x}Cu_xGa$ phase diagram showing austenite (A), martensite (M), pre-martensitic transition (T_P), Curie temperature (T_C), and martensitic transition (T_M). Reprinted from [87] with permission, Copyright 2010 by the American Physical Society.

strengthening of Ni-Ga bonds and a decrease in Mn or Mn-Mn ferromagnetic exchange interaction. Also, at $Ni_{50}Mn_{18.5}Cu_{6.5}Ga_{25}$, there was overlap for A_s (austenite start) and T_C, leading to a large magnetic entropy change $-\Delta S_m$ on heating of 60.2 J/(kg · K) at 5 T.

Li et al. varied Cu concentration in $Ni_{50-x}Cu_xMn_{31}Ga_{19}$ (x = 2-10) and found an increase in Cu led to a decrease in martensite start temperature (M_s) attributed to an enlargement of the unit cell, and a broadening of the transformation region (A_f - M_s, where A_f is the austenite finish temperature) [92]. Recently, Seguí et al. also studied a series of $Ni_{50}Mn_{25-x}Cu_xGa_{25}$ alloys with x = 3-11, finding a paramagnetic austenite → ferromagnetic martensite magnetostructural transition between x = 5.5 and 7.5, and results corroborating that increasing Cu substitution for Mn increases the martensitic transformation temperature and decreases T_C. $Ni_{50}Mn_{19}Cu_6Ga_{25}$ was found by Seguí to have the lowest thermal hysteresis of the studied series, a result attributed to a minimum of the austenite-martensite lattice mismatch [93].

2.5 Additive Manufacturing and Post-Processing

Additive manufacturing (AM) is the process by which material is strategically added to create a near-net-shape part [94]. This manufacturing type stands in contrast to conventional manufacturing methods such as casting (where material is solidified in a shaped mold to create a near-net-shape part) and machining (where material is removed from a bulk shape to achieve a specific geometry). AM began as a method for rapid prototyping using polymers, but between 2010 and 2020, the technique's use grew to include the use of ceramics, metals, biomaterials, foods (e.g. chocolate), and composites (e.g. concrete). AM is advantageous for some applications in that it is able to generate very little waste, can be used to create complicated part geometries, and includes relatively few processing steps [95–97]. Despite these benefits, AM techniques are not a universal manufacturing solution due to costs, resulting material properties, and process capabilities. Determining the effects of these processes on the structure and consequent properties of materials is an active area of investigation.

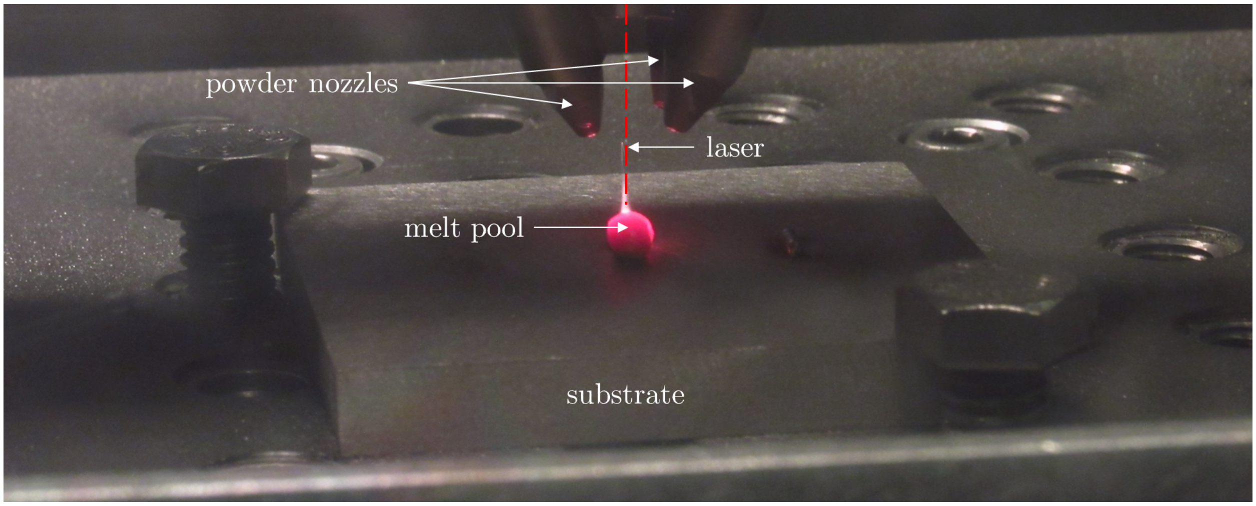

Figure 2.10: DLD LENS® with components labelled.

2.5.1 Direct Laser Deposition

Laser Engineered Net Shaping (LENS®, Sandia National Laboratories, Albequerque, NM, USA) is a laser-based method of additive manufacturing that can also be categorized as direct laser deposition (DLD). A laser is used to create a melt pool on a substrate, while powder is directed towards the melt pool via powder nozzles. This powder adds to the melt pool volume and builds up the part selectively as the laser is scanned over the substrate surface in a pre-determined path that is programmed based on solid model information. The substrate then moves away from the laser source an incremental amount and the next layer of the part is deposited in the same way. This process continues until the near-net-shape part is completed. DLD LENS® is shown with labeled components in Figure 2.10.

Though DLD cannot be used to manufacture all types of complex geometries due to its difficulty creating unsupported overhangs and very smooth surfaces, there are applications for which this manufacturing approach is a good match. Currently, DLD is used to repair the edges of turbine blades that have eroded in service, and it can also be used to create relatively simple part shapes without steep overhangs. Other benefits of DLD include the ability to use less powder than powder bed techniques, and capability for generating structures with variable composition by modifying the feedstock powder ratios during the fabrication process [98]. Though DLD is an attractive method for complicated geometries and repair, the structure and properties of resulting parts must be carefully evaluated, since DLD production creates intense thermal profiles with several cycles of quick heating and cooling [99, 100]. These thermal cycles strongly influence the microstructure and can lead to instances such as dendrite formation, varying grain size and shape, and microsegregation [101].

2.5.2 Powder Bed Binder Jet Printing

Powder bed binder jetting 3D printing (BJ3DP) is a powder bed-based method of AM, commonly called 3D printing because of its similarity to conventional ink-jet printing. With BJ3DP, there is no energy source to bind the powder together as in electron beam or laser systems; rather, a binder is used to adhere particles together selectively within the job box [102]. The BJ3DP process is as follows, with slight variations for different machines:

1. A layer of powder is laid down using powder from a hopper or feeder.
2. A roller or blade is dragged across the powder to flatten the layer.
3. Jets selectively deposit binder in a path pre-determined by a computer model.
4. A small amount of heat is applied to slightly dry the binder.
5. The job box is moved down by a distance equal to the prescribed layer height.
6. Steps 1-5 repeat until the part is finished.
7. The entire job box is removed from the machine and placed into a curing furnace, where the binder is cured at a low heat (180-200 °C, usually for 2-8 h).
8. Parts are carefully removed from the job box, and excess powder is removed in a process called de-powdering. These so-called “green” parts are fragile.
9. Based on the material and part geometry, a post-processing method is carried out to increase density and stability.

BJ3DP has several capabilities that distinguish it from energy-based AM methods like DLD: compatibility with a wider variety of materials, operation in atmosphere at room temperature, no support structures required, no significant melting and cooling cycles, and high throughput [102]. For magnetic functional materials in particular, BJ3DP is advantageous

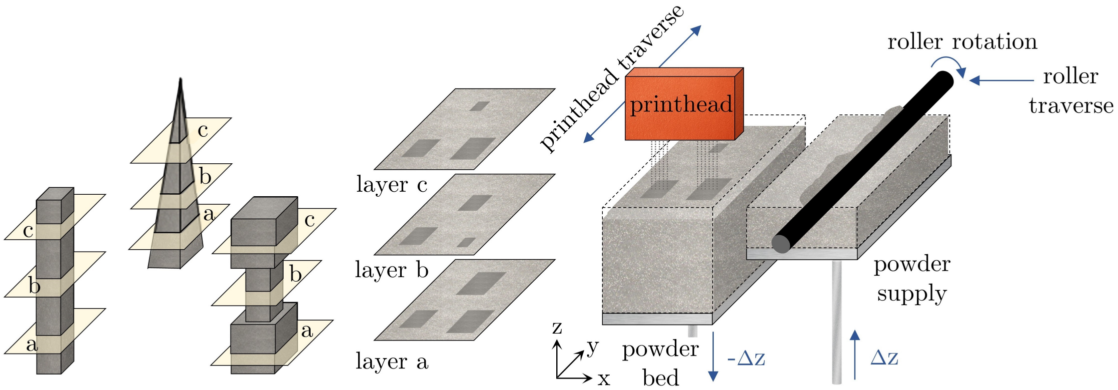

Figure 2.11: X-1 Lab binder jet 3D printing process, left to right: the desired samples from a model are sliced for layer-by-layer printing. In the printer, the printhead selectively deposits binder. The powder supply piston is raised and the powder bed is lowered by Δz. A roller pushes powder from the supply box to the powder bed, flattening the resulting layer.

because the lack of melting enables the structure and properties of the starting powder to be maintained. The melting that would be experienced in a DLD process, for example, alters composition by small amounts, changing the e/a value enough to affect the transformation temperatures. In some magnetocaloric materials, melting can also break down the crystal structure or reverse the efforts of hydrogenation.

An ExOne X-1 Lab 3D printer was used in this investigation, a schematic for which is presented in Figure 2.11. This machine is relatively atypical for BJ3DP systems in the orthogonality of its printhead and roller, as well as its dual powder beds (one as a feed bed and the other as a build bed), and is preferred by many research groups for its very small build volume. A small build volume requires less powder to fill, important for research-scale batches of expensive or hard-to-prepare materials.

As-printed (green) parts from a binder jet printer are not structurally sound and require strengthening, primarily through densification. One method for densification is pressureless solid-state sintering, where the part undergoes a heating protocol in a furnace that facilitates mass transport from the solid material to the empty space. This sintering process increases particle bond interfaces and also usually shrinks the overall volume, increasing the density of the part. Surface energy reduction is the driving force for sintering. Necks (particle contacts) grow in an effort to reduce curvature and surface area at interfaces between particles. This is initially achieved through surface diffusion of atoms to the contact, and (for crystalline materials) is then achieved through grain boundary diffusion as the neck grows larger [103].

There are three stages to solid-state sintering, often delineated by the coordination number of particles [104, 105]:

1. **Initial**:
    - Necks form and grow, at an initially fast rate that decays quickly over time.
    - Curvature gradients dominate driving force.
    - Neck size ratio (*neck diameter/particle diameter*) is less than 0.3, shrinkage is less than 3%, and grain size is similar to that of the stock powder.
2. **Intermediate**:
    - Contact area between particles continues to increase, some grain growth occurs near the end of the stage.
    - Pores become interconnected and less angular, resulting in less driving force from surface area and curvature.
    - Density is approximately 70-92% (theoretical), and pores can become larger.
3. **Final:**
    - When porosity is around 8% or less, open porosity is unstable and pinches off into individual pores (lenticular or spherical).
    - No longer inhibited by an open pore network, grain growth progresses more quickly.

While porosity decreases with longer sintering times in a very generalized sense, the extent of this behavior is limited. Figure 2.12 demonstrates the relationship between grain size vs. pore size, in which there is a critical region where pores become detached and can no longer escape, leading to residual porosity and a coarser microstructure [106].

Times required to reach these various stages of sintering and porosity are determined by the mass transport mechanisms of the sintered material. The two primary categories of

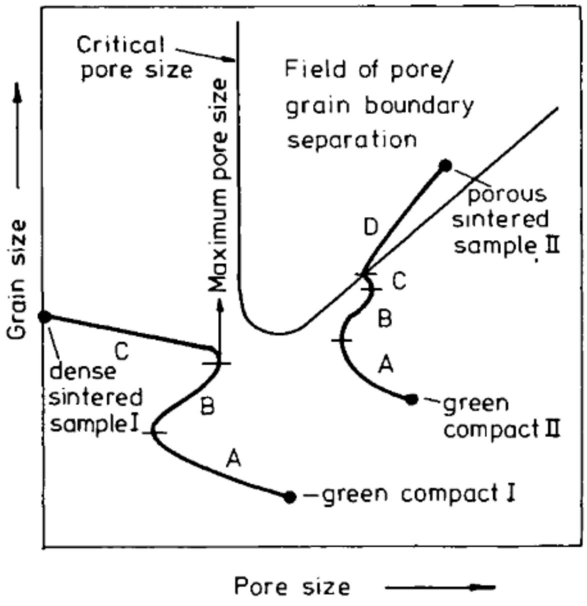

Figure 2.12: Plot of grain size vs. pore size, indicating the field of pore-grain boundary separation where residual porosity is expected. Green compact I to dense sintered sample I is an example of a sintering path for full density, while green compact II to porous sintered sample II will have residual porosity. Segment A: initial stage of sintering; Segment B: intermediate stage of sintering; Segment C: final densification; Segment D (only in Sample II): pore-grain boundary separation, grain growth. Reprinted from [106] by permission from Springer Nature: Springer Nature, Sintering Processes by H. Exner, E. Arzt, Copyright 1996.

mass transport (there are others or various distinctions in more advanced sintering theory) are [107–110]:

1. **Surface (grain boundary) diffusion**:
   - Material moves around the surface.
   - No densification occurs.
2. **Bulk (volume, lattice) diffusion**:
   - Material moves from inside the bulk.
   - Densification occurs.

In powder bed binder jet 3D printed parts, the prediction of kinetics becomes complicated, since a distribution of powder sizes is encountered, causing nonuniform densification rates as well as internal stresses [105]. While a casual observer might anticipate that small powders would produce less residual porosity after sintering, in fact a wider particle size distribution has better packing within the bed. A wider size distribution leads to denser parts after sintering because of a decreased probability for small particles to gather into large agglomerates or be ejected by high-velocity binder [111].

2.6 Current State of Manufacturing of MCE Materials

It is well known that for favorable heat transfer in magnetic refrigeration, a high surface to volume ratio is required of the magnetic refrigerant [5,20]. In order to obtain the maximum response and the best fluid flow, the following additional requirements are placed upon the refrigerant's structural design:

1. Maximize volume fraction of magnetocaloric material.
2. Minimize pressure drop in the fluid.

First order phase transition (FOPT) materials tend to be brittle, limiting machinability, so fabricating a heat exchanger with the desired properties can pose a challenge. Fabrication limitations have resulted in experiments where alloys that showed promise in laboratory testing only exhibited a modest MCE at best in a final, finished structure [112, 113].

There are two types of production that can be discussed: the fabrication of magnetocaloric alloys, and that of the heat exchanger devices that would be used in applications. As far as the alloys themselves, a common method is that of melt-spinning ribbons (rapid solidification), since this could be tailored to produce nanocrystalline, polycrystalline, or amorphous materials, and can encourage formation of certain desirable phases [114–119]. Decreased crystallite size also reduces heat treatment times from up to a week for certain bulk materials down to several hours for small crystallites [116]. However, not every case of melt-spun ribbons has been found to be preferable to bulk alloys, as Liu et al. noted of La-Pr-Fe-Si [120]. Other methods of alloy production are arc or induction melting and ball milling for mechanical alloying, phase formation, or hydriding [121]. Table 2.1 provides a categorization of literature based on alloy and fabrication methods.

Three common methods for producing heat exchanger devices are packed powder beds, parallel plates, and microchannel structures. Schematics of these methods as well as their properties are depicted in Figure 2.13 [32]. Design tradeoffs exist between pressure drop in the fluid, void fraction, and manufacturing cost of refrigerant devices [122]. A low fluid pressure drop is desired to minimize energy losses, the void fraction must allow for the maximum amount of magnetocaloric material to be available for the fluid to contact and initiate heat transfer, and manufacturing cost is of course desired to be as low as possible. Some additional methods for fabricating devices from some common magnetocaloric material systems are detailed in Table 2.1.

Beyond fabrication method, another important practical consideration for the production of magnetocaloric-based heat exchangers is the presence of a large operating temperature range. Because the MCE exists due to a phase change, an ideal operating temperature within the range of that phase change inherently exists. The ideal operating temperature for an MCE material is narrow compared to the range necessary for a functional appliance such as an air conditioner or refrigerator. A body of literature exists that focuses on widening the operating temperature range of individual MCE materials, but the most straightforward solution is to layer MCE materials with gradient properties, namely Curie temperature (T_{C}) [132, 164, 173]. A schematic representing cooling with a gradient layered material is given in Figure 2.14, showing a warm fluid entering a heat exchanger comprised of stacked

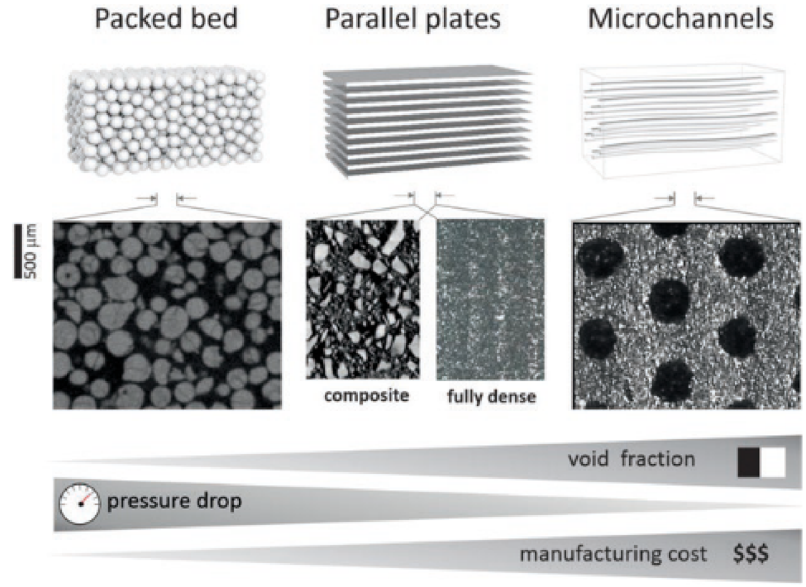

Figure 2.13: Magnetocaloric refrigerant device geometries. Reproduced from [32], Copyright Materials Research Society 2018, with permission from Cambridge University Press.

Table 2.1: Select manufacturing and production methods for magnetocaloric materials (or similar functional magnetic materials) and devices. To be considered devices in this review, parts had to be specially-designed geometries tested in or built for a magnetic cooling system.

Type	Method	Ni-Mn-based	La-Fe-Si-based	Mn-Fe-Si-based	Gd-based
Material	Arc/induction melting	[123, 124]	[125–127]	[128, 129]	[130–132]
	Melt spinning/strip casting	[116, 133]	[119, 120, 127, 134, 135]		
	Ball milling/crushing	[136–139]	[112, 127]	[140–143]	[130, 131]
	Gas atomization	[144–148]	[149, 150]		
Device	Powder metallurgy	[151]	[134, 152–156]		
	Packed/bonded particle bed		[157]	[158, 159]	[132, 160–166]
	Parallel plates		[167]		[163, 168–171]
	Machined microchannels			[172]	
	Additive manufacturing		[112]		

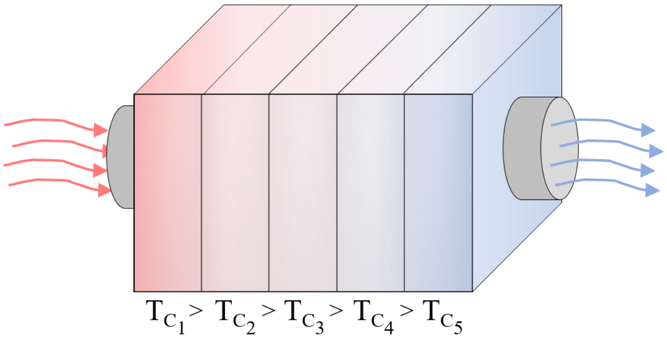

Figure 2.14: Schematic of a gradient layered MCE material. The heat transfer fluid enters at a high temperature and contacts the layer with the highest operating temperature and T_c. As the fluid progresses through the heat exchanger, it is progressively cooled and comes into contact with progressively lower operating temperatures.

magnetocaloric materials having progressively lower T_C. A lower T_C translates to a lower optimal operating temperature range. Thus, as the fluid flows through the heat exchanger it is progressively cooled, and the heat exchanger material has a correspondingly lower optimal operating temperature range, increasing efficiency.

2.6.1 Additive Manufacturing of Functional Magnetic Materials

There are currently large, well-established communities investigating both MCE materials and additive manufacturing, but there are few researchers at the intersection. As of August 2020, Web of Science returns 6,920 results for the term *magnetocaloric* (Scopus returns 7,781, and Dimensions returns 18,510 since it includes the International Journal of Refrigeration and more conference proceedings). Adding to *magnetocaloric* the search terms *additive manufacturing* or *selective laser melting* or *binder jet* or *3D print* decreases the count to an underestimation of 11 articles in Scopus, and an overestimation of 104 publications in Dimensions (Scopus does not include all conference publications or recent articles; whereas

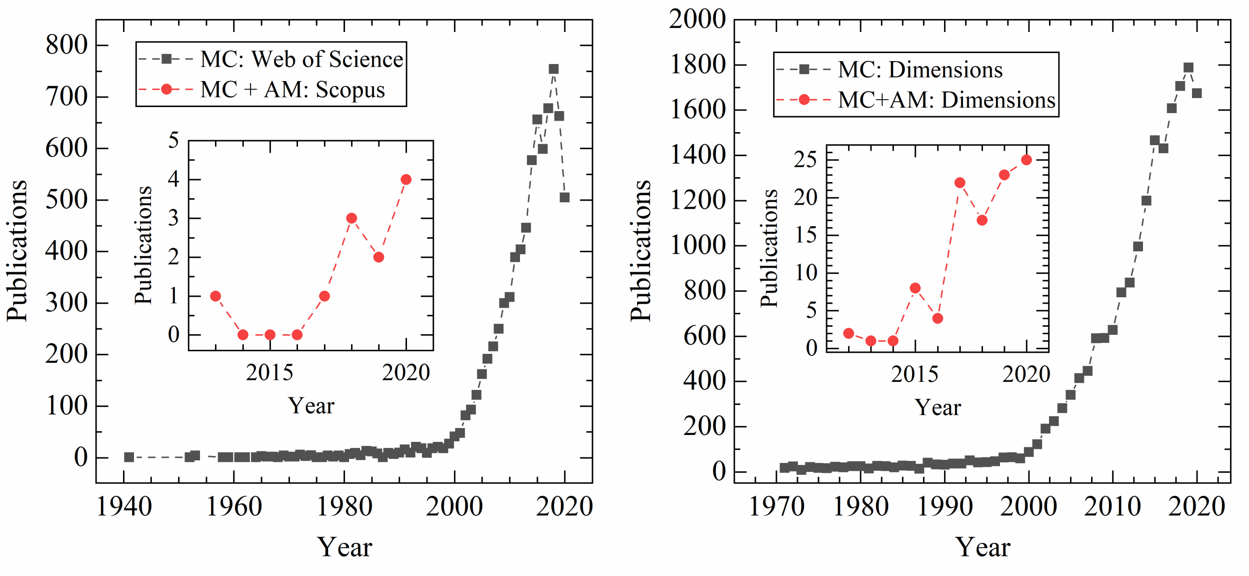

Figure 2.15: MC and MC+AM publications by year, from the databases Scopus, Web of Science, and Dimensions.

Dimensions seems to include publications that are not wholly related). Though exact publication numbers are difficult to determine, this analysis of research interconnections clearly demonstrates that additive manufacturing of magnetocaloric materials is a sparsely populated field that is just now gaining interest, after physics and chemistry communities have described the particle physics and solid state chemistry of the MCE. Now, the engineering and manufacturing fields must advance MCE research into practical implementation.

Studies regarding AM of functional magnetic materials (FMMs), including magnetic shape memory and magnetocaloric materials, are few and have mostly been published within the few years preceding 2020. Results of the MC and MC+AM database searches are plotted by year in Figure 2.15. Most research into AM of FMMs is being pursued with goals to expand geometrical freedom, manage the brittle nature of some FMMs, and optimize microstructures. MCE research prioritizes fabricating porous, complex structures that can minimize pressure loss and maximize heat transfer [112, 143, 150, 174–178].

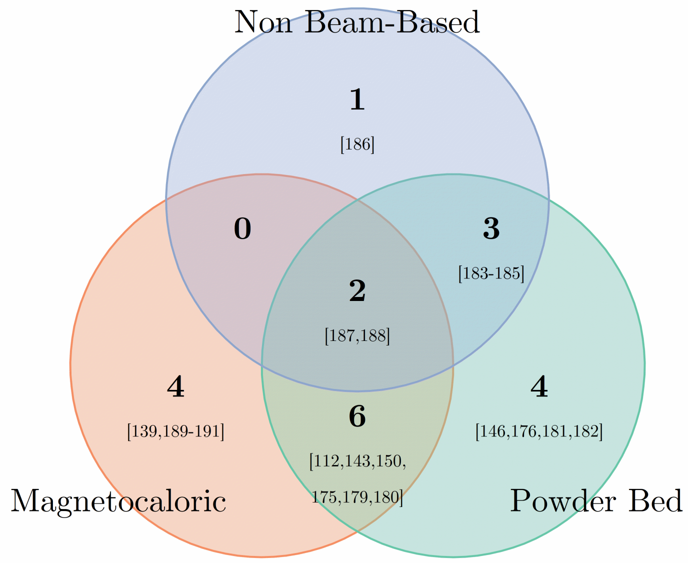

Figure 2.16: Venn diagram of FMM+AM investigations, indicating whether they use magnetocaloric materials, non beam-based methods, and/or powder bed methods [112, 139, 143, 146, 150, 175, 176, 179–192].

AM of FMMs research can be categorized either by beam-based (where “beam” refers to any energy source, typically a laser or electron beam) and non beam-based or by powder bed and powder feeder. A visual representation of where recent related references fall within these categories is shown in Figure 2.16 along with whether the study was conducted with the purpose of advancing magnetocaloric functionality.

3.0 Hypotheses

For this investigation, one beam-based non-powder-bed (direct laser deposition) and one non-beam-based powder bed (binder jet 3D printing) manufacturing method was selected for contrast. Resulting structures and thermal, magnetic, and functional properties of the Ni-Mn-based magnetocaloric materials were examined. Both manufacturing methods were monitored through post-processing. For direct laser deposition, post-processing was homogenization. For binder jet 3D printing, post-processing was a sintering heat treatment followed by annealing. Heat treatment steps were monitored closely *in-situ* for structure changes.

1. Both laser-based and binder jet additive manufacturing methods will be able to produce stable and functional MCE materials.
   1.1. Laser deposition will produce viable samples, after an optimized homogenization step.
   1.2. Binder jet 3D printing will produce viable samples, after an optimized sintering step.
2. A small-scale binder jet printer can be designed and fabricated to produce multi-material samples with little material waste.
   2.1. Sintering of mixed-powder samples will produce a nearly homogeneous composition.
   2.2. For two materials with different sintering properties, density can be tailored per set of layers in multi-material prints.
3. *In-situ* monitoring of sintering and annealing heat treatments of binder jet 3D printed samples can reveal structural evolution.
   3.1. Sintering treatment will change lattice parameter by relieving residual stresses and improving homogenization.
   3.2. Multi-material layered parts will exhibit multiple phase transformations.

H1.1: Laser deposition will produce viable magnetocaloric samples, after an optimized homogenization step

Direct laser deposition (DLD) is an additive manufacturing method that incorporates full melting of powders and large variations in temperature during printing. DLD has the benefit of not requiring a full build bed of powder, but the thermal cycles and full melting can significantly alter the structure and composition between the feedstock powder and final part. Though the as-printed parts are expected to show elemental segregation and inconsistent structure, post-processing has the potential to recover the homogeneity necessary for favorable properties.

Based on the knowledge that full melting changes structure and properties which can to some extent be recovered during post-processing, the following is proposed:

- As-printed samples will show elemental microsegregation which will cause broadening of the thermal transformation as well as unfavorable magnetic properties.
- Heat treatment with the purpose of compositional homogenization will improve properties of laser-deposited samples and restore functionality.
- Restoring compositional homogeneity will produce phase homogeneity since for these alloys phase is heavily dependent on the e/a ratio.

H1.2: Binder jet 3D printing will produce viable samples, after an optimized sintering step

During binder jet 3D printing (BJ3DP), feedstock powder is selectively bound at room temperature rather than being selectively melted. In the absence of melting, the feedstock powder is likely to retain much of its original structure, composition, and properties. Though preserving feedstock powder characteristics is beneficial, BJ3DP parts do still require post-processing treatments for densification such as pressureless sintering. Since sintering can be conducted in the solid state region, it is proposed that after a solid state sintering treatment, BJ3DP parts fabricated with MCE alloy powder will exhibit favorable magnetocaloric properties, including:

- adiabatic temperature change, ΔT_{ad}
- martensitic transformation temperature, M_T

H2.1: Sintering of mixed-powder samples will produce nearly homogeneous composition.

Solid-state sintering temperatures are near the melting points without forming liquid phases. At such high temperatures, atoms will have sufficient mobility to nearly homogenize composition within the sintering hold time. However, some microsegregation may persist in particles with less or longer diffusion paths due to relative isolation, size, or edge positioning.

H2.2: Density can be tailored per set of layers in multi-material prints

Kinetics of sintering are dependent on how quickly relevant atomic transport can occur, which is heavily influenced by homologous temperature (ratio of processing temperature to material melting temperature, T/T_m). For a multi-material part where the comprising materials have differing melting temperatures, the homologous temperature of each material will be different at a given sintering temperature. Homologous temperature affects sintering mechanisms and kinetics, and thus the final multi-material part will have separate density regions.

H3.1: Sintering will change lattice parameter through stress relief and homogenization

All samples will retain residual stress from ball milling, since no stress relief treatment was applied [193]. Heating up to the sintering temperature will relieve this residual stress and change the lattice parameter. As mentioned in H2.1, homogenization is expected to occur during the sintering process for mixed-powder samples. Homogenization will lead to an observation of lattice parameter change as unit cells adapt to their new compositions. For the layered multi-material parts, lattice parameter will change as atoms interdiffuse at the boundary and create a gradient of composition through the part.

H3.2: Multi-material layered parts will exhibit multiple phase transformations

Multi-material layered parts will have several layers of a single composition then several layers of another. During sintering, these compositions are expected to experience some diffusion at the compositional interface, but not enough for full homogenization. Therefore, it is anticipated that thermal behavior will show multiple transformations, corresponding to the single-composition far edges and the partly-diffused boundary section.

The first section of this project summary (Section 5.1) will address H1.1. The second section (Section 5.2) will address H1.2 and introduce H2. The third section (Section 5.3) will address H2.1 - H3.2.

4.0 Experimental Methods

This investigation has three components: fabrication by DLD, fabrication by BJ3DP, and *in-situ* monitoring of heat treatments for BJ3DP parts. These components of the investigation shared some common characterization and data analysis methods, so these are detailed first in Sections 4.1 and 4.2. Following these common characterization and data analysis sections, unique method details for each investigation component are presented in Sections 4.3-4.5 with a short digression in Section 4.5.1 to describe the design and workings of a custom built manual binder jet printer.

4.1 Characterization

4.1.1 Structure and Composition

4.1.1.1 Microscopy and Energy-dispersive X-ray Spectroscopy For standard optical microscopy (OM), a Zeiss Smartzoom 5 with a high magnification lens that spanned 100x-1000x magnification and a Keyence VHX-600 with a 20x-200x lens were used. For scanning electron microscopy (SEM) imaging and EDS, a Zeiss Sigma 500 field-emission SEM (FESEM) was used.

Energy-dispersive X-ray spectroscopy (EDS) is a composition analysis tool within an SEM which uses the characteristic wavelength X-rays emitted from electrons falling from higher orbitals in the inner shell to identify elements within a material. A few important considerations should be noted for EDS analysis: interaction volume, qualitative vs. quantitative measurements, and limited elements. The interaction volume of EDS is based on the energy of electrons within the incident beam and material density. With more energy, the electrons can penetrate further and spread more in the material. A higher density material will induce more collisions, slowing the electrons faster. Monte Carlo simulations can be employed to simulate interaction volumes where necessary [194]. At intermediate voltages

(15-20 kV) generally used for EDS analysis, the resolution due to interaction volume effects is on the order of 1 µm.

Qualitative analysis by EDS is a challenge that requires many considerations, including background signal, peak overlap, and sum peaks. The background for the X-ray spectrum is well-understood and originates from *Bremstrahlung* (braking radiation): when the electrical field of the atoms decelerates the electron beam [195]. Peak overlap can be seen when the characteristic X-ray wavelengths are similar for different elements. More overlap occurs at low energies (usually originating from the L energy shell), so peak identification can improve if beam energy is high enough to also elicit a response from the K energy shell. Pulse pileup occurs when multiple X-rays reach the detector at the same time and are recorded as one X-ray with a sum energy. Commercial software corrects for sum peaks and other spectral artifacts with a process called pulse pile-up correction, where X-rays are returned to their correct energies.

Quantitative analysis by EDS requires quantification and comparison of peak intensities from the unknown and a standard, collected under identical conditions [196]. After removal of Bremstrahlung X-rays and artifacts, peak identification is performed, and peak intensities are compared with a standard reference peak for the same element according to the k-ratio protocol, given in Equation 4.1.

$$k = I_{unknown}/I_{standard} \tag{4.1}$$

In semi-quantitative (or standardless) analysis, the spectrum is compared with spectra measured in the factory for the relevant elements. In fully standardized analysis, a known standard of similar composition as the unknown is measured in the same instrument as the unknown. For accurate quantitative analysis, the unknown must have a flat, polished surface so that no X-rays are trapped by surface topography, thus affecting peak height in the X-ray spectrum.

There are some limitations for the elements that can be quantified using the EDS technique. H and He do not produce X-rays. Li produces X-rays of energy too low to be detected by EDS. Other elements with low atomic number (less than 11) can be detected but are absorbed strongly by the material, and their peaks are subject to change based on bonding environment. C is a particularly difficult element to measure, as it can originate from contamination due to inadequate sample preparation or SEM chamber conditions.

4.1.1.2 Archimedes' Density Measurements Porous solids have several different densities that can be defined. The first is true density, which assumes the solid has no pores using the equation $\rho_{true} = m/V$, where m is the mass of the solid and V is the volume of the solid sample. Often, true density is measured for irregular shapes using Archimedes' principle, which uses the fact that a sample immersed in a liquid experiences upthrust equal to the weight of the displaced liquid. When a porous material is submersed, the open pores will fill with water and the closed will not. These occurrences can be leveraged to calculate apparent density using Equation 4.2:

$$\rho_{apparent} = \rho_{liquid}(\frac{m_1}{m_1 - m_2}) \tag{4.2}$$

where $\rho_{apparent}$ is the apparent density, ρ_{liquid} is the density of the liquid (usually water, $\rho = 0.001 g/mm^3$), m_1 is the mass of the dry sample, and m_2 is the mass of the submerged sample. The third measure of density is the bulk density (Equation 4.3), and is equal to the solid volume fraction.

$$\rho_{bulk} = \rho_{liquid}(\frac{m_1}{m_3 - m_2}) \tag{4.3}$$

m_3 represents the mass of the sample when the open pores are filled with water, measured by removing the submerged sample and gently drying the surface.

4.1.1.3 X-ray Diffraction For this investigation, a Bruker D8 XRD with a Cu-kα source was used to collect diffraction patterns via a LynxEye detector. Temperature regulation for Section 5.2 was achieved by forced air.

X-ray diffraction takes advantage of the constructive interference that arises when atomic plane spacing satisfies the Bragg condition:

$$n\lambda = 2dsin\theta \tag{4.4}$$

where n is an integer, λ is wavelength, d is interplanar distance, and θ is signal incident angle [195]. An idealized diffraction pattern for a given material has vertical lines at 2θ values where the Bragg condition is satisfied and with heights (intensities) determined by the structure factor (F_{hkl}):

$$F_{hkl} = \sum_{n=1}^{N} f_n e^{2\pi i(hu_n + kv_n + lw_n)} \tag{4.5}$$

where hkl is the reflection considered, uvw is an atom's coordinates, n is the atom considered, f_n is the atomic scattering factor, and N is the total number of atoms in the unit cell. F_{hkl} describes the sum wave scattered by all atoms in the unit cell. Even if a Bragg peak should be observed, the atoms of the unit cell may scatter deconstructively for a resulting structure factor of zero.

In a real diffraction pattern, peaks have a width as well as a height. This peak broadening is caused by machine parameters and also by crystallite size or lattice strain. Very small crystallites (in the nm range or less) effect broadening because there are not enough planes present for destructive interference to occur fully near the Bragg angles. Lattice strain, specifically nonuniform strain, broadens diffraction peaks because there is a distribution of tensile and compressive stresses within the lattice. Unit cells in tension will have a slightly increased lattice parameter, while those in compression will have a slightly decreased lattice parameter. These slightly-larger and slightly-smaller lattice parameters diffract at slightly different 2θ angles and combine into a single, broader peak.

Many other factors affect the resulting diffraction pattern of a material, one of which is its temperature. With a temperature increase, the amplitude of atomic thermal vibrations increases. These vibrations cause: 1) unit cell expansion and a corresponding decrease in 2θ, 2) a decrease in the peak intensities as described by the Debye-Waller factor, and 3) an increase in background scattering.

The discussed principles of X-ray diffraction also apply to neutron diffraction.

4.1.1.4 X-ray Microtomography For these experiments, a Bruker SkyScan 1272 X-ray microtomography (µCT) machine was used with 100 kV, 100 µA and a 0.11 mm Cu filter.

Reconstruction and analysis were performed using Bruker Corporation software provided by Micro Photonics, Inc. (Allentown, PA, USA): NRecon, Dataviewer, CTAn, and CTVox.

Tomography is also known as 3D or volume imaging, and is based on mathematical theory presented by Johann Radon in 1917 [197]. The process for tomography involves a series of projections that are used to infer the real object via mathematical reconstruction. For µCT specifically, an X-ray is directed at the object to be reconstructed, and a radiograph is formed on a detector behind the object that is dependent on the X-ray attenuation at each point in the object at that given position. Attenuation is based on X-ray density (scaled with atomic number Z^4, [198]) as well as thickness of material. After the single radiograph is formed, either the detector and source or the object are rotated about an axis perpendicular to the X-ray beam and the procedure repeats. Typically, the object is imaged through 180° rotation since all further information would be redundant.

Accuracy of 3D reconstructions in tomography depends on the method used, the sampling density, the instrument resolution, and the completeness of the data. There are many types of artifacts that can appear in the reconstructed data and care must be taken to mitigate the effects of artifacts while causing minimal changes to the data [199]. Some common artifacts include:

1. **Ring artifacts**: A result of imperfections in detector elements, ring artifacts appear on reconstructed images. These ring artifacts are reduced by calibrations prior to testing as well as filtering methods in post-processing. [200]
2. **Beam hardening and scatter**: Caused by preferential absorption of low-energy X-rays and a scatter inherent in a cone beam shape, beam hardening and scattering makes objects have an edge glow after reconstruction because the energy distribution of the beam is altered as it is partially absorbed and scattered. Beam hardening is mitigated by using physical filters of Al or Cu to block as many low-energy X-rays as possible for a given sample during scanning. Scattering is lessened by choosing samples that are as small as possible, and by placing them close to the source. Both effects are also corrected for by filtering methods in post-processing. [201]

3. **Poisson noise**: Low signal generates Poisson noise, which appears as dark and bright streaks in a reconstructed image. During scanning, Poisson noise can be reduced by increasing the X-ray dose. In post-processing, filtered back-projection reconstruction methods (most common methods, and used for this investigation) are unable to correct this artifact. However, iterative reconstruction methods can avoid the majority of Poisson noise by improving the image through multiple iterations. [202]

4.1.2 Magnetic and Thermal Properties

4.1.2.1 Vibrating Sample Magnetometry A Lakeshore 7407 (calibrated with a Ni sphere) was used for magnetic property measurements Section 5.1. A Quantum Design superconducting quantum interference device (SQUID) was used in VSM continuous sweep mode for the magnetic properties measurements of BJ3DP samples in Section 5.2. In a VSM, an electromagnet is used to generate a magnetic field within which the sample is vibrated. The sample vibration generates an induction field that is converted to a voltage by a set of pickup coils. Common plots constructed using a VSM are magnetization curves (magnetization vs. field, $M(H)$) and thermomagnetization curves (magnetization vs. temperature, $M(T)$). Some sources for error in VSM measurements are: sample mounting position and pickup coil positioning [203]. To avoid sample positioning errors, each sample must be centered in all three axes before testing. Pickup coil positioning should be held constant during each test, and calibration is necessary any time the pickup coils are moved.

An image of the SQUID used is shown in Figure 4.1. Sample size for the SQUID is very small; masses for Ni-Mn-Cu-Ga samples were between 1 and 3 mg. The SQUID system uses liquid helium and a cryopump for cooling. Samples were mounted with high vacuum grease to a quartz sample holder, then wrapped in Teflon tape. Within the machine, the pickup coils are within a span of about 16 mm, so the sample must always be much smaller than that or the signal will be inconsistent across the sample. On top and bottom, there are *right-hand* pickup coils and in the middle there is a two-turn *left-hand*

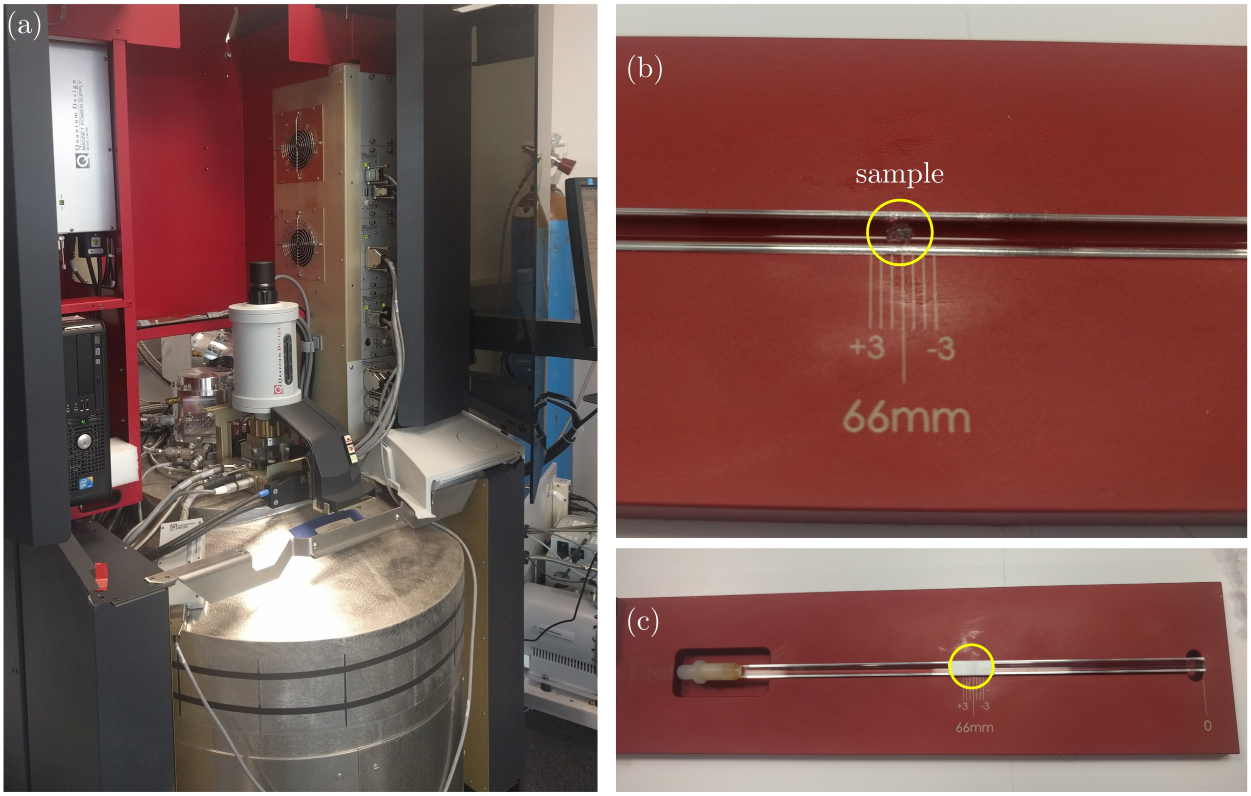

Figure 4.1: SQUID used in VSM mode and sample mounting for magnetic property testing. (a) SQUID, where the sample is inserted vertically beneath the black cap in the center of the image. (b) Mounted sample, adhered using vacuum grease, on the center of the quartz rod. (c) Final sample mounting, with the quartz rod wrapped in Teflon tape.

pickup coil; this means that signal from the center is positive and signal from the ends is negative. Using this setup, the system centers the sample in the magnetic field automatically.

4.1.2.2 Differential Scanning Calorimetry Differential scanning calorimetry (DSC) thermal property analysis was conducted using a Pyris 6 DSC for Sections 5.1.2.3 and 5.2.2.2, and a DSC 250 from TA Instruments attached to an RCS 90 cooling unit for Section 5.3.2.3.

Differential scanning calorimetry (DSC) is a technique used to evaluate the heat flow of a given material as a function of time or temperature. A differential scanning calorimeter measures the heat flow by employing the use of a reference material with known heat capacity, generally air [204].

Cooling/heating rates within a DSC have an effect on the signal: a higher rate produces a higher signal but has the detrimental effect of widening transformation peaks, since the material experiences a thermal lag [205,206]. In Ni-Mn-Ga magnetic functional materials, the DSC curve typically shows one peak each on heating and cooling, corresponding to the first-order martensitic transformation (on cooling) and its reverse (on heating). These two peaks are slightly offset in temperature location due to the energy barrier of the transformation. Peak locations can be quantified using the two-tangent method, where a tangent is drawn on the peak slope and on the background immediately before or after the transformation, and their intersection is identified as the transformation point.

In addition to the main peak, there can be a second-order transformation observed at the T_C of the austenite phase at a higher temperature than the main peak. In materials with magnetocaloric functionality, it is common to not observe the second-order transformation because it is obscured by the main phase transformation peak. This obfuscation is common because the functionality requirements for magnetocaloric materials dictate that it is beneficial for T_M and T_C to be very near each other, even overlapping.

4.2 Data Analysis

4.2.1 ImageJ and Fiji

ImageJ is an open source, multi-purpose image analysis software [207, 208], and Fiji is an updated version of ImageJ with many pre-installed plugins [209]. Images obtained on the Zeiss Smartzoom 5 optical microscope were in CZI format, which can be opened and manipulated using the BioFormats plugin for ImageJ [210], one of the pre-installed plugins for Fiji. Density and grain size measurements were conducted via image analysis in ImageJ or Fiji. Automatic thresholding methods were used, with a manual confirmation that thresholding was accurate and adjustments made as needed. Grain boundary distinctions were occasionally made by manually drawing visible boundaries when they could not be distinguished by thresholding alone.

4.2.2 FullProf

FullProf is an open-source software for neutron and X-ray diffraction data analysis [211]. Though the program is very powerful and versatile, one of the more straightforward uses it has is refining phases present and their lattice parameters in WinPLOTR [212]. This is of course delicate work and includes prequisite knowledge, i.e. likely phases present and their approximate lattice parameters. It is also necessary to have a high signal-to-noise ratio (SNR) in the XRD data for diffraction pattern fitting. Even with a reasonable idea of the phases present and a high SNR, it can be difficult to determine the true best fit of the data. For example, one of the goodness of fit evaluation parameters is χ^2, which approaches 0 for a good fit, though this is not universally true. Sometimes simply adding four phase options or a monoclinic phase can produce the same or a lower χ^2 than the true fit of the correct two high-symmetry phases. The output for peak fitting includes: *a*) the raw data curve *b*) peak indicators for input phases and *c*) a difference curve that indicates the discrepencies between the raw data and the calculated peaks.

4.3 DLD Fabrication Investigation

50 g of $Ni_{43}Co_7Mn_{39}Sn_{11}$ at.% powder for DLD parts was provided by collaborators after being melt spun and then mechanically ground. Powder size was characterized via 35 optical and scanning electron micrographs from cold mounted, polished samples as well as unmounted particles (imaging and ImageJ analysis details in Section 4.1). 3D powder size analysis was conducted from µCT data. For both methods, a lower measurement limit of 5 µm was observed due to resolution limits.

Samples produced by DLD were five layers high, each layer consisting of two neighboring parallel lines. $Ni_{43}Co_7Mn_{39}Sn_{11}$ was deposited onto a 2 x 2 x 0.25 in. 99.99% nickel substrate using an Optomec LENS® 450 DLD system with a 1070-nm continuous wave ytterbium-fiber laser (spot diameter 570 µm). Argon was used as a shielding gas flowing over the melt pool. Since only 50 g of powder were available, no optimization of parameters was possible, though small adjustments were made during printing to attempt to compensate for inconsistent flow causing overbuilding.

Two categories of samples resulted from DLD printing: properly built (PB) and overbuilt (OB). The resulting categorization was not a result of deposition parameter changes alone, as samples with identical deposition parameters had the potential to become either PB or OB, as can be noted from Table 4.1 containing all sample designations and printing parameters. Complete characterization was performed on samples PB2 (in Section 5.1, simply PB) and OB4 (in Section 5.1, simply OB).

A Princeton Scientific Corps. wire saw was used to cut samples in half parallel to the laser scanning direction; one half was cold mounted in epoxy and polished to a final step of colloidal silica and the other was kept in the as-printed state. Mounted samples were examined with SEM-EDS. After characterization in the as-printed state via DSC and VSM for thermal and magnetic property measurements, unmounted samples were encapsulated in quartz ampoules with an argon-purged vacuum atmosphere and annealed at 1000 °C for 4 hours then air cooled. Heat treated samples were hand polished and final surface preparation was achieved with ion milling before SEM-EDS examination.

Table 4.1: Printing parameters for DLD $Ni_{43}Co_7Mn_{39}Sn_{11}$. Note that powder feed rate is a machine parameter in rotations per minute (rpm), while powder mass flow rate is estimated from the corresponding feed rate based on experiments.

Sample	**Laser power** [W]	**Layer height** [mm]	**Powder feed rate** [rpm]	**Powder mass flowrate** [g/min]	**Hatch spacing** [mm]
PB1	200	0.25	5	2.0	0.25
PB2	300	0.25	5	2.0	0.25
OB1	200	0.25	5	2.0	0.25
OB2	200	0.25	5	2.0	0.25
OB3	200	0.51	6	2.5	0.51
OB4	250	0.25	5	2.0	0.25
OB5	200	0.51	4	1.5	0.51

4.4 BJ3DP Fabrication Investigation

300 g of powder for BJ3DP Ni-Mn-Cu-Ga was fabricated from argon-atmosphere induction melted ingots made with high purity (99.99+ %) elemental Ni, Mn, Ga, and Cu. Based on a publication by Sarkar et al. showing large ΔS values for temperatures above room temperature in $Ni_{50}Mn_{18.75}Cu_{6.25}Ga_{25}$ at.%, this composition was chosen as the target [91]. Elements were measured in wt.% to a nominal composition of $Ni_{50.00}Mn_{18.75}Cu_{6.25}Ga_{25.00}$ at.%. Ingots were ground in a planetary ball mill and sieved to a particle size of < 106 µm.

Powder was used to fabricate cylindrical parts of 5 mm height and 10 mm diameter with an ExOne X-1 Lab powder bed binder jet printer, using ExOne Solvent Binder 04. For printing the following parameter values were used: layer height 100 µm, spread speed 20 mm/s, feed/build powder ratio of 2, drying time 40 s, and binder saturation 80%. Parts were cured at 200 °C for 8 h then de-powdered. Sintering for densification was performed in an encapsulated quartz tube with an argon-purged vacuum atmosphere and a Ti sponge oxygen getter, with a 5 °C/min ramp to 1080 °C, 2 h hold time, and air cool.

Table 4.2: Nominal, ingot average, and BJ3DP part compositions with ± values representing standard deviation across all measurements. Ingot average is calculated from EDS data obtained from each of eight ingots, and EDS data for the printed part is evaluated excluding carbon.

Composition, at.%	**Ni**	**Mn**	**Cu**	**Ga**
Nominal	50.00	18.75	6.25	25.00
Ingot average	48.5 ± 1.4	17.8 ± 0.4	8.0 ± 0.9	25.7 ± 1.0
BJ3DP printed part	49.5 ± 0.3	19.1 ± 0.1	6.6 ± 0.2	24.8 ± 0.2

After cutting by wire saw, cold mounting in epoxy and polishing, room temperature microstructural data was collected by SEM-EDS, OM, and µCT (see Section 4.1 for details). Table 4.2 presents the nominal and average semi-quantitative EDS-measured composition (from area scans) of all eight ingots that were combined after ball milling into powder, along with the final EDS-measured composition of the printed part matrix. Between the nominal composition and the final composition of the part, only a < 1 at.% difference was observed. Despite small fluctuations in individual element concentrations, the electronic concentration (e/a) was constant at 7.75, indicating a propensity for similar structure and properties as discussed in Section 2.4.

Porosity was evaluated through: 1) Archmedes' method, using the assumption of single martensitic phase to calculate true density; 2) µCT; and 3) image analysis using ImageJ software.

Thermal, structural, and magnetic properties were analyzed by DSC (5 °C/min), XRD, and SQUID, respectively. XRD was performed on a $(1.84 \times 1.84 \times 4.14)$ mm^3 rectangular prism cut from the printed and sintered part. SQUID measurements were performed between -23 °C and 67 °C under applied magnetic fields up to 7 T, and the data was used to construct the $\mu_0 H - T$ phase diagram and to calculate the indirect MCE via the Maxwell relationship

(Equation 2.3) with the H_1 field equal to 0:

$$\Delta S_m(T,H) = S_m(T,H) - S_m(T,0) = \int_0^H \frac{\partial \mu_0 M(T,H')}{\partial T} dH' \tag{4.6}$$

Direct measurements of MCE were conducted on a custom-built calorimeter as described in detail in Section 4.4.1. The applied magnetic field was 1.96 T (hereafter rounded to 2 T). As noted in Section 2.3, sample history is very important when measuring the MCE. According to the established protocols, before each $M(H)$ curve in SQUID or direct MCE measurement, the sample was heated above the austenite finish temperature before being zero-field cooled to the testing temperature.

It should be noted that the thermocouples in each instrument (DSC, SQUID, custom calorimeter) have varying positions, calibrations, and sensitivities, leading to inherent discrepancies in nominal readings across the techniques. To compensate for this variation, thermomagnetization curves were shifted along the temperature axis by a few degrees to coincide with the other results. In addition, samples were different pieces and sizes from the original part, measuring from 2-100 mg depending on the instrument's requirements.

4.4.1 Direct MCE Testing

Direct MCE (ΔT_{ad}) measurements were collected from a custom modified calorimeter built by EHU-UPV collaborators [45]. The main components of the system are:

1. Power sources for the heater, magnet, and electrovalve for piston motion
2. Digital to analog converter cards
3. Data acquisition card
4. Vacuum pump
5. Hall probe to measure the field

Components and accessories of the tester are labeled in the photos in Figure 4.2. The sample holder is ceramic, and a thermocouple is sandwiched between two pieces of sample, shown in Figure 4.3b. Thermal conductivity was ensured with silver paint around the sample and thermocouple (Figure 4.3a). Finally, the sample assembly was wrapped in Teflon tape

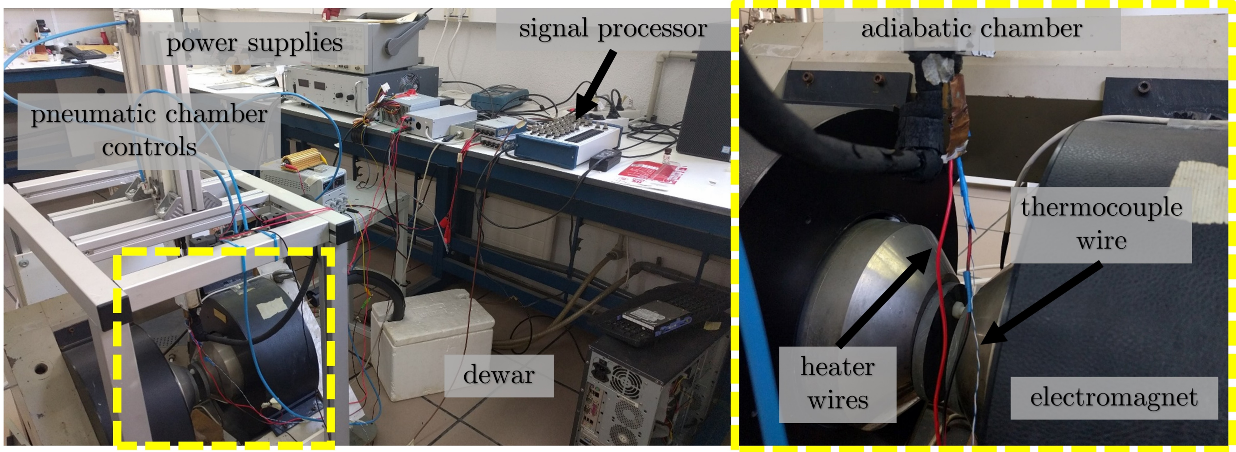

Figure 4.2: Adiabatic tester for obtaining direct MCE measurements.

and inserted into the sample chamber (Figure 4.3c). For the measurements in Section 5.2, the sample was held outside of the magnetic field while the temperature stabilized. Then, at the stabilized temperature, the piston was activated, which accelerated the sample into the magnetic field (maximum of 1.96 T) in less than one second. The temperature change due to insertion into the magnetic field was measured directly by the sandwiched thermocouple. Calibration of the system was performed with pure Gd. According to necessary protocols, between each measurement the testing sample was heated above the austenite finish temperature. Cycling measurements were conducted by holding temperature constant through manual airflow control and dropping the sample into the magnetic field for each measurement.

4.5 In-Situ Monitoring of BJ3DP Post-print Heat Treatments

A full overview of samples can be seen in Figure 4.4. For the E3 beamline, diffraction data from *in-situ* heat treatment monitoring was assessed for peak location and Gaussian fit with parameters of intensity, FWHM, and 2θ.

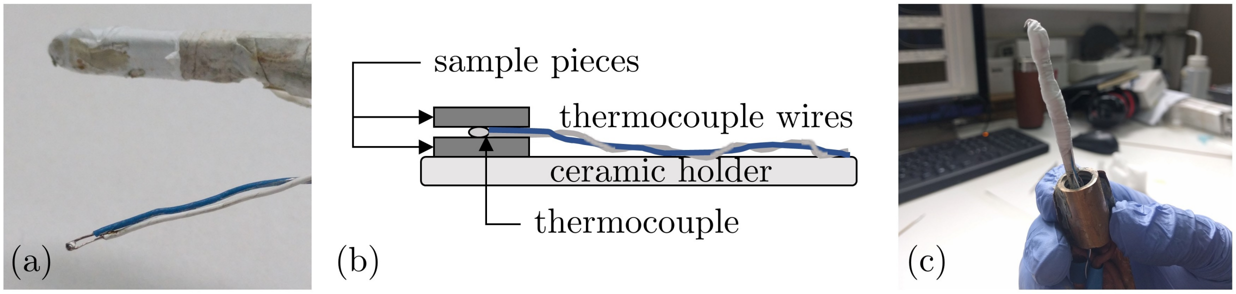

Figure 4.3: Sample mounting for custom calorimeter: (a) empty ceramic holder and thermocouple, (b) schematic of mounting setup, (c) mounted sample wrapped in Teflon tape.

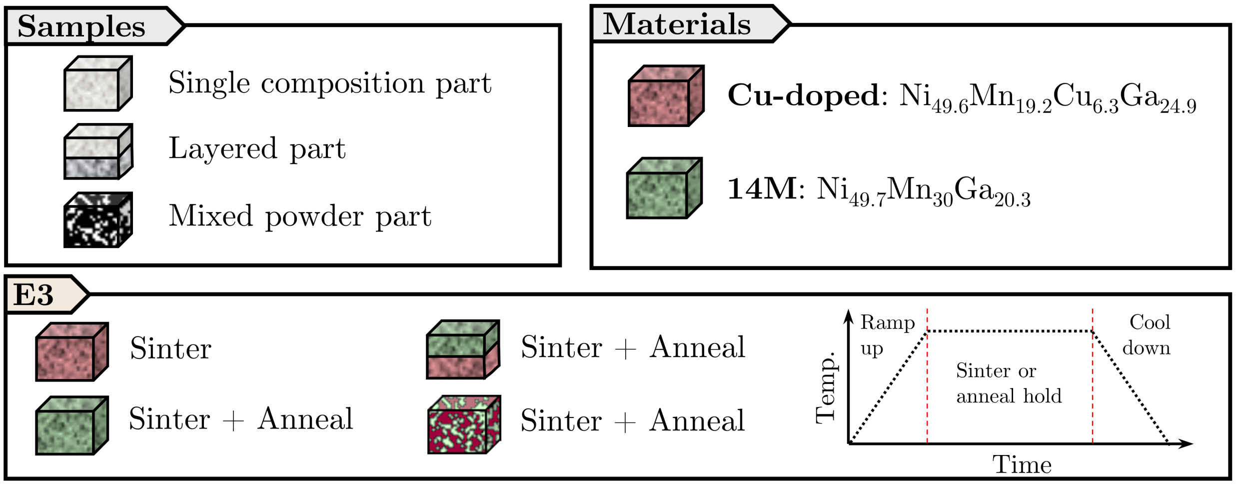

Figure 4.4: Overview of experiments and analysis conducted for the E3 beamline. The three types of samples were: single-composition, layered, and mixed-powder. Materials used were Ni-Mn-Ga and Ni-Mn-Cu-Ga alloys. At the E3 beamline, four different samples underwent *in-situ* heat treatments that included ramp up, hold, and cool down segments.

Figure 4.5: Exemplary set of 4 green samples produced by a single manual printing run. Each sample is approximately (5 × 5 × 4) mm^3. In this image, three of the samples are resting on the x-z or y-z plane, while the part in the foreground is resting on the x-y plane, where the z axis is in the build height direction.

All samples were 4 mm in the build direction (z), with x and y dimensions of 5 mm, fabricated with the custom-built binder jet 3D printer described in Section 4.5.1. Two ball-milled powder compositions were used, both sieved to < 63 µm: $Ni_{49.7}Mn_{30.0}Ga_{20.3}$ and $Ni_{49.6}Mn_{19.2}Cu_{6.3}Ga_{24.9}$ at.%. The $Ni_{49.7}Mn_{30.0}Ga_{20.3}$ is hereafter referred to as NMG. Since Cu was the doping element in $Ni_{49.6}Mn_{19.2}Cu_{6.3}Ga_{24.9}$, this composition is hereafter referred to as "NMG-Cu". In addition to pure samples of each composition, samples were made by mixing powder (50% NMG and 50% NMG-Cu by weight, agitated in a sealed container before printing to ensure mixing, designated by "mixed") and by layering (designated by "layered"). All samples had 16 total 250 µm thick layers. Layered samples had 8 layers of one composition, then 8 layers of the second, while mixed-powder samples were mixed powder throughout.

Four printing runs were conducted, each of which produced 4 samples. An exemplary set of 4 samples is shown in Figure 4.5. Layers are visible, but parts are structurally sound and withstood de-powdering. Beneficial for integrity of the samples was the angular nature of the ball-milled powder since their multiple points of contact decrease flowability (as compared to spherical powder particles).

Post-printing processing consisted of a curing step at 200 °C for 2 h. Green, cured samples were then transported to the Helmholtz Center Berlin for Materials and Energy (HZB) E3 beamline [213, 214] for *in-situ* monitoring of heat treatments.

Beamline setup is shown in Figure 4.6. Heating and atmosphere control were achieved using a vertically-mounted furnace unit attached to the sample containment unit, and thermocouples were mounted both inside and outside of the unit. During heat treatment, samples were encapsulated with a Ti sponge oxygen getter supported on quartz wool in either a quartz ampoule (NMG, mixed, layered) or aluminum holder (NMG-Cu) with argon-purged vacuum atmosphere at approximately 965 mbar. Interaction volume of the neutron beam encompassed the entire $(5 \times 5 \times 4)$ mm^3 cuboids, which must be kept in mind when evaluating especially mixed vs. layered samples. Experimental conditions for NMG-Cu were slightly unstable, and the sample setup slipped partway out of the beam during the sintering ramp up segment. The sample position was corrected for the hold segment, and the beam slit was then widened to ensure full sample coverage. Wavelength of the beam was 1.4722 ± 0.0004 Å and the area detector for collection was 300×300 mm^2 (256×256 pixels) detecting from a constant 10° 2θ range centered on 42° 2θ. Data was collected in 60 s monitor scans, and sample rotation ω was held constant throughout ramps and sinter hold. During the annealing hold, ω was varied in 11 steps from 0° to -20°, but only 0° data is used in this study to ensure constant diffraction volume.

The heat treatment processes are shown schematically in Figure 4.7a for sintering and Figure 4.7b for annealing. Ramp up for sintering occurred at 20 °C/min until decreasing to 5 °C/min from 1040 °C to 1080 °C, where a 120-min hold was carried out. On cool down, the initial ramp was 20 °C/min to 700 °C for 11 min then a slow 2.5 °C/min ramp to 650 °C for another 11 min. These holds at 700 °C and 650 °C were to encourage increased ordering at the transition out of the disordered high temperature B2 phase. Final ramp to room temperature was again at 20 °C/min. For the annealing treatment a 10-min hold (to enable integration of area detector images at those temperatures) was allowed at 100 °C increments during the heat up and cool down ramp segments, which otherwise also occurred at 20 °C/min. Annealing hold was 420 min at 1040 °C. The annealing step was not able to be conducted for NMG-Cu.

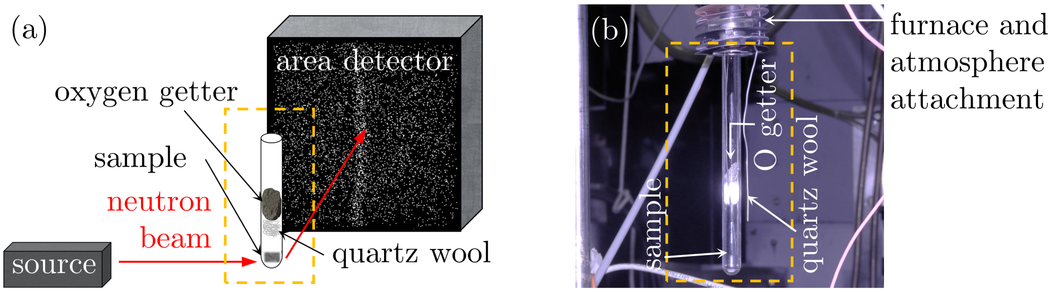

Figure 4.6: Setup for neutron diffraction at beamline E3. (a) Schematic of neutron beam diffracted by the sample onto the area detector. (b) Photo of sample setup: oxygen getter, supporting quartz wool, and furnace/atmosphere attachment for the quartz tube.

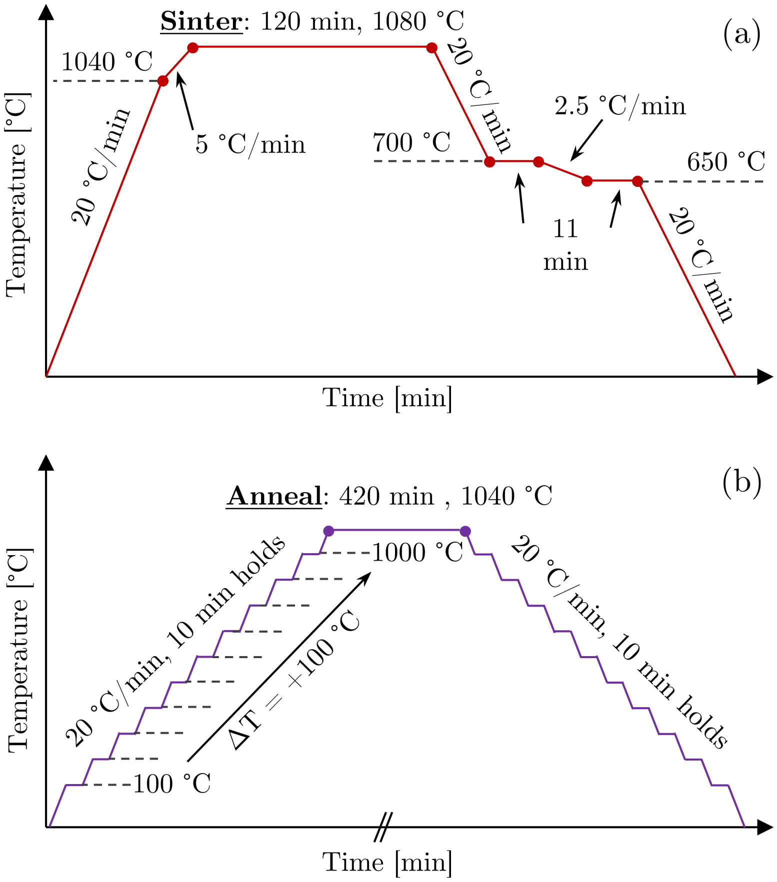

Figure 4.7: Temperature profiles for (a) sintering and (b) annealing processes.

Detector image extraction was performed using the beamline-provided software caressplorer. Diffractograms were combined and extracted, background-subtracted, and fit with Gaussian peaks in STeCa2 [215]. Peak intensities were all normalized by the average monitor value (neutron signal counter between the monochromator and the sample)) for the image set. Image combination was done for sintering ramp up with 5 images or all images in a 20 °C range, whichever came last. Ordering hold stable temperatures during sintering cool down were combined together. During both sintering and annealing holds, combination was performed in 5-image stacks. Each annealing hold image was collected about 12 minutes apart (since ω was varied during that time but only 0° data is used in this study), so total time elapsed during each hold combination segment was approximately 51 minutes. For annealing ramp up and cool down, there were 10-min intervals built into the temperature profile, and all images within the plateaus were combined. To capture more accurately the deterioration of the austenite peak into multiple martensite peaks, temperatures below ordering in the cool down segments were split into 5-image stacks. Temperatures are reported as an average of the temperatures at the beginning of the 60 s scan time for all images within the combination intervals.

Temperature and pressure within the enclosed quartz ampoules were monitored over time (Figure 4.8) in order to ensure proper temperature and to identify any pressure spikes or dips. No anomalies were found, so it was concluded that ampoules remained sealed throughout the heat treatments and the volume of any vapor produced by binder burnout was insignificant compared to the total volume of the ampoules.

Final structure of post-annealing samples was examined using SEM-EDS and DSC (10 °C/min) (details in Section 4.1). To reveal cross-sections for SEM-EDS, samples were cut in half perpendicular to layer boundaries with a Princeton Scientific Corps. wire saw, cold mounted in epoxy, and polished to a final step of acidic alumina. Density was estimated using image analysis in Fiji (see Section 4.2.1) from a single cross-section, avoiding a few areas where material was lost during polishing.

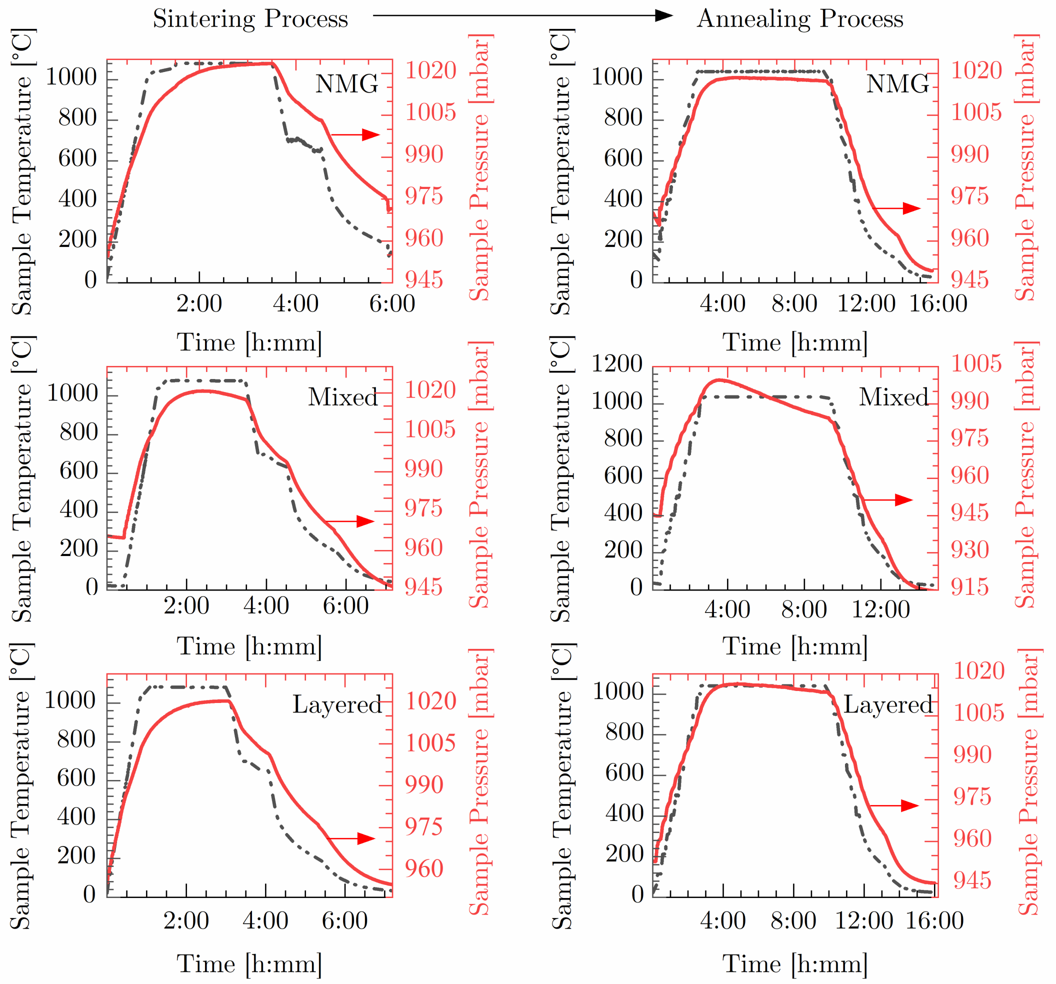

Figure 4.8: Time-temperature-pressure plots for annealing and sintering processes at the E3 beamline.

4.5.1 Custom Powder Bed Binder Jet Printer

Though binder jet printing is promising for 3D printing without internal stresses, melting, or supports, the feasibility of small-scale research on binder jetting is limited. The smallest build box available (on the discontinued ExOne X-1 Lab) is 175 mm^3 and requires as much as 300 g of powder for a successful build, though much of the powder can be recovered. With proper capabilities however, small-scale laboratory BJ3DP research experiments could be conducted on slightly-adjusted compositions, layered or gradient compositions, and aligned powders with an *in-situ* applied magnetic field.

With these machine deficiencies and goals in mind, a manual, small-scale binder jet 3D printer was designed and produced. The machine is relatively simple and could be reproduced by any research laboratory with access to several polymer 3D printing technologies and a basic machine shop.

4.5.1.1 Printer Components In general, the printing process of the custom binder jet printer mimics that of commercial printers, just with the steps being far more manual. Powder is deposited then spread flat, binder is deposited and dried, the stage is lowered by a distance equal to the layer height, and the process repeats. Powder deposition is achieved by sliding one of two small feeders over top of the stage and allowing powder to fill the empty layer thickness. A knife-edge spreader is dragged across the powder surface to flatten it. A laser-cut acrylic template is placed over the stage and the rest of the machine is also protected by specially-cut acrylic sheet before the binder is sprayed with a dosed spray bottle towards the stage from a pre-determined position. Without the template and covers, binder would indiscriminately cover the machine and soak into the powder feeders. The cover and template are removed and a heat lamp is placed using a base designed to sit atop the machine and hold the heater at a constant distance from the powder bed. After 30-45 s of drying time, the heater is removed and the stage is lowered using a micrometer. These steps are shown pictorially in Figure 4.9.

The manual printer consists of: (a) frame, (b) stage assembly, (c) powder spreading mechanisms, (d) binder drying lamp, (e) powder recapture methods, and (f) transfer assem-

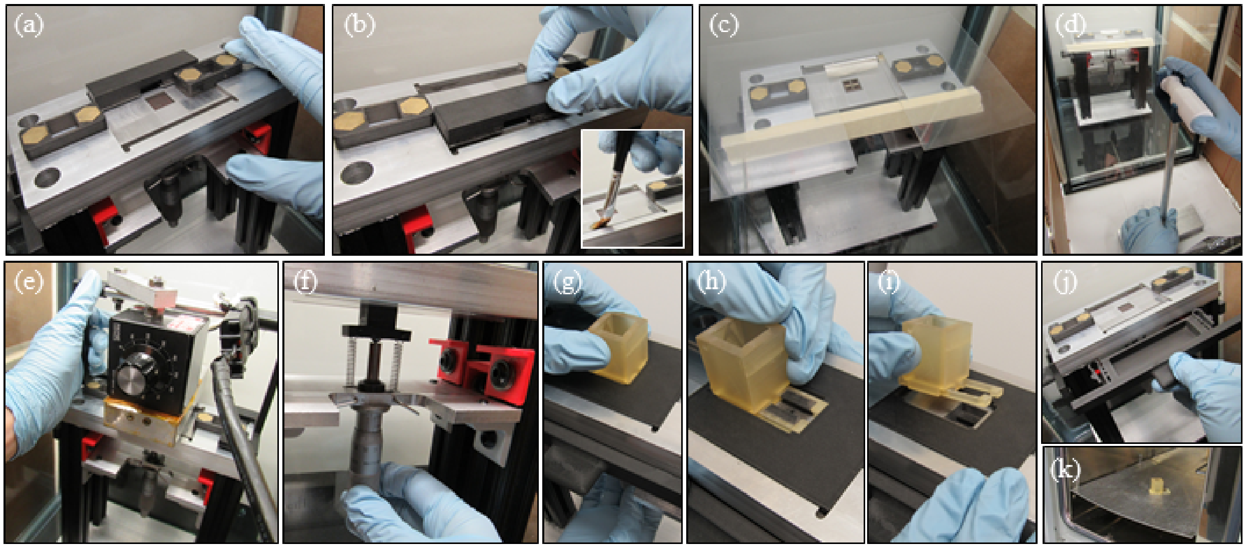

Figure 4.9: Demonstration of the manual printing process, detailed in Section 4.5.1.2.

bly. These components are shown from the 3D computer model in Figure 4.10. In addition to the main components, there is a removable electromagnetic coil that can be turned on to generate a magnetic field affecting the powder bed.

(a) The frame consists of a base, four posts with a center attachment to support the micrometer, and a top plate. The top plate has a rectangular depression with two extensions parallel to the longer dimension to contain the powder beds. These extensions, as well as both full sides of the rectangular depression, end in narrow through-cuts to allow powder to fall off the top plate into the powder recapture system.

(b) The stage assembly includes a shaft with micrometer attachment to allow for precise layer thickness adjustment. Shaft motion is transferred to the stage mount by a single point of connection via bearing ball. The stage is preloaded by two small springs on opposite corners of the stage mount and anchored into the frame, which resist the upward force applied by the micrometer and shaft. A powder bed stage is attached to the stage mount via a dovetail connection and can be easily removed when the stage mount is fully raised. High-temperature felt is adhered to the lower face of the stage, in contact with the stage

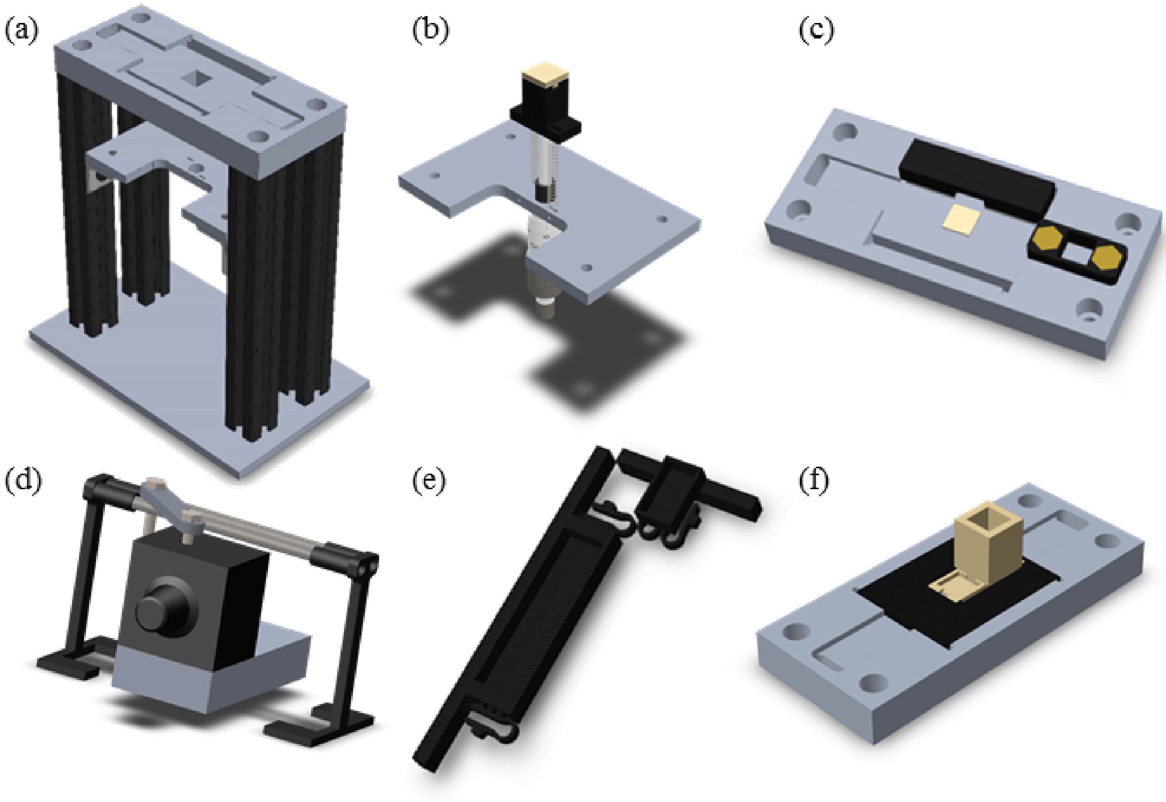

Figure 4.10: 3D computer models of manual printer components, disassembled. The frame (a) supports all permanent components. Mounted on the lower plate of the frame, the stage assembly (b) contains the stage mount and stage itself connected to the micrometer. On the top plate of the frame, the powder spreading mechanisms (c) sit in pre-defined grooves. Separate from the frame, the binder drying lamp (d) is placed on the top plate during the drying step. Also separate from the frame, powder recapture methods (e) aid in powder recycling, and the transfer assembly (f) enables moving the completed build bed to post-processing.

mount when attached, in order to prevent powder from falling between the walls and stage mount.

(c) Powder spreading is achieved through use of powder feeder beds and a spreader, all of which were produced by polymer 3D printing. There are two powder feeders that can be filled with different powder compositions. Each feeder is weighted with two pieces of brass to ensure constant contact with the top plate. Additionally, each feeder has a square through-hole in the center for powder stock. The feeder side in contact with the top plate has felt adhered to the side furthest from the powder bed in order to clean the top plate as it slides. This prevents sticking due to powder buildup. After powder has been deposited by the feeder, the spreader is pulled over the bed perpendicular to the feeder movement. Spreading levels the print bed and removes any excess powder, placing it into the powder recapture system. This rectangular spreader bar has felt in contact with the top plate, and a pointed edge over the location of the build bed.

(d) After the binder is sprayed onto the powder bed, it must be dried before the next layer can be properly spread. Drying is achieved by placing a heating lamp ~ 1 mm above the print bed for 45 s. In order to maintain consistent positioning, the lamp is mounted on a 3D printed stand that is placed on the top plate during drying.

(e) Powder recapture during printing without an electromagnetic coil is achieved by trays that are inserted between and locked into the supporting posts. When the coil is inserted, the trays on the long dimension are replaced by sleeves that fit into the narrow through-cuts on the top plate.

(f) After printing, the bed of powder and binder must be transported into a curing oven at between 180 and 200 °C for at least 2 hours (for small parts). In order to prevent a delay in production, a transfer assembly was created to transfer the finished print bed to the oven. First, a 3D printed alignment plate is placed over the rectangular section of the top plate. Then, a transfer slider is inserted into the alignment plate, with the transfer box fitted onto it. This slider and box are fitted with the same dovetail that is used on the powder bed stage. To complete the transfer, the box is placed over the bed and the stage is raised until the dovetails align. The box and stage are then slid along the transfer slider until both are seated in the solid section of the slider. The entire transfer assembly is removed from the top plate and placed into the oven. In order to withstand the necessary temperatures, the transfer slider and box, as well as the powder bed stage are 3D printed from high temperature resin.

4.5.1.2 Operation Process The printing process is pictured step-by-step in Figure 4.9:

(a) deposit powder by swiping feeder over the print bed
(b) flatten the bed with the spreader and use a brush to clear excess powder
(c) use covers to protect the printer from binder spray and apply a template to the powder bed
(d) spray binder to evenly coat the powder surface
(e) remove protective covers and dry the binder by placing the heat lamp on top of the printer for 30-45 s
(f) lower the stage by the layer thickness and repeat steps (a) through (f) until the part is complete
(g) attach the transfer assembly and raise the powder bed to transfer position
(h) slide the transfer box with attached build stage over to the removal position
(i) remove the transfer box with the stage attached
(j) remove and empty the powder recapture trays
(k) place the transfer assembly with stage and powder bed in an oven to cure at 180-200 °C for at least 2 h

5.0 Results and Discussion

5.1 DLD Fabrication

5.1.1 Overview

A summary of DLD fabrication of Ni-Mn-Co-Sn is given in Figure 5.1 (related publications [101,191]). Mechanically ground $Ni_{43}Co_{7}Mn_{39}Sn_{11}$ powder was used in DLD to fabricate samples, which were then homogenized. Both as-deposited and homogenized samples were characterized for structural and thermal properties to determine magnetocaloric viability. Heat treated samples were more viable than as-printed due to more martensitic phase, homogenized composition, and clearer phase transformations. However, build inconsistencies make powder feeding of granular powder undesirable. Also, full-melting techniques degrade control of composition and functional outcomes in magnetocaloric materials. Further study could render DLD a viable option for production of magnetic refrigerants, but non-melting techniques have the benefit of preserving feedstock powder features.

5.1.2 Results and Discussion

5.1.2.1 Powder Morphological observation showed particles to be irregular (according to ASTM B243 13), as expected from pulverized powder of brittle material. 3D visualization with µCT confirmed that powder was mostly granular (approximately equidimensional, non-spherical). Figure 5.2 shows particle size distribution plotted as circle- or sphere-equivalent diameter as calculated by image analysis (5-176 µm) and µCT (5-138 µm). The lower limit of 5 µm reflects resolution limits and the upper end of particle sizes has a positive deviation away from the lognormal line. Recommended spherical particle range for DLD is 44 to 150 µm [216, 217].

5.1.2.2 Structure and Composition Two types of samples were observed after deposition: properly built (PB) and overbuilt (OB), and one example of each was chosen for

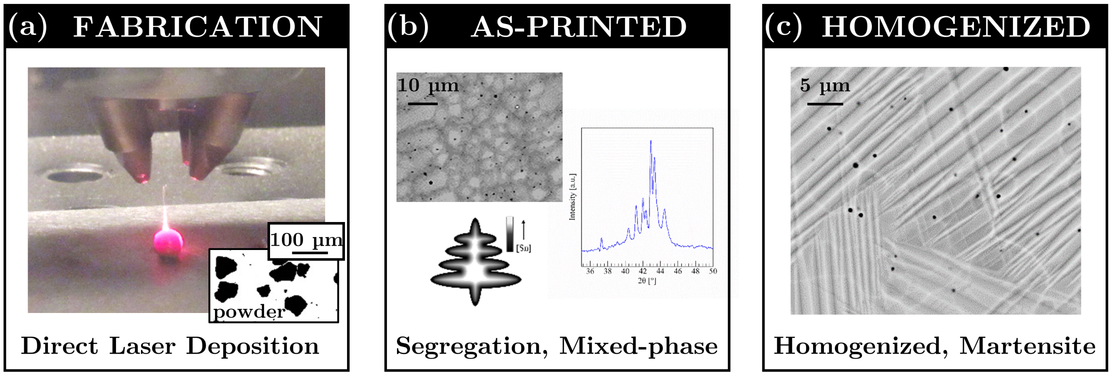

Figure 5.1: Summary of DLD fabrication of Ni-Mn-Co-Sn. (a) Fabrication using granular powder. (b) As-printed samples were multi-phase, cellular, and dendritic. (c) Homogenized samples were consistent in composition and phase, showing improved transformation.

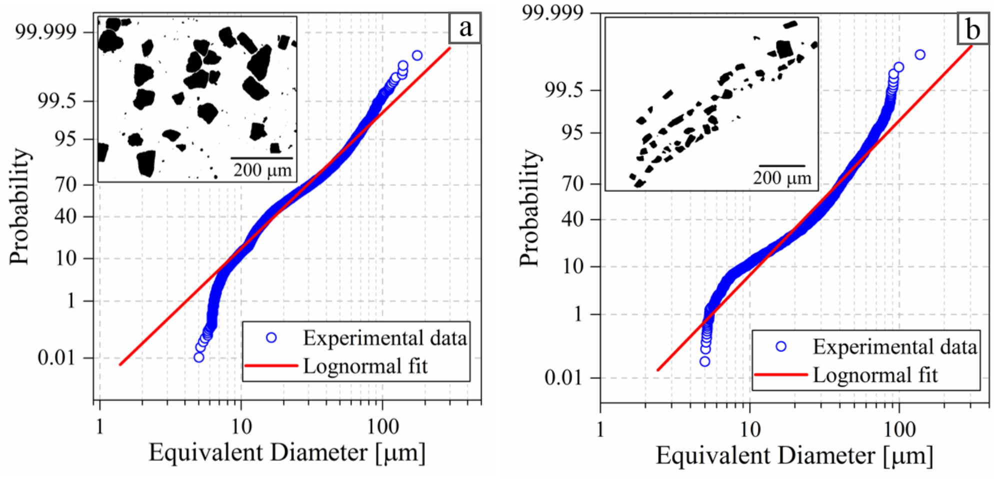

Figure 5.2: Powder size distribution compared to a lognormal fit. (a) Data collected using optical and electron microscopy. (b) Data collected using X-ray µCT. Insets are exemplary binarized images from each technique, showing powder shape and size in projection for (a) and in a 2D slice for (b).

Table 5.1: Feature descriptions of sections within the PB and OB samples.

Section	Melt pools	Layers	Microstructural features
1	Consistent spacing	Thin, consistent height	Fine, elongated cells
2	Inconsistent spacing	Thicker, inconsistent spacing	Dendrites, columnar grains

comparison of the microstructure produced in this material after laser melting and homogenization. Figure 5.3 shows the lengthwise cross sectional views of the PB and OB samples, with the layer boundaries shown as dotted grey lines. As detailed in Table 5.1 and indicated with grey and white area fill in Figure 5.3, there are two distinct sections of the samples. In both samples, there is a bottom section that has relatively even layer boundary spacing, and melt pool boundaries are also in consistent intervals. Nearer to the top however, the layer boundaries become far apart or inconsistently placed. Hereafter, the sections will be referred to by the sample name and section name (PB-1, PB-2, OB-1, OB-2).

Figure 5.3 also shows an overview of the microstructural features observed through backscatter electron images in both the as-built and homogenized samples. Both the PB-1 and OB-1 as-printed sections had a relatively fine microstructure of elongated cells, with a transition to columnar grains and then relatively large (tens of µm long) dendrites by the top of both PB-2 and OB-2. Magnified views of these microstructural features are shown in Figure 5.4.

After homogenization, layer boundaries were blurred in both samples as seen in Figure 5.4e-h. Equiaxed grains developed in the bottom PB-1 and OB-1 sections, as well as some towards the top sections (Figure 5.4e,g,h). Columnar grains remained unchanged after homogenization (Figure 5.4f), and twinning was – in contrast to as-deposited samples – ubiquitous, implying a uniform or nearly uniform presence of the martensite phase, indicating a well-homogenized sample.

Composition determined by EDS varied from the nominal $Ni_{43}Co_{7}Mn_{39}Sn_{11}$, particularly in the dendritic region shown in Figure 5.4. Interdendritic regions were approximately $Ni_{43}Co_{12}Mn_{39}Sn_{6}$ average from all samples, and matrix (excluding interdendritic regions)

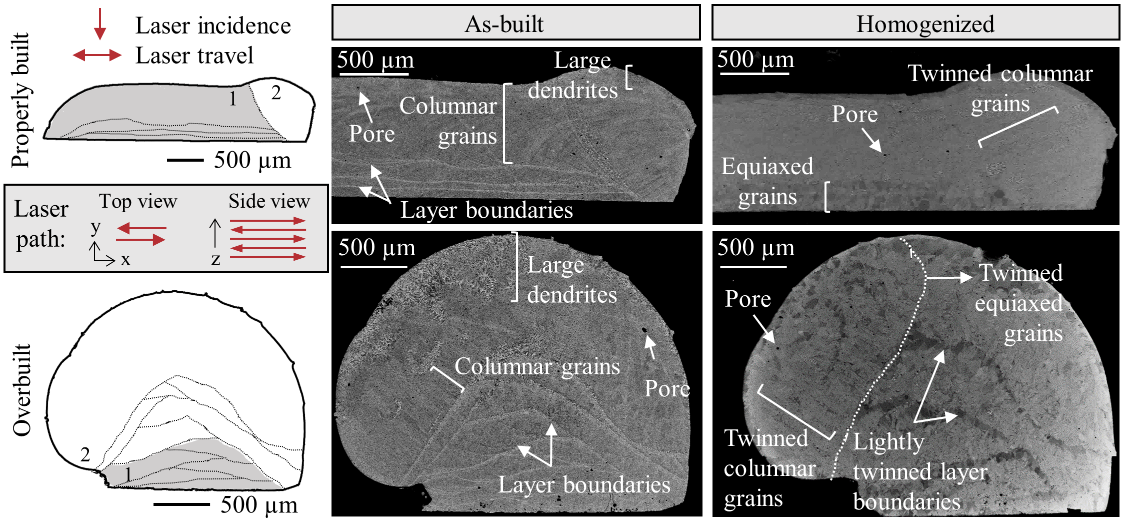

Figure 5.3: Microstructure effects of DLD manufacturing and homogenization of Ni-Mn-Co-Sn with (a) as-deposited OB sample, (b) homogenized OB sample, (c) as-deposited PB sample, and (d) homogenized PB sample.

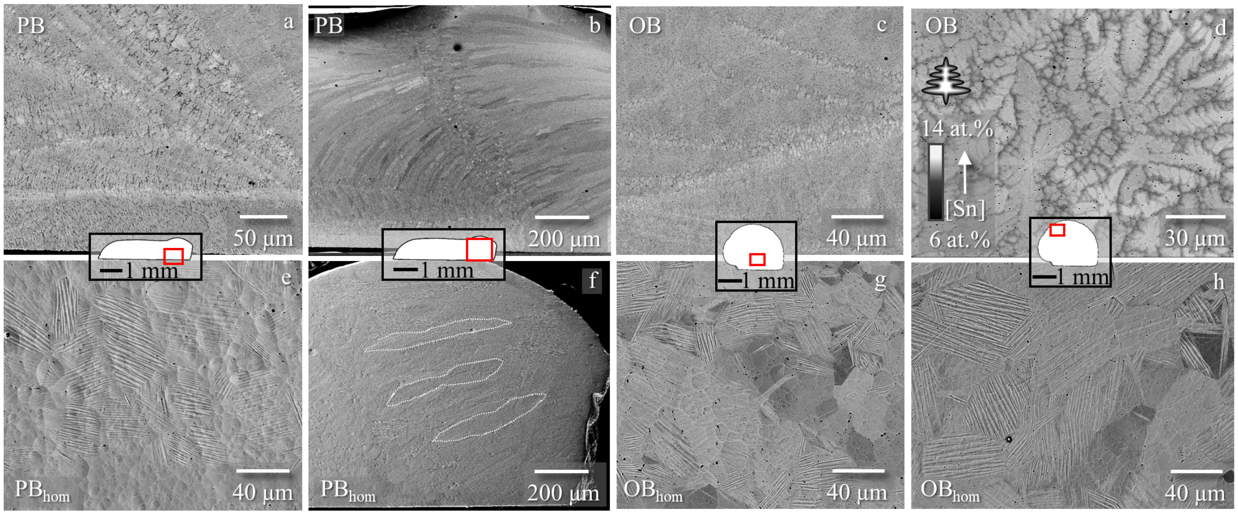

Figure 5.4: Examples of microstructural features in (a–d) as-built and (e–h) homogenized samples and level of Sn microsegregation within the dendritic region of (d) as-built OB. Insets indicate region from which the as-built/homogenized micrograph pair was obtained. White dotted areas in (f) trace columnar grains.

Table 5.2: EDS composition data averaged over sample matrix in the as-built and homogenized state, all with ± 1.0 at.% uncertainty, together with corresponding electronic concentration, e/a. OB as-built data are from a comparable sample.

at.%	Ni	Mn	Co	Sn	e/a
PB	44.5	36.4	6.6	12.5	8.09
$\mathrm{PB_{hom}}$	46.0	36.6	7.4	10.0	8.23
OB	43.0	37.8	6.5	12.7	8.04
$\mathrm{OB_{hom}}$	45.2	36.8	7.5	10.5	8.19
Nominal	43.0	39.0	7.0	11.0	8.10

compositions for each sample are given in Table 5.2 and compared with homogenized composition data. Ni concentration increased in the as-built matrix from the nominal and increased further after homogenization. From the nominal composition, there was a decrease in Mn by 2-3 at.% in the as-built sample matrix, which was not recovered after homogenization. There was also a slight decrease in Co in the as-built sample matrix, but this was recovered and surpassed the nominal composition of 7 at.% in the homogenized samples. Conversely, there was an increase in Sn in the as-built matrix, which dissipated and reached a level about 1 at.% lower than nominal after homogenization.

With compositions so varied, XRD was necessary to determine the phases present; all patterns are shown in Figure 5.5. The XRD patterns for the as-printed OB sample were indexed as a mixture between a cubic disordered structure (Pm3m space group) and a low symmetry 7M monoclinic martensitic phase, with homogenization leading to the appearance of an $L2_1$ ordered $Fm\bar{3}m$ phase (Table 5.3). Similarly, the PB sample began in the as-printed condition with a 7M martensitic phase, but was progressively replaced by the ordered cubic $L2_1$ phase, which remained after homogenization. For the PB sample, there was also an unidentified peak near 39° that was reduced by heat treatment.

In as-deposited samples, EDS analysis showed that sub-grain boundaries (interdendritic regions) were significantly depleted in Sn, while dendrite cores (composition given in Table

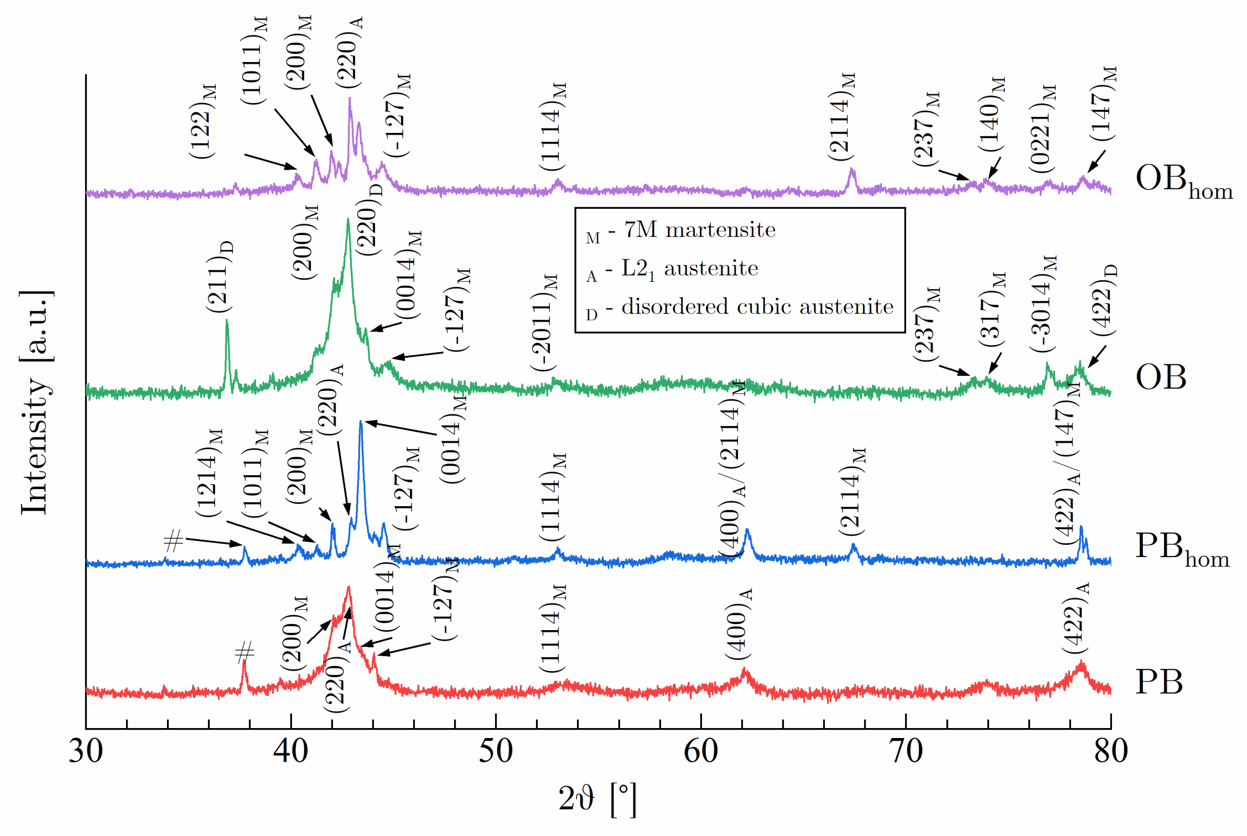

Figure 5.5: Room-temperature XRD patterns showing L2$_1$ austenitic, disordered cubic austenitic, and martensitic peaks. # marks an unidentified peak that does not correspond to austenitic, martensitic, or face-centered cubic (FCC)-γ phases.

Table 5.3: Phases and lattice parameters determined using XRD patterns.

Sample	Phase	a(Å)	b(Å)	c(Å)	β(deg)
PB	$L2_1$ ($Fm\bar{3}m$)	5.98			
	Monoclinic 7M	4.30	5.36	29.22	93.50
PB_{hom}	$L2_1$ ($Fm\bar{3}m$)	5.97			
	Monoclinic 7M	4.32	5.38	29.31	94.47
OB	Disordered (Pm3m)	5.96			
	Monoclinic 7M	4.29	5.34	29.11	94.37
PB_{hom}	$L2_1$ ($Fm\bar{3}m$)	5.96			
	Monoclinic 7M	4.31	5.38	29.31	94.49

5.2) were slightly Sn-enriched. Sn segregation is a well-known occurrence in casting of other alloys such as Cu-Ni-Sn due to the low melting point of Sn [218], thus it is not unexpected that fast and repeated thermal fluctuations experienced by the material in DLD also produce Sn segregation [219]. Twinning presence varied throughout the segregated regions, indicating a difference in the phases present. This is supported by DSC data in Figure 5.6a, where the transformation peaks are significantly broadened. The broad peak is a combination of many small peaks at slightly different peak locations that correspond to the different compositions present on the micro-scale within these samples. Indeed, even small compositional changes are known to have a large effect on the martensitic transition (MT) temperature of Ni-Mn-based functional magnetic materials [64, 66]. After homogenization however, this microsegregation was mitigated, as evidenced by the much narrower transformation peaks seen in Figure 5.6b and by EDS data.

Composition compared between the nominal, as-built matrix, and homogenized states shows how the elements are lost and redistribute within the material. From the nominal composition of $Ni_{43}Co_7Mn_{39}Sn_{11}$, there was a loss of Mn in the as-built state that was not recovered in the homogenized state. Since Mn has a low vapor pressure, it has been shown that a small amount is lost during full melting with the laser during the deposition

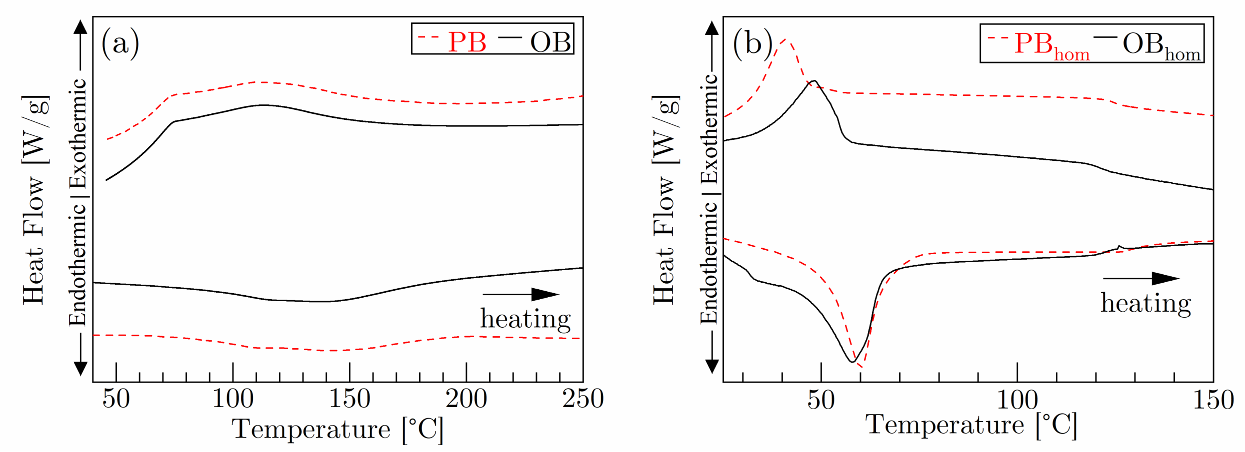

Figure 5.6: DSC thermal analysis, showing that as-printed samples (a) exhibited a very broad peak, whereas heat-treated samples (b) had sharper peaks and a distinct T_C.

process [181, 182]. There is slightly greater loss of Mn in the PB sample, which may be due to the increased energy density present in the process. Although the laser power and scan speed were held constant, there would have been a higher energy density in the smaller sample (PB) because there was less influx of material.

XRD patterns show that the as-built samples did contain 7M martensite, and either an ordered or disordered cubic phase. The reduction of the $(220)_A$ peak intensity of the austenitic phase indicates that the heat treatment promotes the growth of the martensitic phase. Moreover, the sharp drop of the $(211)_A$ peak intensity in the OB sample can be associated with an atomic rearrangement of the cubic phase (cubic disordered to $L2_1$ ordered). The PB sample contained $L2_1$ rather than the cubic disordered phase, which is likely a result of the differences in composition and composition distribution between the OB and PB samples. The PB sample also showed an unidentified peak that did not match with the cubic disordered, $L2_1$, or 7M phases, and also did not correspond to the FCC-γ phase that has been seen for this composition type [220–222].

Table 5.4: Transformation temperatures (M_s, M_f, T_M, A_s, A_f, TA and T_C) and room-temperature magnetization values at 2 T applied magnetic field for homogenized samples. ± values represent uncertainly related to the tangent method measurement of the transformation temperatures.

	M_s [°C]	M_f [°C]	T_M [°C]	A_s [°C]	A_f [°C]	T_A [°C]	T_C [°C]	M_{2T} $[Am^2/kg]$
$\mathrm{PB_{hom}}$	47 ± 1	32 ± 1	39.5 ± 2	52 ± 1	67 ± 1	59.5 ± 2	125 ± 3	14.7
$\mathrm{OB_{hom}}$	57 ± 1	36 ± 1	46.5 ± 2	49 ± 1	66 ± 1	57.5 ± 2	121 ± 3	19.4

5.1.2.3 Martensitic Transformation As-built samples showed very broad transformation peaks on DSC curves, plotted in Figure 5.6a. Though distinct MT temperatures are difficult to extract, the reverse martensitic transformation (martensite to austenite) occurred over a range of approximately 90-170 °C and the forward transformation (austenite to martensite) occurred over a range of 60-140 °C. Both the PB and OB as-built DSC curves have the same shape and do not show a distinct Curie temperature ($\mathrm{T_C}$).

After homogenization (Figure 5.6b), as expected with the elimination of microsegregation, the MT peaks were more distinct, and the range of transformation decreased significantly. Using the tangent method, martensite and austenite start and finish transformation temperatures (M_s, M_f, A_s, and A_f) were determined and are shown in Table 5.4, along with $T_M = (M_s + M_f)/2$ and $T_A = (A_s + A_f)/2$. T_C was very close in both samples.

Cong et al. reported the austenitic peak of induction melted, annealed $\mathrm{Ni_{43}Co_7Mn_{39}Sn_{11}}$ to be about 57 °C and the martensitic peak to be about 34 °C [223]. Observed here for $\mathrm{PB_{hom}}$ and $\mathrm{OB_{hom}}$ were $T_A = 59.5\,^{\circ}\mathrm{C}$ and $57.5\,^{\circ}\mathrm{C}$; $T_M = 39.5\,^{\circ}\mathrm{C}$ and $46.5\,^{\circ}\mathrm{C}$. Though the austenitic peak data tends to agree, the martensitic peak for the current samples is $5.5 - 12.5\,^{\circ}\mathrm{C}$ higher. This discrepancy is attributed to slight differences in composition of the samples from the nominal, giving rise to a difference in e/a from the nominal 8.10 to 8.23 in $\mathrm{PB_{hom}}$ and 8.19 in $\mathrm{OB_{hom}}$, respectively. Due to similar reasons, there is also a 7 °C increase in T_M from the $\mathrm{PB_{hom}}$ to $\mathrm{OB_{hom}}$ sample.

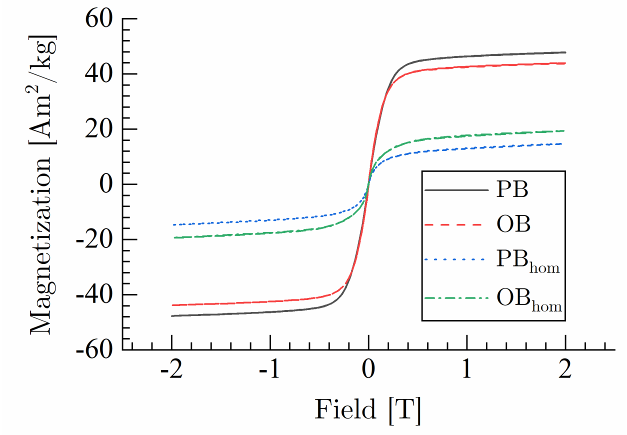

Figure 5.7: $M-H$ plot showing a drop in magnetization from the as-built to the homogenized samples measured at room temperature.

5.1.2.4 Magnetization Behavior Figure 5.7 shows the room-temperature magnetization curves for each sample and for their homogenized counterparts. At 2 T, PB and OB samples reached 47.8 A·m^2/kg and 43.9 A·m^2/kg, respectively. Homogenized PB and OB samples at 2 T reached 14.7 and 19.4 A·m^2/kg, respectively. Heat treatment therefore led to a drop of 33.1 A·m^2/kg (69.2%) in PB and 24.5 A·m^2/kg (55.8%) in OB. This is due to the increase in the volume fraction of martensitic phase within the samples (see Figure 5.5), since the weakly magnetic martensite phase does not react as strongly to an applied field as the ferromagnetic austenite phase does [224].

5.1.3 Summary

In this first study of direct laser deposition (DLD) additive manufactured magnetocaloric effect (MCE) material, we have demonstrated that deposition was successful and resulted in structurally intact samples. Structural and functional differences between an overbuilt and properly-built part, both as-built and homogenized were examined. Particularly, prior to homogenization, as-built sample structure showed dendrites, columnar grains in the overbuilt area, elongated cells in the properly-built area, and a mix of cubic austenite and 7M martensite. After homogenization, sample structure showed equiaxed grains in the properly-built area, persisting columnar grains in the overbuilt area, and a decrease in the austenite fraction in favor of the 7M martensitic phase. The latter effect was explained by some loss of Mn. The characteristics of the martensitic transformation and magnetism of the additively manufactured Ni-Mn-Co-Sn samples are comparable to those observed in the similar MCE alloy produced by conventional methods.

The DLD additive manufacturing processing of Ni-Mn-based MCE materials is a very promising technology, as it has demonstrated effective reproduction of typical MCE materials transformation and magnetic properties. If DLD is pursued as a fabrication method, powder flow control would need to be addressed to correct the inconsistent overbuilding. It is likely that using spherical powder of 44 to 150 µm, as recommended for DLD, would improve the consistency of the powder flowrate. Further progress is therefore expected after preparation of spherical MCE material powder with an atomization process. Improvements are also expected from the use of an additive manufacturing technique with a wider range of acceptable powder morphologies (non-powder feeder, powder bed methods) as presented in the following, Section 5.2.

5.2 BJ3DP Fabrication

5.2.1 Overview

A summary of current efforts in BJ3DP fabrication of Ni-Mn-Cu-Ga is given in Figure 5.8. Coupons of composition $Ni_{49.5}Mn_{19.1}Cu_{6.6}Ga_{24.8}$ at.% were additively manufactured using the powder bed binder jetting (BJ3DP) printing method. Coupons were then sintered at temperature intervals through melting to determine optimal sintering temperatures for properties and structural integrity. It was determined that 1080 °C was the closest solid-state sintering temperature before melting occured at 1090 °C. The sample sintered at 1080 °C was thoroughly characterized for magnetic and thermal properties, and was found to have favorable magnetocaloric properties.

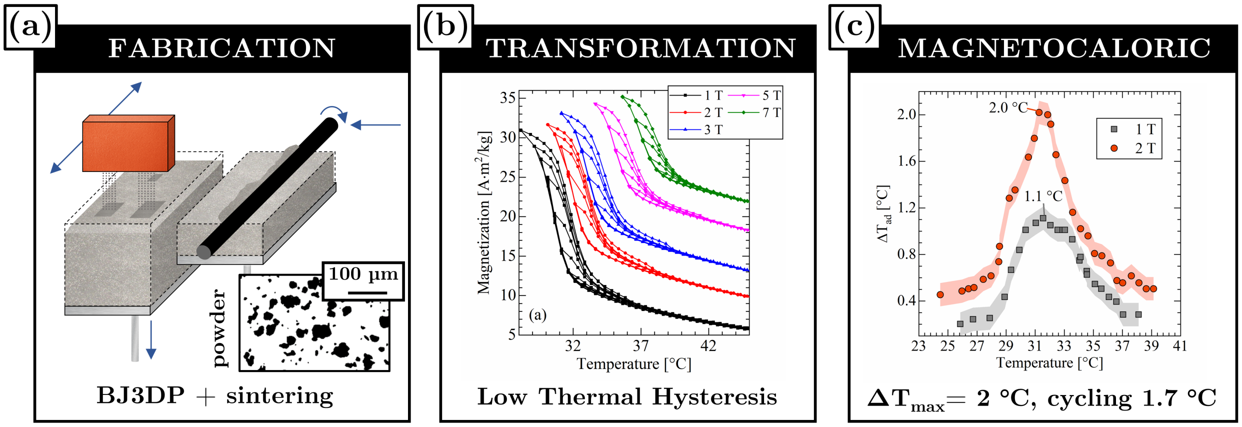

Figure 5.8: Overview BJ3DP printed Ni-Mn-Cu-Ga experiment: (a) fabrication by BJ3DP and post-print sintering, (b) low hysteresis values measured for partial transformation $M(T)$ loops, (c) good MCE evaluated by direct measurements and stable cycling values.

5.2.2 Results

5.2.2.1 Microstructure The results of density analysis are shown in Table 5.5. It is worth noting that the evaluation region for each technique was different. Archimedes' method was used to measure the bulk density (94% ± 1 pp [percentage points]). Micro-computed X-ray tomography (µCT) is only successful on small samples, so a sliver was cut from near the center of the workpiece (96% ± 1 pp). The image analysis was performed on micrographs from the sample after it was cut in a half near the center, so is more representative of a central plane (92% ± 1 pp). For Archimedes and µCT results, the error is directly related to the measurements, while for image analysis it is the standard deviation from 4 images. The backscattered electron micrographs in Figure 5.9 show that the pore distribution is unremarkable for a part sintered from powder. Pores are located along grain boundaries and are generally larger near the edges of the part.

As anticipated for BJ3DP with subsequent sintering at a sub-solidus temperature (no melting was involved), a homogeneous microstructure regarding the grain size and dominant phase, as well as the equilibrium shape of grains are evident in Figure 5.9. Grain size was

Table 5.5: Densities of BJ3DP sample measured using Archimedes, µCT, and imaging methods. Error for Archimedes and µCT is measurement-related, and for OM image analysis it is a standard deviation. Measured area or volume is also listed.

	Archimedes	**µCT**	**Imaging**
Density	94%	96%	92%
Error	± 1 pp	± 1 pp	± 1 pp
Measured	Bulk	Central Sliver	Center

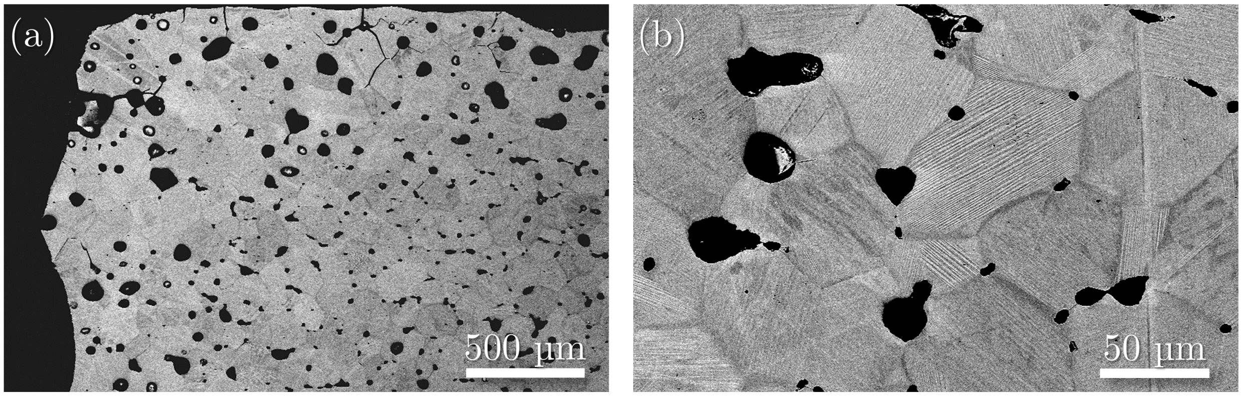

Figure 5.9: Backscattered electron micrographs of a polished cross section of the BJ3DP part. (a) An overview of a corner of the part; and (b) a magnified view of the pores along grain boundaries and grains exhibiting twinned martensitic phase.

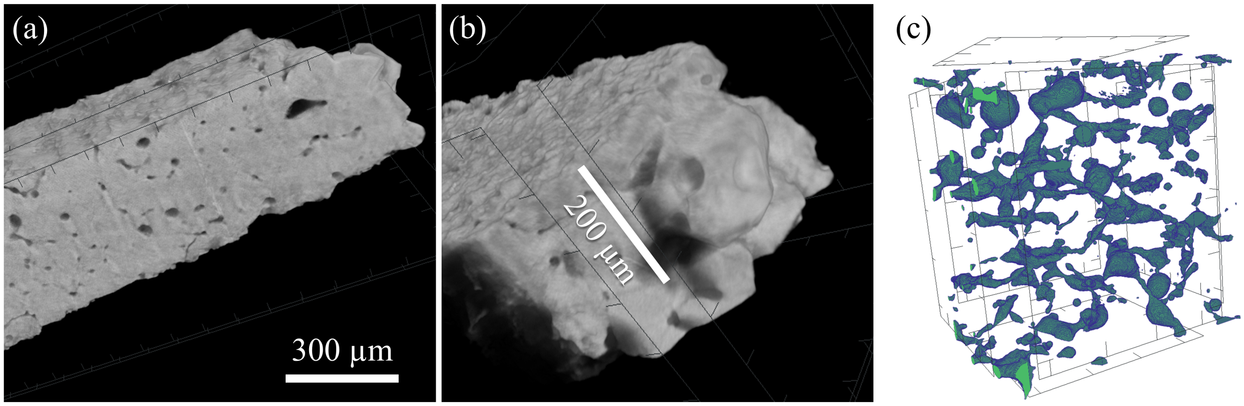

Figure 5.10: 3D visualizations using µCT data. (a) The view of a cut side of the slice, (b) a single grain on the top of the slice, and (c) porosity only, visualized for a small volume.

measured from 82 grains in optical micrographs to be 130 ± 30 µm in circle-equivalent diameters, slightly larger than the feedstock powder due to coarsening during sintering. Figure 5.9 also shows that grains contain twinning, indicating a dominant presence of the martensite phase at room temperature.

µCT-collected radiographs and subsequently reconstructed 2D slices were used to generate both porosity data and 3D visualizations. Figure 5.10 corroborates 2D porosity and grain information. Particularly, Figure 5.10b shows a single grain with porosity along the grain boundary. Figure 5.10c also confirms the existence of both standalone spherical pores and connected porosity, signifying that sintering progressed to the intermediate stage [105, 225]. In a µCT-reconstructed analyzed volume of 0.3 mm^3, the part had an average structure separation of 22 ± 12 µm, and an average structure thickness of 92 ± 24 µm. Within the same volume, pores had a median sphericity of 0.78, with 66% of pores having sphericity > 0.7 and 45% of pores having a sphericity > 0.8.

5.2.2.2 Martensitic Transformation and Crystal Structure Figure 5.11 displays DSC curves, where the reverse and forward MTs on heating and cooling are accompanied by sharp endothermic and exothermic peaks, respectively. DSC scans were measured up to

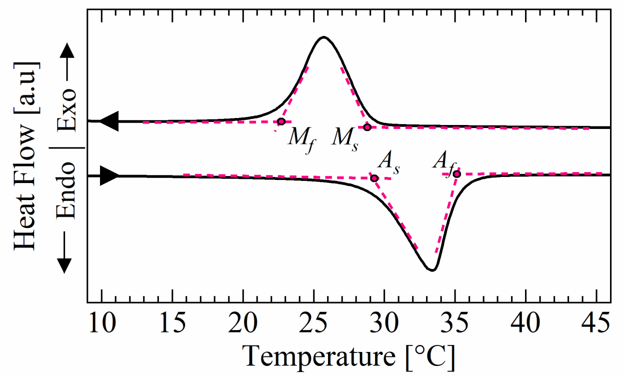

Figure 5.11: Calorimetric curves showing the reverse and forward martensitic transformation during heating and cooling, respectively. Two-tangent method intersection points are drawn to indicate the locations of martensite start (M_s), martensite finish (M_f), austenite start (A_s), and austenite finish (A_f) temperatures.

155 °C (not shown here) to confirm that no additional transformations occur in the material. The characteristic temperatures of MT, martensite start (M_s), martensite finish (M_f), austenite start (A_s), and austenite finish (A_f), have been estimated from DSC curves using the two-tangent intersection method, and they are summarized in Table 5.6. The MT temperatures of the forward and reverse transformations have been defined as $T_M = (M_s + M_f)/2$ and $T_A = (A_s + A_f)/2$, respectively, being $T_M = 299\,°\text{C}$ and $T_A = 306\,°\text{C}$. The MT hysteresis is equal to $\Delta T_h = T_A - T_M = 7\,°\text{C}$. For comparison, Table 5.6 also contains the MT data derived from the magnetization measurements discussed in Section 5.2.2.3.

The experimental and calculated XRD patterns are shown in Figure 5.12. At 300 K, they present a non-modulated tetragonal martensite (NM martensite) with the presence of some amount of the residual austenite. Table 5.7 summarizes the unit cell parameters determined for the martensitic and austenitic phases.

The values of parameters in Table 5.7 are in good agreement with the literature. Li et al. reported the L2$_1$ phase in $Ni_{44}Cu_6Mn_{31}Ga_{19}$ to have $a_0 = 5.865$ Å [92], larger than the values reported here due to the higher amount of Mn, which has the largest atomic radius of the contained non-doping elements. Sarkar et al. reported lattice parameters of the L2$_1$ phase in

Table 5.6: Characteristic temperatures of MT determined from DSC scans and from thermomagnetization curves measured under different magnetic fields.

	Field [T]	M_s [°C]	M_f [°C]	T_M [°C]	A_s [°C]	A_f [°C]	T_A [°C]
DSC	0	29	23	26	29	35	32
SQUID	0.01	29	25	27	30	34	32
	0.1	30	28	29	32	35	33
	1.0	31	29	30	33	36	35
	3.0	34	32	33	36	38	37
	7.0	38	36	37	39	42	41

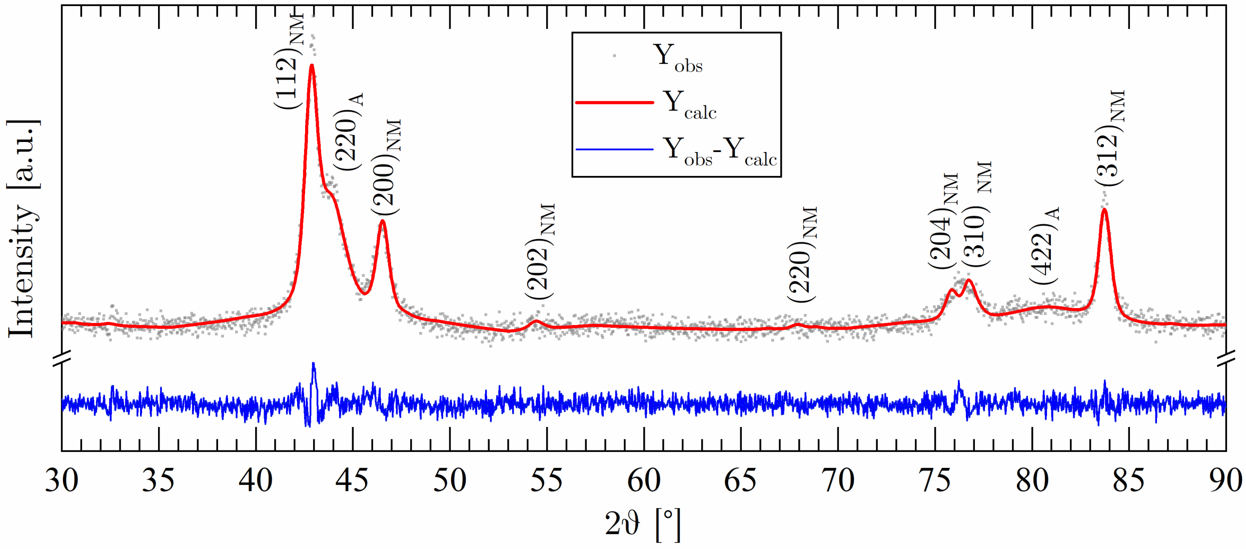

Figure 5.12: Experimental (Y_{obs}) and calculated (Y_{calc}) XRD patterns representing the 2-phase state at T = 27 °C. Indexing is according to the non-modulated tetragonal structure of martensite, NM (I4/mmm) and cubic L2$_1$-ordered austenite, A (Fm$\bar{3}$m).

Table 5.7: Unit cell parameters determined for non-modulated tetragonal martensite (space group I4/mmm) and austenite (space group Fm$\bar{3}$m)

	Martensite	Austenite
Lattice parameters	NM tetragonal	L2_1 cubic
a [Å]	3.903	a_0=5.830
c [Å]	6.547	

$Ni_{50}Cu_{6.5}Mn_{18.5}Ga_{25}$ to have $a_0 = 5.802$ Å and the I4/mmm NM phase for $Ni_{50}Cu_7Mn_{18}Ga_{25}$ to have $a = 3.893$ Å and $c = 6.436$ Å [91], and again a difference in Mn concentration could cause this mismatch. The nearest composition of $Ni_{50}Cu_{6.25}Mn_{18.75}Ga_{25}$ was reported by Roy et al. to have an L2_1 lattice parameter of $a_0 = 5.814$ Å [226].

5.2.2.3 Magnetization Behavior The results of thermomagnetization measurements performed at constant magnetic fields are depicted in Figure 5.13a. They show only one hysteretic anomaly, which means that the ferromagnetic order appears when the forward MT proceeds. The obtained $M(T)$ loops in Figure 5.13a were collected between full martensitic phase (low temperature) and full austenitic phase (high temperature). During the heating process there is a large drop in magnetization corresponding to the reverse MT from a ferromagnetic martensitic to a paramagnetic austenitic phase. The transformation is fully reversible during cooling - heating cycles. Under the influence of a magnetic field, the MT shifts to higher temperatures due to the stabilization of the ferromagnetic martensitic phase. Table 5.6 collects the MT characteristic temperatures obtained by the two-tangent method using data from Figure 5.13a.

The MT temperatures are plotted in Figure 5.13b as a function of the magnetic field, thereby representing a $\mu_0 H - T$ phase diagram, approximated by linear dependencies with almost the same slope, equal to $dT_M/d\mu_0 H = 1.2 \pm 0.1\,°\mathrm{C}/T$. The shaded area in 5.13b corresponds to the quasi-stable presence of martensitic or austenitic phase within a hysteresis loop, depending on whether heating or cooling is performed, respectively.

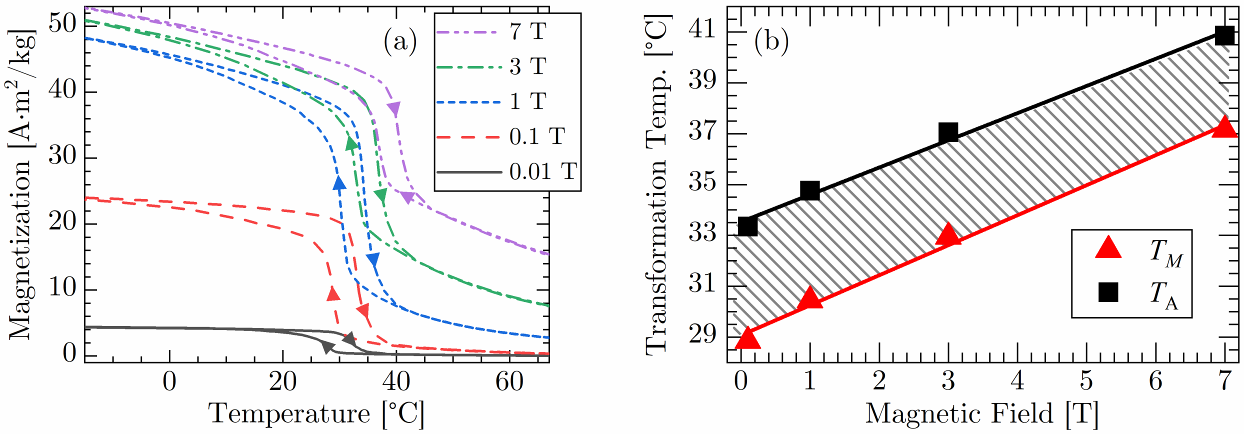

Figure 5.13: (a) Magnetization versus temperature dependencies during cooling-heating ramps in various magnetic fields. (b) $\mu_0 H - T$ phase diagram of the magnetostructural transformation, showing MT hysteresis to be almost independent of the magnetic field. Shaded region represents quasi-stable martensite or austenite upon either cooling or heating.

In the present work, it was found that a drastic decrease of the MT hysteresis can be achieved by partial cycling through the thermally- or magnetic field-induced MT, where only some fraction of material is reversibly transforming. Figure 5.14 shows the measured partial (or minor) $M(T)$ hysteresis loops which exhibit a thermal hysteresis equal to $1.2 \pm 0.1\,°\mathrm{C}$ for the largest minor loop at all applied fields (the value of hysteresis was taken as a temperature difference of averaged transformation temperatures found using the two-tangent method for the forward and reverse MT). This incredibly low value for the minor loop hysteresis is relevant for obtaining a large value of ΔM and a relatively narrow MT interval during partial cycling. The behavior of the last two parameters can be appreciated from Figure 5.14a and for the sake of comparison with the complete MT cycles in Figure 5.14b. Magnet designs for magnetic refrigeration reach magnetic field values of not more than 2 T [44, 227], and so detailed $M(H)$ measurements were carried out up to 2 T only.

Isothermal $M(H)$ curves measured in the vicinity of MT in the steps of $0.5\,°\mathrm{C}$ are plotted in Figure 5.15a. Before each measurement, the sample was heated to austenite and

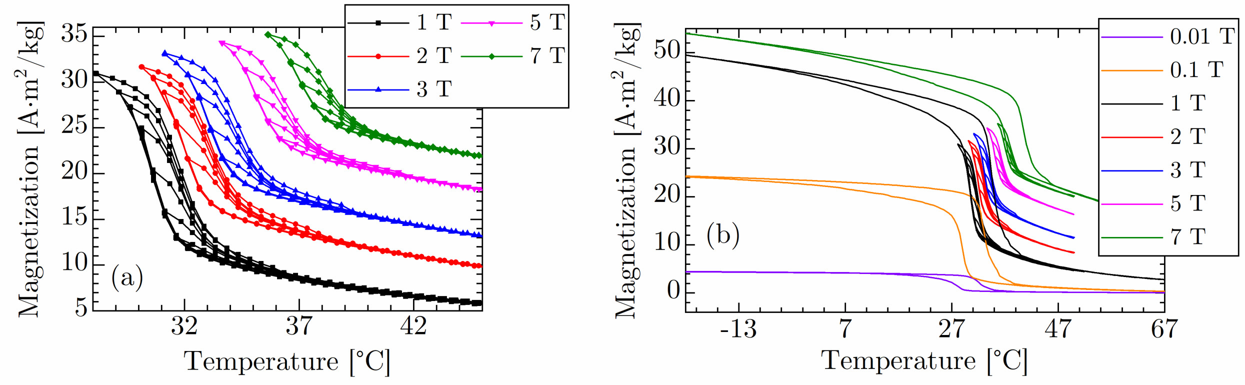

Figure 5.14: (a) Thermomagnetization curves at different magnetic fields recorded during cycling across thermally induced partial MT; (b) overlapping of several graphs from Figure 5.13a with the partial $M(T)$ cycling depicted in (a) to highlight a drastic reduction of the thermal hysteresis while maintaining large values of magnetization drops.

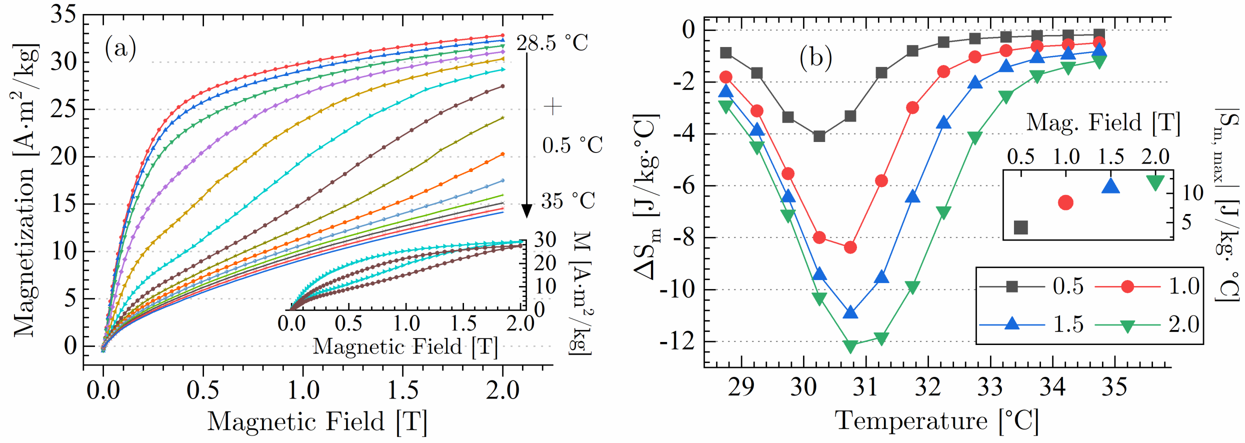

Figure 5.15: (a) Isothermal $M(H)$ curves, taken at 0.5 °C increments from 28.5 °C to 35 °C. Inset shows an exemplary full loop reversal behavior for 31 °C (light blue) and 31.5 °C (brown). (b) Temperature dependencies of the magnetic field induced entropy change, ΔS_m, at different constant magnetic fields in the range from 0.5 T to 2.0 T, calculated using isothermal magnetization data in (a). Inset demonstrates evolution of $\Delta S_{m,max}(H)$.

returned to the measuring temperature in order to avoid any influence of the partial transformation induced by the magnetic field. For the sake of clarity, only the curves recorded during increasing of magnetic field are displayed in Figure 5.15a. To demonstrate magnetic field-induced reversibility of MT however, two complete $M(H)$ loops are shown in the inset, as an example. At low temperature (28.5 °C), the martensitic phase shows a regular ferromagnetic behavior, although it is not saturated even at 2 T. At high temperature (35 °C) the magnetization is strongly reduced. It exhibits a nonlinear dependence due to the presence of two phases at this temperature: the ferromagnetic martensitic phase and paramagnetic austenite with a domination of the latter phase. For the intermediate temperatures, the non-regular change of the susceptibility is related to the magnetic field induced partial MT.

5.2.2.4 Adiabatic Magnetocaloric Response The conventional MCE, which should occur in the studied alloy at its magnetostructural transformation, was characterized by the indirect (evaluation of ΔS_m) and the direct (measurements of ΔT_{ad}) methods. The $\Delta S_m(T)$ dependencies were calculated from the isothermal $M(H)$ curves in Figure 5.15a using the Maxwell relationship, Equation 2.3, and the results are given in Figure 5.15b for different applied magnetic field changes. All the curves present a high and narrow minimum, resulting from the field-induced change of magnetic order. This change is related to the partial or full occurrence of the forward MT from the low-magnetization paramagnetic austenitic phase to the high magnetization ferromagnetic martensitic one. The maximum value of $|\Delta S_{m,2T}|$ is equal to ≈ 12.0 J/(kg · °C).

The adiabatic MCE response was measured during cooling upon sample insertion into the magnetic fields of 1 T and 2 T in adiabatic conditions. The same procedure was followed as in the case of isothermal $M(H)$ measurements, i.e., before each temperature test the sample was heated to full austenite and then the temperature was slowly reduced to the target temperature. The results are depicted in Figure 5.16. The maximum temperature change, $\Delta T_{ad} = 2.0 \pm 0.1$ °C, at 2 T, was obtained at TM around 31 °C, in accordance with Table 5.2.2.2. The peak on the curve $\Delta T_{ad}(T)$ spans approximately 10 °C. For lower applied magnetic fields, the ΔT_{ad} is reduced; a 50% reduction of the applied field results in a corresponding decrease in MCE response to ≈ 1 °C.

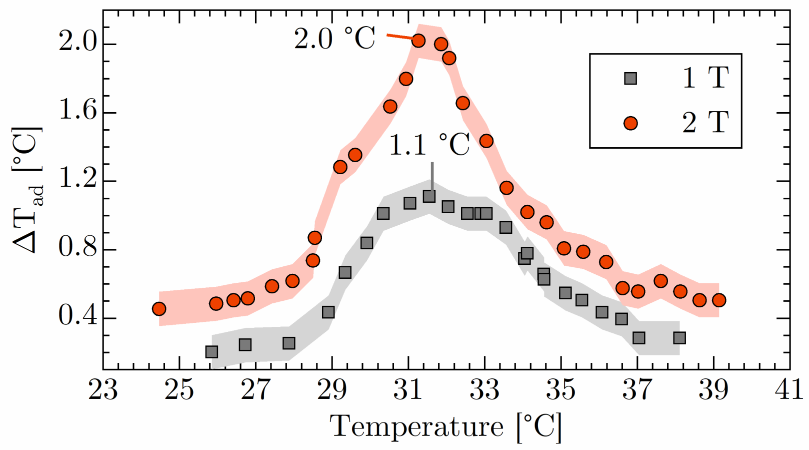

Figure 5.16: Magnetic field induced adiabatic temperature change at 1 T and 2 T measured at different temperatures on cooling. Shaded bands indicate a ± 0.1 °C of uncertainty in the ΔT_{ad} measurements.

Cycling measurements of ΔT_{ad} were conducted at constant temperatures by inserting/removing the sample into/from the magnetic field of 2 T with a full cycle time of 10 s. Variations in the temperature baseline are due to the imperfect manual control of the temperature via air flow regulation, but slow varied fluctuations were limited to within 0.5 °C. Results of measurements close to T_M are shown in Figure 5.17. Figure 5.17a presents the entire 101 measured cycles at a nominal temperature of 31 °C. Figure 5.17b is a rescaled view of what a series of measurements looks like and is extracted directly from the data in Figure 5.17a. Shown in the box in Figure 5.17c, a single measurement consists of a cluster of the data points collected when the sample is in a 0 T magnetic field and when it heats up under 2 T. The difference between the lower- and higher-temperature clusters of data points is the measured ΔT_{ad}.

Figure 5.18 shows the stability of ΔT_{ad} during cycling, with measurements to the nearest 0.05 °C due to uncertainty created by clustering of points as seen in Figure 5.17c. At the temperature where ΔT_{max} was observed (31 °C), the sample was repeatedly inserted into and removed from the field. The first cycle showed the highest value of 1.95 °C, near that

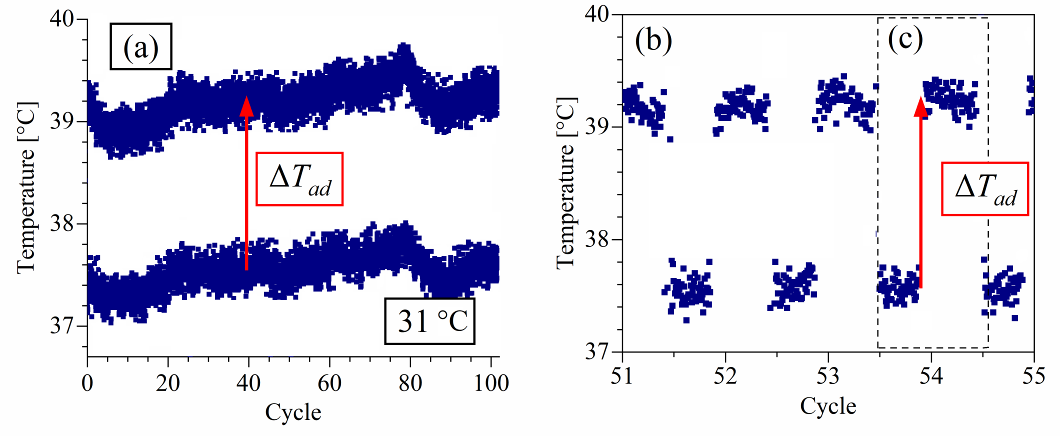

Figure 5.17: Adiabatic temperature change of the sample under the magnetic field on/off cycling conducted at 31 °C. (a) Results for 101 cycles. (b) Rescaled view of several measurement cycles showing the step-like change of the temperature of the sample induced by its periodic inserting/extracting into/from the magnetic field of an electromagnet. (c) A single measurement, indicating the value of ΔT_{ad}.

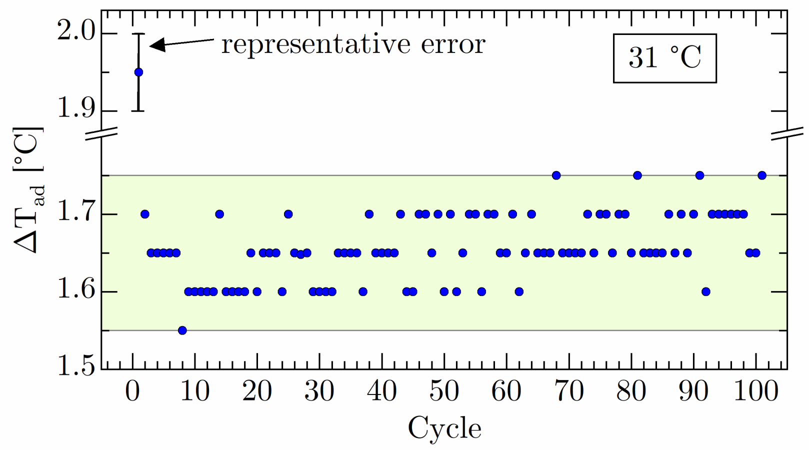

Figure 5.18: Magnetic field cycling performed at the temperature where ΔT_{max} was observed (31 °C). The first data point shows a representative ± 0.5 °C of uncertainty that is assumed to be valid for all other plotted points. The filled area indicates where 97.5% of all points and their error bars fall within, excluding the first data point.

Table 5.8: Heat treatment at temperature T_{an} during time t; martensitic start temperature (M_s); temperature hysteresis of MT (ΔT_h); unit cell volume of martensitic phase (V); and MCE characteristics ($|\Delta S_{m,max}|$, one-way ΔT_{ad}) obtained at T_{max} under applied magnetic field ($\mu_0 \Delta H_{app}$) for Ni-Mn(Cu)-Ga alloys exhibiting magnetostructural transformation.

	T_{an}	t	Cool	M_s	ΔT_h	V	$\mu_0 \Delta H_{app}$	T_{max}	$\Delta S_{m,max}$	$\Delta T_{ad,max}$	Ref.
Composition	[°C]	[h]		[°C]	[°C]	[Å^3]	[T]	[°C]	[J/kg $\cdot$ °C^{-1}]	[°C]	
$Ni_{49.5}Mn_{19.1}Cu_{6.6}Ga_{24.8}$	1080	2	air	29	7 (full)	99.80 (NM)	2	31	12.1	2.0	This
(BJ3DP)	(sinter)				1.2 (partial)	198.16 ($L2_1$)	2	31		1.7 (cycle)	work
$Ni_2Mn_{0.75}Cu_{0.25}Ga$	800	144	furnace	35			2	35	28		[88]
$Ni_{49.9}Mn_{19.1}Cu_{6.4}Ga_{24.6}$	850	24		16	10	195.31 ($L2_1$)	1	30	10.2		[91]
$Ni_{49.9}Mn_{19.6}Cu_{5.7}Ga_{24.8}$			furnace	17		96.64 (NM)	2	27	9.86	0.23	[228]
$Ni_2Mn_{0.75}Cu_{0.25}Ga$	800	144	furnace	35			2	30		1.5	[229]
$Ni_{49.3}Mn_{18.4}Cu_{7.6}Ga_{24.7}$	900	24		43	11		1.5	48	12.8	1.6	[230]
$Ni_{50}Mn_{18}Cu_7Ga_{25}$	900	24	air	41	9		2	49	14.3		[118]

observed in the initial direct MCE response test. Past the first point, ΔT_{ad} dropped to approximately 1.65 °C, with 97.5% of the 100 cycles and their ± 0.5 °C error bars falling within 1.55 − 1.75 °C. The appearance of a slight trend upwards is an effect of the slight upward trend in manually controlled temperature, which can be seen in Figure 5.17a.

5.2.3 Discussion

5.2.3.1 Analysis of Transformation Characteristics Table 5.8 compiles the data obtained in the present work and compared to literature for similar FSMAs. Table 5.8 shows the slight increased value of the unit cell volume of martensitic phase calculated for BJ3DP sample, 99.73 Å^3, compared to that calculated using data presented by Sarkar et al. [44], 97.54 Å^3, or from Wroblewski et al. [228], 96.64 Å^3. These variations can be related to the differences in the composition. Also, an influence of the possible antisite atomic disorder and/or interstitial positions of some atoms (possibly carbon) could not be discarded.

A minimized temperature hysteresis of the magnetostructural transformation is necessary for the long-life cycling stability of MCE material. Table 5.8 shows that, whereas the characteristic transformation temperatures of the BJ3DP alloy and materials prepared by conventional methods all have T_{max} close to room temperature, the thermal hysteresis of the complete MT, ΔT_h, appears reduced, from the lowest literature values $9-11\,°\mathrm{C}$ [91,118,230] to about $7\,°\mathrm{C}$ in the printed sample. Different rationales can justify this reduction. For instance, the porosity and large grain size may be factors favoring a low hysteresis. Studies on nonmagnetic Cu-based SMAs show that the hysteresis is reduced as the grain size grows, reaching a minimum for grain size higher than 100 µm [231]. In the present case, the high temperature sintering process increased the grain size in the BJ3DP sample from the initial size of the feedstock powder, which can result in the reduction of ΔT_h. Furthermore, the width of thermal hysteresis exhibited by the thermoelastic MT is directly proportional to the residual stress (low thermal hysteresis for low residual stress) [232]. Residual stresses are minimal in BJ3DP parts because the printing process does not introduce any sharp thermal gradients through heating-cooling cycles, as selective laser melting does [233]. All of these factors can contribute to a reduction of ΔT_h. Thus, the above discussion indicates that this BJ3DP fabrication process does not have a significant impact on composition, structure or characteristic temperatures, but reduces the width of the main hysteresis loop characterizing the complete MT.

Naturally, the hysteresis loop of the partial MT should be located inside of the main MT loop, whereby the further reduction of hysteresis width is expected. It is very hard to predict the width of partial hysteresis since the theoretical description must deal with the processes of the volume fraction evolution in the locally nonequilibrium two-phase states [234]. In our work, we found experimentally that the Ni-Mn-Ga based material exhibits a partial MT accompanied by a more than 5 times reduced hysteresis if compared to the complete MT, Figure 5.14b.

A reduction of MT hysteresis was also observed for Ni-Mn-In(-Co) metamagnetic shape memory alloy (MMSMA) when partial cycles were performed starting from the martensitic phase [78, 235]. While the hysteresis reduction in [78, 235] is much smaller than that observed here, this can be explained by the radically different interplay between mechanisms contributing to the energy barrier for phase transformation: phase stabilization with field applied, stress buildup at the habit plane and during reorientation of twin variants, formation of nucleation centers, and reduction of stress fields by way of open surfaces. In Ni-Mn-In(-Co)

MMSMA, the field-preferred phase is austenitic. Gottschall et al. point out that in partial cycles (minor loops) from low temperatures, energy is saved through preserving martensitic nucleation sites [78] and they additionally propose that there is a buildup of stresses as twin variants reorient in the two-phase region [235]. Both preservation of martensitic nucleation sites and stress buildup during twin variant reorientation shift MT to lower temperatures and encourage transition to the high-temperature austenitic phase. Alternatively, in the case of the studied printed and porous Ni-Mn(Cu)-Ga FSMA, the field-preferred phase is martensitic. Though stress fields form at the habit planes, stress relief and easy nucleation can occur at the porosity concentrated at grain boundaries. Therefore, although energy is required for the martensitic nucleation centers to form, it is clearly outweighed by the energy savings due to a preferred martensitic phase and porosity resulting in stress relief and easy nucleation sites. An appearance and relaxation of mechanical stresses during partial or complete MT can be monitored by the diffraction methods at large-scale facilities (e.g. [236, 237]).

5.2.3.2 Magnetocaloric Effect and Technological Issues The direct MCE measurements show T_{max} of 2.0 °C at 2 T for the first test, and a stable field- induced temperature change of approximately 1.65 °C for 100 cycles more (Figure 5.18). The first cycle normally results in a higher measured effect, but stable cycling response is expected to be reduced. The value of the decrease depends on the amount of residual phases during the partial martensitic transformation [238]. Following [78], the changes of magnetization caused by the complete and partial MT (see $M(T)$ curves in Figure 5.14b) were used for rough estimation of the volume fraction of the martensitic phase involved during sample cycling at 304 K under 2T, equal to about 70%. Comparing with the other polycrystalline samples shown in Table 5.8, similar MCE characteristics have been determined for similar compositions, but it is important to note that no cycling experiments were previously performed in order to determine the value of stabilized ΔT_{ad}.

Unlike past studies, this investigation used binder introduced during the 3D printing phase, cured in an oven, and mostly burned out during sintering. However, sintering is conducted in argon-purged vacuum and in an enclosed quartz tube, not allowing for burnout products to be carried away. To eliminate these products, the Ti sponge was also encapsulated in the tube as an oxygen getter. In addition to oxygen, the binder composition includes carbon, which cannot be as simply trapped by a getter. Carbon could be partially incorporated into a crystal lattice of FSMA as an interstitial, potentially causing some of the volumetric expansion observed over the data from Refs. [91, 228], as indicated in Table 5.8. Though inclusions are often considered detrimental for the functional properties, an intentional hydrogenation of magnetocaloric material La(Fe,Si)$_{13}$, for instance, allows for tuning of MCE without precluding stability [239]. Carbon could serve a similar tuning purpose in binder jet 3D printed magnetocaloric materials, expanding the ranges of acceptable compositions and opening a new avenue for fabrication. The role of carbon and its impacts requires further investigation.

In addition to the possible incorporation of carbon, the influence of pores and grain boundaries merits further study as well. It was found that along most of the grain boundaries several pores exist (Figures 5.9 and 5.10) as a result of incomplete densification. Some of the grain boundary pores have oxides of several microns diameter embedded, as previously shown in [187]. Small-scale (10 nm) matrix-dispersed Mn oxides have been identified in Ni-Mn-Ga thin films even after careful preparation and annealing in inert atmosphere [240–242]. Since surface and matrix-distributed Mn-O is unavoidable in these alloys, these are not expected to impact the comparison of MT values with other literature sources, which would experience the same. Mn-O particles found at the grain boundaries of the studied alloy in [187] may aid in inter-grain stress relief while not being detrimental to MT since they are not integrated into the matrix. For structural materials, porosity and grain boundary precipitates are detrimental, but in functional materials like Ni-Mn-Ga FSMAs, for which cyclic functionality depends upon both a reversible unit cell volume change and constraints at grain boundaries, porosity can be highly beneficial [243].

5.2.4 Summary

Additive manufacturing in the form of powder bed binder jet 3D printing is shown to be a viable method for producing magnetocaloric Ni-Mn(Cu)-Ga FSMAs. Post-processing included sintering in an argon-purged vacuum atmosphere followed by an air cool. Samples showed a ΔT_{ad} of 2 °C under 2 T at 31 °C. Subsequent cycling resulted in a stable ΔT_{ad} of approximately 1.65 °C. The stable cycling of such a value of ΔT_{ad} is achieved owing to an incredibly low hysteresis for FSMAs of 1.2 °C, accompanying a partial magnetostructural martensitic transformation, with still-high values of ΔM and a narrow transformation interval. The possible incorporation of carbon from the binder may cause observed volumetric expansion which might serve as additional factor improving functionality of printed material, but this requires more study. Pores at grain boundaries allow for better conditions for reversible volumetric expansion necessary for functionality. Powder bed binder jet printing is proved to be a successful processing route for magnetocaloric materials, such as Ni-Mn-Cu-Ga FSMA.

5.3 In-Situ Monitoring of BJ3DP Post-print Heat Treatments

5.3.1 Overview

A summary of binder jet 3D printing (BJ3DP) of Ni-Mn-Cu-Ga is given in Figure 5.19, and one related publication can be found at [188]. Neutron diffraction data was collected at the Helmholtz Zentrum in Berlin, Germany on samples of layered and single-material BJ3DP samples of Ni-Mn(-Cu)-Ga. E3 beamline data was collected to observe *in-situ* unit cell development during sintering and annealing of BJ3DP parts. Final, post-annealing parts were evaluated for composition, density, and thermal phase transformation behavior. This study presents new quantitative data describing the structure evolution during heat treatments after BJ3DP, and connects that evolution to the final obtained parts. In addition, this study uses the first multi-material layered BJ3DP parts, an important proof-of-concept display towards layered-property magnetocaloric heat exchangers fabricated by AM.

5.3.2 Results

Diffraction peaks were analyzed and compared for both the sintering and annealing processes, with each containing the *ramp up*, *hold*, and *cool down* segments. Complete time-

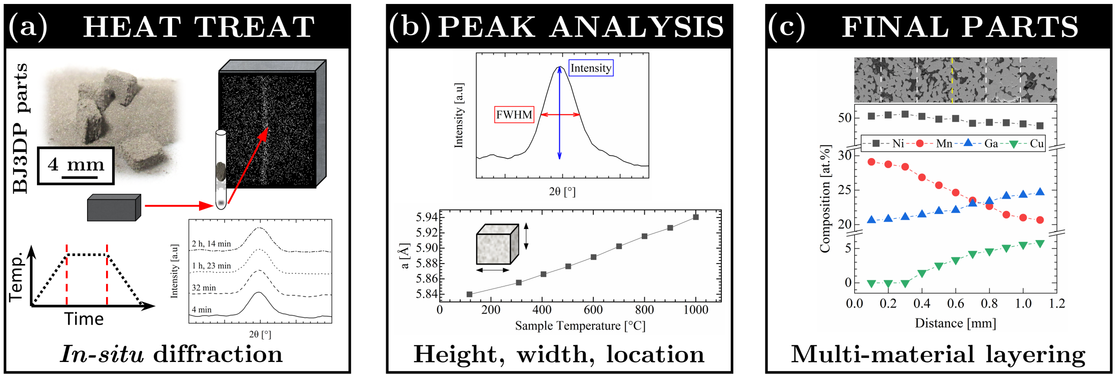

Figure 5.19: Overview of neutron diffraction for *in-situ* heat treatment of BJ3DP printed Ni-Mn(-Cu)-Ga parts. (a) Heat treatment sintering and annealing processes were carried out while collecting diffraction patterns. (b) Diffractograms were generated from area diffraction images and peak height, width, and location was analyzed. (c) Composition, structure, and transformation behavior of post-annealing parts was measured.

temperature-intensity and time-temperature-lattice parameter plots are provided in Figures A1-A4, but relevant projections of these are also presented directly in the following sections.

5.3.2.1 Sintering Process Area detector images were evaluated to assess the quality of the signal informing the quantitative peak analysis. During the ramp up stage of sintering, the NMG sample showed a faint, broad ring until 350 °C, then a more coherent ring forms at 457 °C. This peak formation and coalescence trend is shown in Figure 5.20 and persists across all samples with the formation temperature varying slightly based in large part on experimental factors: formation at 322 °C (mixed), 322 °C (layered), and 365 °C (NMG-Cu); coalescence at 426 °C (mixed), 431 °C (layered), and 475 °C (NMG-Cu).

Calculated lattice parameter a values and measured FWHM and intensity of fitted Gaussian peaks were compared across samples in Figure 5.21. After 475 °C, all samples showed an increase in lattice parameter (a decrease in 2θ peak location, as calculated from the Bragg condition in Equation 4.4). Throughout all segments, NMG had the highest (average) lattice parameter, NMG-Cu the lowest, with the mixed and layered samples falling in the middle

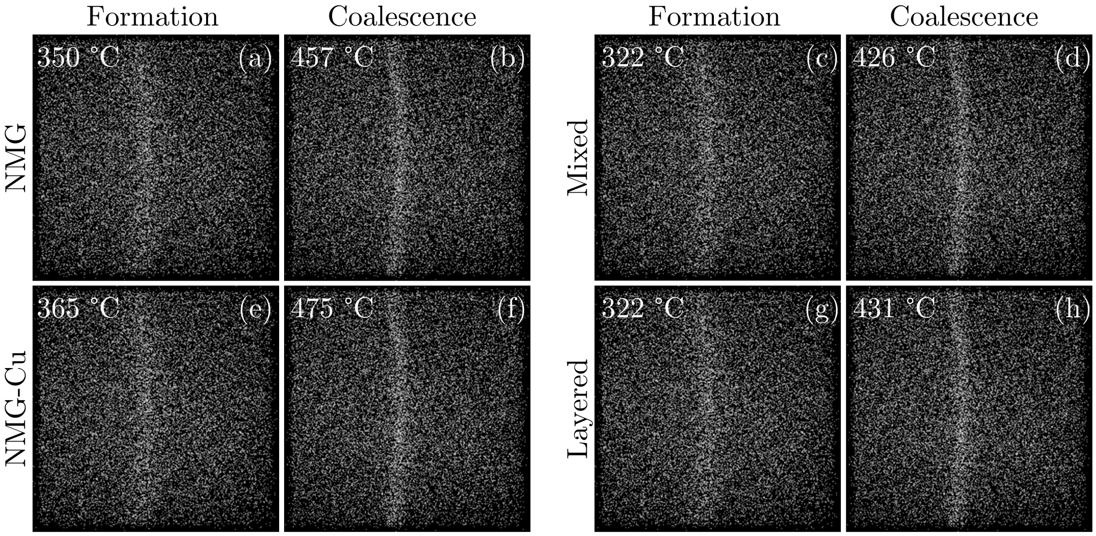

Figure 5.20: Peak formation and coalescence on sintering ramp up, with corresponding temperatures given.

with similar values. The NMG-Cu peaks were the broadest (highest FWHM). NMG, mixed, and layered samples had similar FWHM. Though intensity values cannot be compared across samples due to differing diffraction volumes, all peak intensity values trended upwards during initial ramp up then began to curve back down between 600 and 700 °C, .

After the sintering hold, a cool down was initiated, during which the single diffraction peak blurred and split in the 40-50 °C region for mixed and layered parts. NMG and NMG-Cu were monitored only through 150-200 °C. For the mixed-powder sample, the single peak split into 3 around the combined images 43-38 °C. Similarly, for the layered sample, the single peak gained two faint side peaks at 37 °C. Only the center peak is monitored, measured, and plotted in Figure 5.21.

5.3.2.2 Annealing Process Figure 5.22 presents the comparison of lattice parameter, intensity, and FWHM across ramp up, hold, and cool down segments for the annealing process. During the ramp up stage of annealing, there was a shift of each ring to lower 2θ (increased lattice parameter), accompanied with broadening for layered and NMG, with

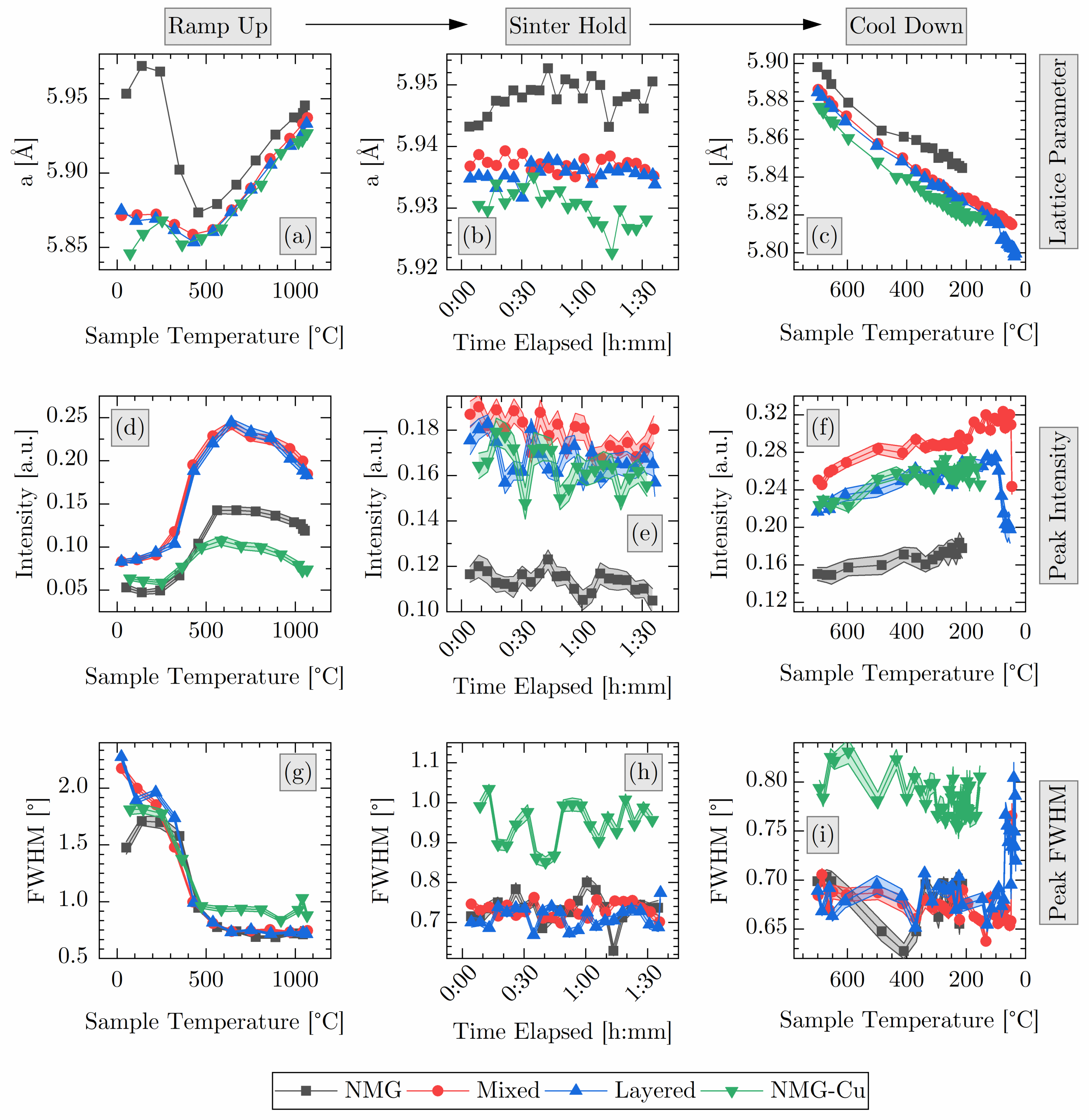

Figure 5.21: Evolution of lattice parameter (a-c), peak intensity (d-f), and peak FWHM (g-i) for the sintering process ramp up (a, d, g), hold (b, e, h), and cool down (c, f, i).

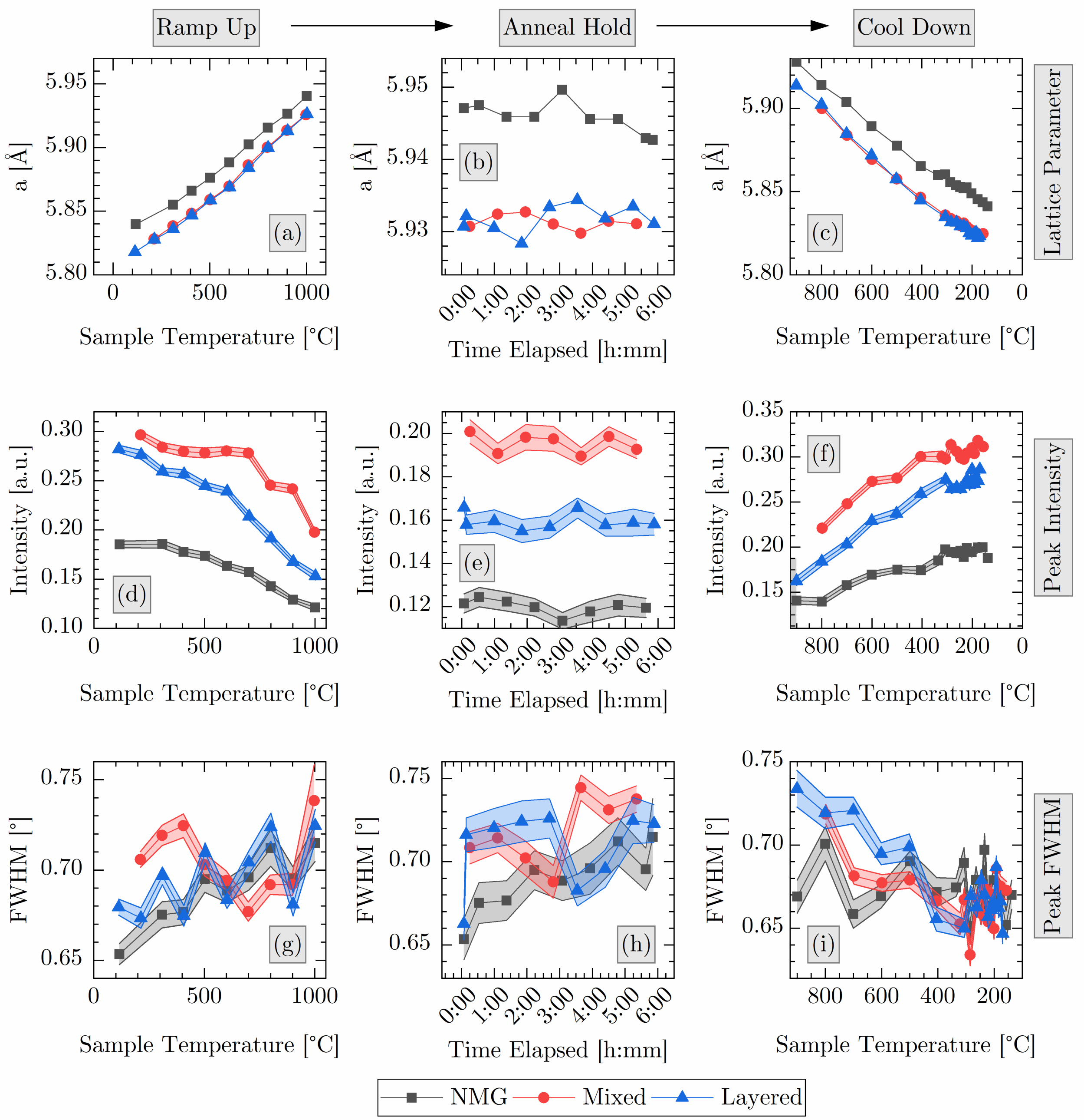

Figure 5.22: Evolution of lattice parameter (a-c), peak intensity (d-f), and peak FWHM (g-i) for the annealing process ramp up (a, d, g), hold (b, e, h), and cool down (c, f, i).

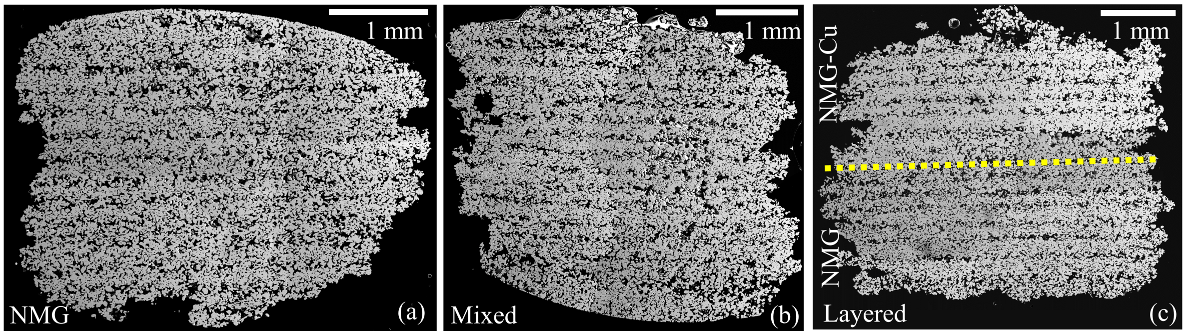

Figure 5.23: SE micrographs of cross-sections for (a) NMG, (b) mixed, and (c) layered parts.

mixed experiencing a modest FWHM decrease around 500 °C, but remaining around 0.7° 2θ width for the entire heating range. Amongst the samples, NMG maintained the highest lattice parameter, with the mixed-powder and layered parts' average a remaining similar. Considering fitting errors, all FWHM values were similar. All parts showed a decrease in peak intensity with increasing temperature and nearly constant peak intensity during the hold segment. During the annealing hold segment, lattice parameter trends persisted (NMG highest, mixed and layered similar) and FWHM of fitted peaks increased slightly during the hold but were similar to each other. Upon cool down after annealing treatment, peak intensity increased for all samples and lattice parameter decreased. FWHM showed a slight decrease on cool down for all samples.

5.3.2.3 Final Structure Overview SE micrographs in Figure 5.23 showed distinct layers with an intralayer increase in porosity. NMG and mixed samples showed a relatively consistent average porosity across the cross-section, with 68.1 ± 0.9% and 68.7 ± 2.1%, respectively. Density of the NMG-Cu and NMG halves of the layered sample were different, measured at 79.4 ± 2.3% and 73.1 ± 2.1%, respectively. The distinction between NMG and NMG-Cu layer sets is marked in Figure 5.23c.

As a reminder from Section 4.5, nominal composition for the two used powders were: $Ni_{49.7}Mn_{30.0}Ga_{20.3}$ and $Ni_{49.6}Mn_{19.2}Cu_{6.3}Ga_{24.9}$ at.%. Elemental analysis for the NMG part

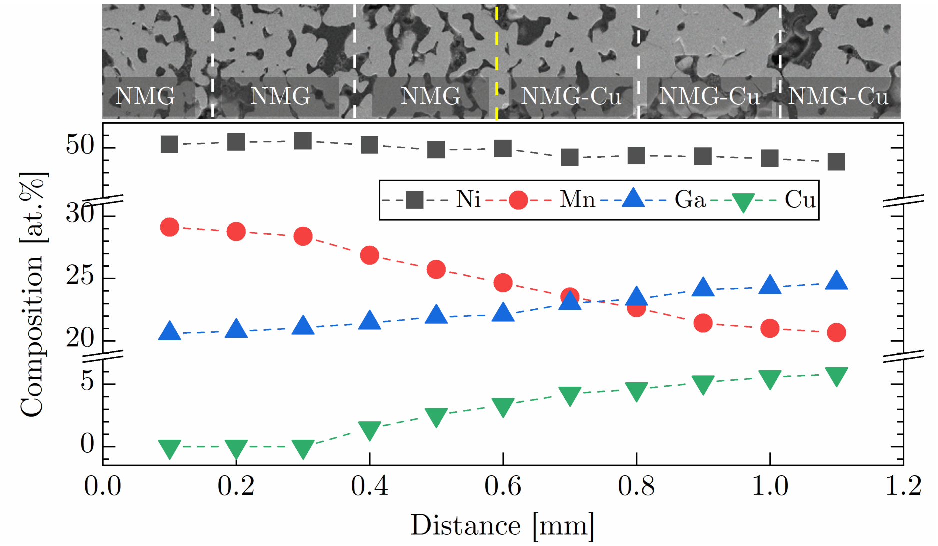

Figure 5.24: Compositional change across the boundary between NMG and NMG-Cu. Dashed lines indicate approximate layer boundaries. The yellow dashed line indicates the approximate boundary where powder composition was changed.

resulted in a composition of $Ni_{49.9}Mn_{29.8}Ga_{20.3}$ at.%, and the mixed-powder part in a composition of $Ni_{49.8}Mn_{23.5}Ga_{22.9}Cu_{3.8}$ at.%. All elements has ± 0.2-0.4 at.% standard deviation. Composition is plotted across the NMG and NMG-Cu boundary of the layered sample in Figure 5.24. In the 6 layers analyzed, Ni differed the least across the boundary (-1.4 at.% NMG → NMG-Cu), and Ga showed a 4.0 at.% increase from NMG to NMG-Cu layers. Mn and Cu migrated opposite of each other, with a -8.5 at.% change in Mn and 5.8 at.% increase in Cu for NMG → NMG-Cu.

Thermal behavior is given via DSC traces in Figure 5.25. The mixed sample exhibited an extremely broad transformation with a low peak, possibly two peaks around 65 and 90 °C. NMG transformation was a clear first-order peak near 90 °C with a thermal hysteresis of ∼5 °C and peak widths of around 10 °C. In contrast, the layered part shows three peaks, at 90-100 °C, 45-50 °C, and 25-35 °C, with the latter two overlapping.

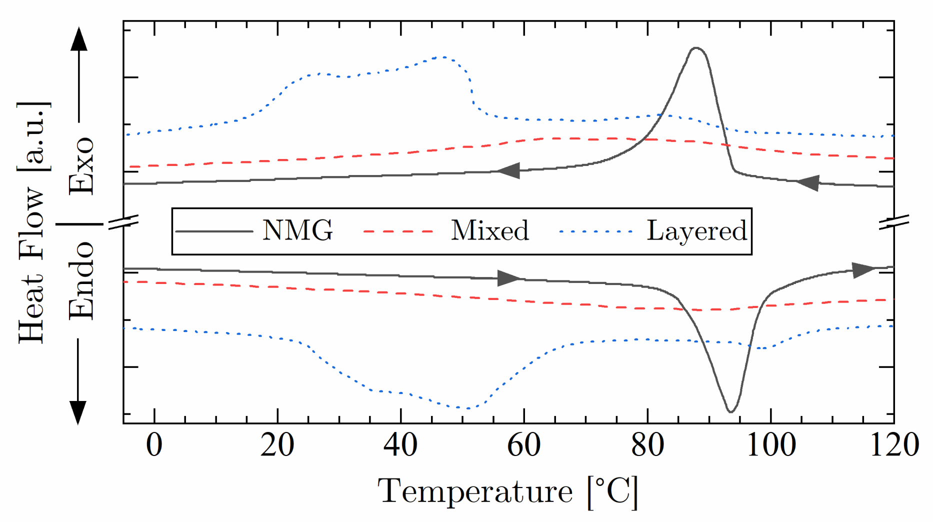

Figure 5.25: Thermal behavior of NMG, mixed, and layered parts.

5.3.3 Discussion

5.3.3.1 Structure Evolution It must first be emphasized that the significant jump in intensity between the ramp up and sintering hold segments (Figure 5.21d-e) for NMG-Cu can be fully attributed to experimental conditions. The sample slid partly out of the beam during testing, and was position-corrected for the hold segment, as described in Section 4.5.

Through all heat treatment stages, NMG had the highest lattice parameter, agreeing with other literature showing that the substitution of Cu in Ni_2MnGa of up to around 6 at.% at the expense of Mn reduces the austenite lattice parameter [91, 93]. Across all samples, lattice parameter was very similar at high temperatures for pre- and post-sintering (see Figure 5.21a). With decreasing temperature, the negative difference between pre- and post-sinter lattice parameter increased, i.e. the lattice parameter was smaller after sintering than before. This is discussed further in Section 5.3.3.2. NMG saw an increase in lattice parameter upon the first heat above room temperature (Figure 5.21a), attributed to difficulties fitting due to the high peak width to peak height ratio until ring formation at 350 °C, displayed by the plotted diffractograms in Figure 5.26a. This is similar for all samples, which had high peak width to peak height ratio until ring formation between 322-365 °C (Figure 5.21g and Figure

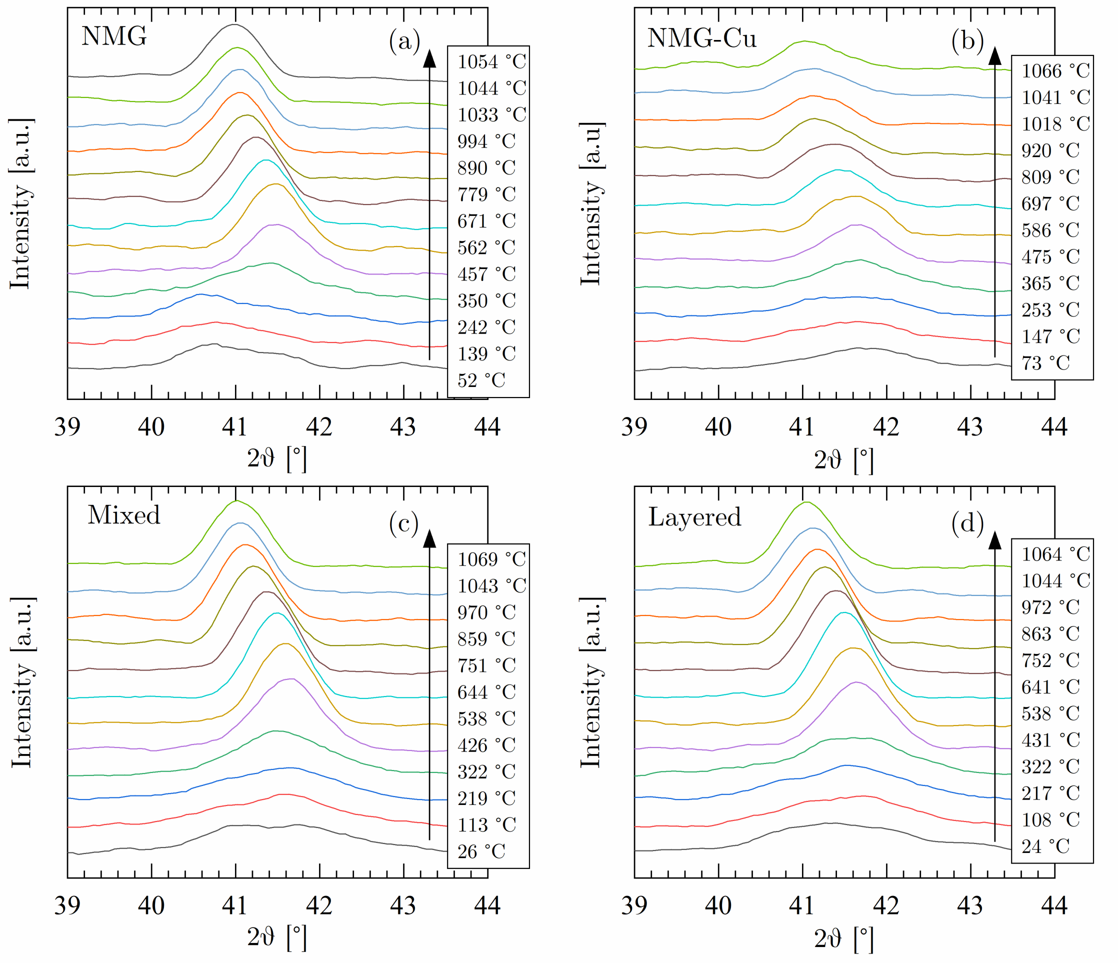

Figure 5.26: Diffractogram plots for each detector image set over the ramp up segment of the sintering heat treatment for (a) NMG, (b) NMG-Cu, (c) mixed, and (d) layered samples.

5.26). After peak coalescence around 450 °C, the data analysis becomes more sensible as the peak width to height ratio decreases significantly and Gaussian fitting is more apt. These broad, weak diffraction peaks in printed and cured green parts were significantly narrowed and strengthened during the heating and sintering steps due to stress relief of the ball-milled powder corresponding to a decrease in strain-broadening. Ball milling to achieve nano-sized Ni-Mn-Ga powder has been shown to result in 1.13-2.83 MPa of internal stress, which significantly broadens diffraction peaks but is relieved with appropriate heat treatments [193]. Internal stress can confidently be identified as the cause for peak broadening on sintering ramp up because broad peaks were not observed during the annealing ramp up segment (Figure 5.21g vs. Figure 5.22g).

All samples during sintering ramp up showed increased peak intensity upon heating until the 600-700 °C range, when peak intensities began to curve downward (see 5.21d). On initial heating, the stress relief of ball-milled powders improves the lattice quality, thus increasing the intensity of the diffraction peak. Around 600-700 °C, order breaks down and the B2' disordered phase emerges (the Mn and Ga sublattices become disordered). At the order-disorder transition, atoms have increased freedom of movement within the lattice, and the effects of residual stress from ball milling (T-dependent decrease in FWHM and increase in intensity, Figure 5.21d and Figure 5.21g) are no longer observed. Overholser experimentally and computationally determined the Ni-Mn-Ga pseudo-binary phase diagram, showing the expected transformation in the 600-700 °C range [244]. This disordering to form the B2' phase occurs at a slightly lower temperature in NMG-Cu because the Cu doping occurred at the expense of Mn, which [244] indicates lowers the order-disorder transition. Both after the order-disorder transition and during the annealing ramp up segment, temperature increase in the annealing treatment caused peak intensity to decrease. With ideal single crystals, an intensity decrease with rising temperature is expected based on the Debye-Waller temperature factor, which describes beam attenuation increase with a corresponding temperature increase. More beam attenuation translates to a decrease in the scattering centers (diffracting atoms), and therefore a decrease in peak intensity.

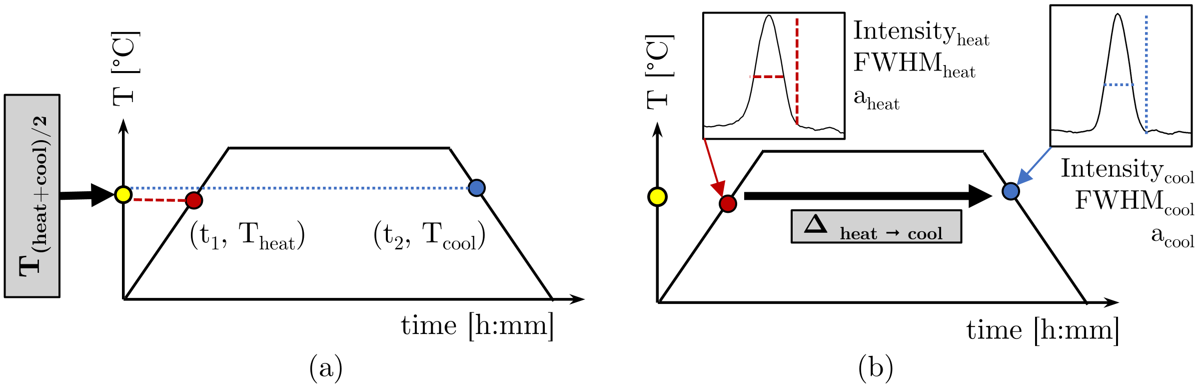

Figure 5.27: Graphical explanation of $\Delta_{heat\rightarrow cool}$ values plotted in Figure 5.28: (a) calculation of the horizontal axis temperature value in Figure 5.28 as an average of two similar temperatures from the heat up and cool down segments, and (b) calculation of the $\Delta_{heat\rightarrow cool}$ value for intensity, FWHM, or lattice parameter by subtracting the value obtained for the cooling segment from the value obtained for the heating segment at a similar temperature.

5.3.3.2 Pre- vs. Post-heat Treatment Structure

In-situ monitoring of structure throughout heat treatment allowed for the quantitativecomparison of structural parameters and diffraction peak properties before and after each stage of high temperature post-processing. Prior to the initial sintering step, diffraction peaks were broad with low intensity. To illustrate the change that occurred within the sample during sintering, diffraction patterns at similar temperatures from the heat up and cool down steps were compared (a process clarified graphically in Figure 5.27) and plotted in Figure 5.28 as value on cool down minus value on heat up. This shows the quantitative change between heating (pre-heat treatment) and cooling (post-heat treatment), evaluated at the same temperature.

Lattice parameter (Figure 5.28a,b) decreased for all samples between the pre- and post-sintering ramps ($\Delta a_{heat\rightarrow cool} < 0$), with the difference showing an increasing trend with increasing temperature, i.e. the heat and cool lattice parameter values were closer to each other the closer they were to the sintering hold temperature. For mixed, layered, and NMG-Cu samples, the $\Delta a_{heat\rightarrow cool}$ was around -0.05 Å for 110-150 °C, while it reached as low as

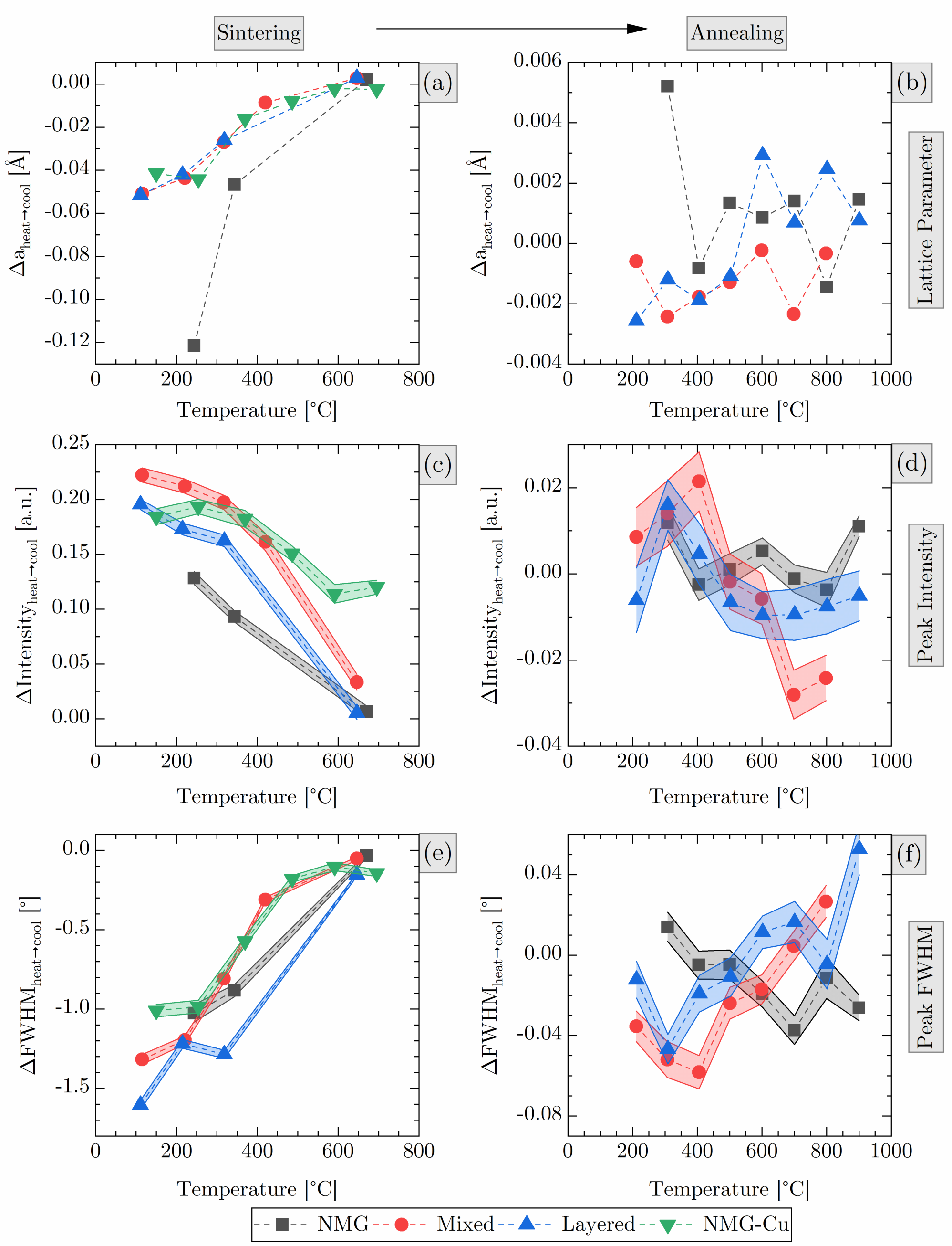

Figure 5.28: Change in lattice parameter (a,b), intensity (c,d), and FWHM (e,f) between the heating and cooling steps of sintering (a, c, e) and annealing (b, d, f) processes, evaluated at similar temperatures for each step. The horizontal temperature axis refers to the average between the similar evaluated temperatures.

-0.12 Å for ~245 °C for NMG. At the maximum temperature compared (645-695 °C), the differences in lattice parameter on heating and cooling were ~0.002 Å, well within error of calculation.

Peak intensity of the fitted Gaussian peak (Figure 5.28c,d) was compared across samples and temperature ranges as well, exhibiting a trend opposite to the lattice parameter. From pre- to post-sintering, peak intensity increased. Like lattice parameter though, upon approaching the sintering hold temperature, the intensity values at similar temperatures became more similar. Mixed, layered, and NMG-Cu samples differed in intensity values by slightly above or below 0.2 at the lowest temperature around 110-150 °C, with mixed and layered decreasing to a 0.01-0.03 difference at 645 °C. NMG-Cu decreased less, to a $\Delta Intensity_{heat \to cool}$ of 0.12 at almost 700 °C. The lowest comparable temperature data available for NMG was at 244 °C, where $\Delta Intensity_{heat \to cool}$ was lower than the other samples, at 0.13. NMG $\Delta Intensity_{heat \to cool}$ then coincided with layered and mixed values at high temperatures, nearly 0 just before 650 °C.

FWHM of the peak fit (Figure 5.28e,f), like lattice paramter, showed an increasing trend over temperature for a decrease in parameter between pre- and post-sintering as indicated by a $\Delta FWHM_{heat \to cool} < 0$, i.e. peaks were narrower post-sintering, but FWHM parameter values were closer to each other the closer they were to the sintering hold temperature. The layered sample showed a $\Delta FWHM_{heat \to cool}$ of -1.6° at 110 °C, NMG and NMG-Cu were similar with $\Delta FWHM_{heat \to cool}$ of around -1° at 150-250 °C, and the mixed sample had $\Delta FWHM_{heat \to cool}$ of around -1.2° to -1.3° from 115-220 °C. At higher temperatures, the difference between pre- and post-sintering became less, at or greater than $\Delta FWHM_{heat \to cool}$ of -0.15°. Error for the FWHM of the peak fit mostly ranged between 0.007-0.0018° (and propagated error is included in Figure 5.28c,e, so the $\Delta FWHM_{heat \to cool}$ is accepted to be affected by more than just fit errors. As detailed in Section 5.3.3.1, ball milling has a large effect on peak broadening pre-sintering.

Lattice parameter, intensity, and FWHM showed much less change between the heating and cooling steps of the annealing process, plotted in Figure 5.28b,d,f. $\Delta a_{heat \to cool}$ fell almost entirely within ±0.004 for all samples (presumed well within error bounds considering error propagation), $\Delta FWHM_{heat \to cool}$ between -0.07 and +0.05, and $\Delta Intensity_{heat \to cool}$ between -0.03 and +0.02. Compared to the differences seen during the sintering stage, these ranges are quite low. However, with the FWHM and intensity fit error ranges at 0.004-0.007° (FWHM) and 0.004-0.007 (intensity) with propagated error plotted in Figure 5.28d,f. $\Delta FWHM_{heat \rightarrow cool}$ increased with temperature for the mixed and layered samples and decreased slightly with temperature for NMG. $\Delta Intensity_{heat \rightarrow cool}$ was relatively constant for NMG and layered samples, decreasing for mixed.

5.3.3.3 Mixed vs. Layered Parts Though densities cannot be justifiably compared across different samples due to the inconsistencies between individual fabrication runs in the custom-built manual printer, it is a significant result that the density varied within the two sections of the layered part. This indicates that multi-material BJ3DP can also be used in applications where porosity needs to be tailored within a part. Of course, the materials incorporated must be similar enough that unavoidable diffusion is limited and not detrimental, or alternatively diffusion must be desired. Successful spatially-variant density also requires that one material have faster sintering kinetics (e.g. lower melting temperature, different powder size distribution). Here, NMG-Cu experienced significant melting at 1090 °C whereas the used NMG composition has been shown to begin partial melting at 1100 °C [183].

Compositional analysis of the final layered sample allows quantification of the anticipated diffusion across the material layer boundary through the measured 6 layers (Figure 5.23). Ni content was within ± 0.1 between the two powder compositions used in this study, so there was no driving force for Ni diffusion. Mn, Ga, and Cu did diffuse, however. Ga equilibrated within the 3 measured layers on each side of the material boundary, beginning around 20 at.% in the NMG layer furthest from the material boundary and ending around 25 at.% in the NMG-Cu layer furthest from the boundary. Mn however had not quite settled into the nominal composition at the edges of the measurement area. At the edges of the measured NMG and NMG-Cu layers, Mn content was around 29 at.% (nominal 30 at.%) and 21 at.% (nominal 19 at.%), respectively. Cu content remained 0 at.% at the furthest NMG layer from the boundary, and rose to 6 at.%, near to nominal.

Interdiffusion is a process that is dictated by composition gradient, atom mobility, and availability of diffusion paths. In this BJ3DP multi-material layered sample, a composition gradient exists for Mn, Ga, and Cu, but not for Ni. Though interdiffusion data has not been investigated for Cu-doped Ni-Mn-Ga alloys, ternary interdiffusion of Ni-Mn-Ga was studied by Zhou et al., with the finding that interdiffusion of Ni is greatest, followed by Mn and Ga [245]. It is worth noting that there is a plateau of composition for Mn and Cu within the two layers furthest from the multi-material layer boundary. Large amounts of porosity at the boundary between individual layers reduced the availability of diffusion paths and prevented Mn and Cu from achieving a smooth transition in composition. This effect was not as relevant for the NMG-Cu side since sintering kinetics were faster and less porosity existed.

Compositional homogeneity can also be indirectly inferred through the thermal transformation data (see Figure 5.25), since martensitic transformation (MT) is very sensitive to composition (namely, valence electrons per atom or e/a) in Ni-Mn-Ga Heusler alloys [66]. The NMG part had the expected single relatively narrow peak for MT. In contrast, the mixed-powder part showed an extremely wide transformation range from approximately 40-110 °C, indicating that even though compositional analysis showed homogeneity, microsegregation exists though it was not observed during EDS measurements. This segregation could exist in large particles that did not have enough time to equilibrate, or in particles in relative isolation due to pore surroundings or being positioned on the edge of the part. The layered part had three distinct MT events, with one of them coinciding with the NMG MT. Compositionally, there are two distinct compositions on the ends of the part (one being the original NMG) with their own transformation temperatures, and the diffusion region in the center where interdiffusion took place which has its own broad MT peak.

5.3.4 Summary

This study presents the first neutron diffraction experiments on multi-material layered, binder jet 3D-printed Ni-Mn(-Cu)-Ga samples with the purpose of laying a foundation for research into efficient magnetocaloric heat exchangers with gradient properties and desirable geometries. Also examined are the lattice parameter and peak fit parameter evolutions in-situ with heat treatment for Ni-Mn-Ga, Ni-Mn-Cu-Ga, a mixed-powder part, and a multi-material layered part. Quantitative evaluation of average lattice parameter during heat treatment was performed, and a comparison with pre- and post-heat treatments was presented. Multi-material layered parts produced in a single additive manufacturing run have never before been tested. It has here been demonstrated that such fabrication is possible and can produce parts with distinct phase transformation events. In addition, layered binder jet 3D printing provides the opportunity to selectively tailor density if the included materials have different sintering kinetics.

6.0 Conclusions and Future Works

Additive manufacturing (AM) of magnetocaloric effect (MCE) materials can expand possibilities for designing safe and efficient heat exchangers through increased geometrical freedom and the potential for single-piece layered printed parts with gradient properties. This work has assessed the viability of direct laser deposition (DLD) and powder bed binder jet 3D printing (BJ3DP) as means of MCE material heat exchanger fabrication.

Functional parts were manufactured by DLD, though a homogenization step was necessary, and composition control is a challenge since full melting occurs. Microstructurally, the features of overbuilt and properly-built parts were documented and compared. Despite the larger elemental segregation occurring in the dendrites of the overbuilt part, both types of builds were well-homogenized after heat treatment and showed evidence of martensite throughout the cross-section at room temperature. Phase analysis confirmed martensitic phase prevalence in homogenized samples, with a much-reduced amount of austenitic phase. Phase transformation and magnetic properties of the DLD-fabricated Ni-Co-Mn-Sn were comparable to those measured for parts fabricated by conventional methods. DLD is a promising route for processing of Ni-Mn-based MCE materials, after including a post-processing homogenization step.

Structurally stable Ni-Mn-Cu-Ga parts were also manufactured via BJ3DP. Without full melting during printing, final BJ3DP part composition was true to the powder, and thus powder properties were translated to the printed part. Functionality of BJ3DP parts with optimized post-processing met or exceeded the performance of similar MCE materials in the form of single crystals or ribbons, with a ΔT_{ad} of 2 °C under 2 T at 31 °C. Thermal cycling showed good stability with a ΔT_{ad} of approximately 1.65 °C for 100 cycles. Most notable for this part was the low thermal hysteresis of 1.2 °C for the minor loops during partial transformation from austenite to martensite. Pores left after the sintering process likely improved cycling stability by relieving constraints during volume expansion at the phase transformation.

The process knowledge for creating stable, functional BJ3DP Ni-Mn-based parts was transferred to a small-scale, custom-built binder jet 3D printer that had the capability of multi-material printing with multiple powder feeders. Single-composition, mixed-powder, and layered material parts were fabricated with Ni-Mn(-Cu)-Ga. Parts were then monitored *in-situ* with neutron diffraction during post-printing sintering and annealing heat treatments. Neutron diffraction results were analyzed to obtain lattice parameters and peak fit parameters (intensity and FWHM). Results of this study are: a quantitative evaluation of lattice and peak fit parameter evolution with heat treatments and characterization of the final parts post-annealing. Lattice parameter decreased after the sintering treatment and did not change much with annealing. Multi-material parts had a density variation across the composition boundary due to a difference in sintering kinetics.

With results of this investigation in mind, the hypotheses are revisited:

1. Both laser-based and binder jet additive manufacturing methods will be able to produce stable and functional MCE materials.
    1.1. Laser deposition will produce viable samples, after an optimized homogenization step.
    1.2. Binder jet 3D printing will produce viable samples, after an optimized sintering step.
2. A small-scale binder jet printer can be designed and fabricated to produce multi-material samples with little material waste.
    2.1. Sintering of mixed-powder samples will produce a nearly homogeneous composition.
    2.2. For two materials with different sintering properties, density can be tailored per set of layers in multi-material prints.
3. *In-situ* monitoring of sintering and annealing heat treatments of binder jet 3D printed samples can reveal structural evolution.
    3.1. Sintering treatment will change lattice parameter by relieving residual stresses and improving homogenization.
    3.2. Multi-material layered parts will exhibit multiple phase transformations.

As predicted in H1, stable and functional samples were produced by both laser-based and binder jet additive manufacturing. Both laser deposition and binder jet 3D printing required the expected post-processing treatments. For H2, a small-scale binder jet 3D printer was indeed fabricated and used to produce multi-material samples with little waste. Within the multi-material samples, mixed-powder samples (H2.1) did result in a nearly homogeneous composition when assessed with EDS area scans, but small-scale microsegregation was predicted based on width of transformation peak in thermal transformation data. In contrast, multi-material layered samples had distinct layers that did sinter at different rates, resulting in a density variation within the same part (per H2.2). As anticipated in H3.1, lattice parameter did change during the sintering process due to a relief of residual stresses obtained during ball milling preparation. Further lattice parameter changes could be attributed to some improved homogenization. Finally, the reality of hypothesis H3.2 can clearly be seen in the thermal properties of the layered part as multiple first-order peaks in the heat flow measurements, a step towards layered multi-material parts with gradient transformations, produced in a single manufacturing process.

6.1 Future Works: Continuation

There are a few research avenues which I believe are logical continuations to the presented work and use current capabilities and data:

1. Probe MCE properties in the printed parts from Section 5.3 using indirect measurements and the recently-completed direct MCE tester VSM attachment.
2. Perform interrupted heat treatment studies in-house to observe structural and property evolution with other methods.

6.1.1 Direct and Indirect MCE Measurements

Evaluating the magnetic properties of MCE materials is an important step towards gauging practical viability. $M(T)$ and $M(H)$ measurements should first be conducted on parts presented in Section 5.3. In addition, the same hysteresis-reducing partial transformation behavior that was shown in Figure 5.14 should be assessed.

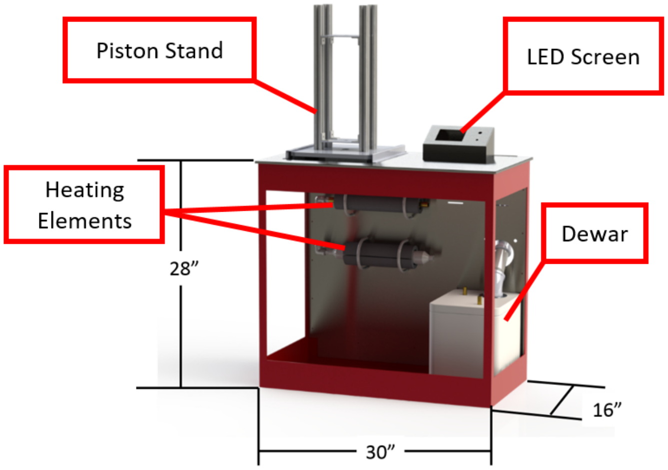

Figure 6.1: Cart containing air heating and cooling methods for direct MCE testing adapter for VSM, as well as the interactive LED screen and a holding area for the piston.

Recently, the capability has been developed to measure ΔT_{ad} in-house, and this should be used to gather additional data on samples from Section 5.3. I advised three teams of researchers who designed and built a magnetocaloric materials test stand for direct MCE measurements. The first team developed methods for heating and cooling air that will flow over a sample to change its base temperature and mounted a piston setup on the VSM electromagnet to inject the sample quickly into a magnetic field after it reaches a stable temperature. The second research group designed and built a containment cart (Figure 6.1), and coded an Arduino to control the air temperature and to run designated testing sequences where the air is heated, cooled, or stabilized as required. The third team transferred control from an LED screen to an interactive LabView interface and redesigned the piston stand to make sample exchange simple. Pending calibration and viability testing, the MCE test stand can be used to perform direct MCE measurements on BJ3DP samples.

If direct MCE testing is not feasible, indirect measurements can be made using a VSM oven attachment. As previously described in Section 2.3.2, this requires $M(T)$ loops from different stable temperatures for integration using the Maxwell equation (Equation 2.3).

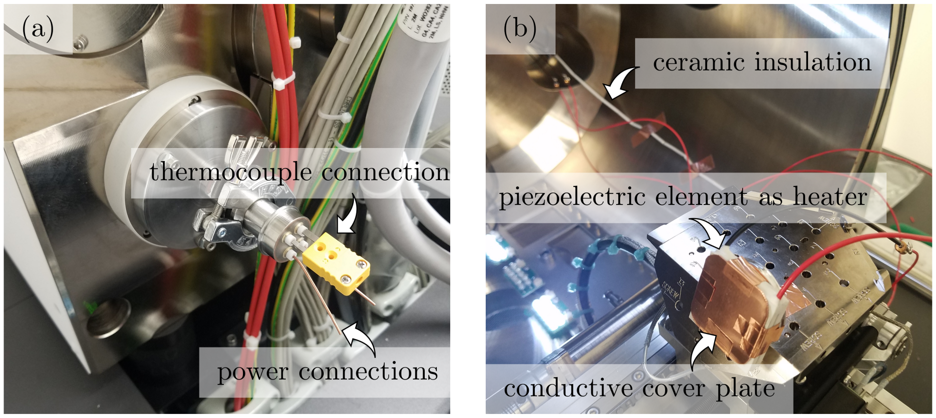

Figure 6.2: SEM feedthrough designed and built for heated EBSD. Portion external to the chamber is shown in (a), while components internal to the chamber are shown in (b).

6.1.2 Interrupted Heat Treatment Studies

Data from the E3 beamline can be clarified by experiments: heated XRD and interrupted heat treatments with quenching. Heated XRD can elucidate structure changes throughout the heating process by providing additional peaks for analysis. Interrupted heat treatment allows for structural analysis from parts taken to progressively higher temperatures. Namely, insights can be gained from progressive grain size analysis and porosity distribution (via microscopy and tomography), and resulting MCE functionality in the parts.

Heated EBSD could also complement the heated XRD and structural analysis from interrupted heat treatments by providing a visual and quantitative representation of the transformation to austenite. I have already helped to design and assemble a heated stage feed-through for the EBSD-equipped SEM, pictured fully installed in Figure 6.2.

6.2 Future Works: New Directions

The current work has opened curiosity pathways to new research, including:

1. Investigate binder types, binder burnout, and residue interactions for BJ3DP.
2. Design a testing system for magnetocaloric parts, print heat exchanger geometries, and test simulated in-service functionality of printed parts.
3. Expand studies to promising La(Fe,Si)$_{13}$- and Mn-Fe-based magnetocaloric material systems.
4. Study interaction between strength of first order transition and porosity.
5. Test effects of magnetic alignment in BJ3DP parts.
6. Use the design process to model and simulate heat transfer in novel heat exchanger geometries enabled by additive manufacturing.

6.2.1 Binder Burnout and Residue

One of the primary concerns for BJ3DP of impurity-sensitive materials is residual elements originating from the binder. It would be beneficial for the field to have a robust and systematic study of binder burnout temperatures and residues for magnetic functional materials. Similar work has been done for sand molds (see, e.g. [246]). The two readily-available commercial ExOne binders are solvent-based and water-based, though the company has recently debuted a low-carbon binder and an Oak Ridge National Laboratory collaboration has developed an *in-situ* crosslinking binder [247]. For any binder type that can be acquired, detailed thermo-gravitational analysis should be conducted to assess burnout temperatures both for the pure binder and for powder that has been mixed with binder. After binder burnout, composition should be measured, taking care to include the elements C and O. With impurity analysis conducted, the amount of residual elements can then be related to structural features and functional properties, as has been done for metal injection molding of La-Fe-Si-based MCE materials [179, 248].

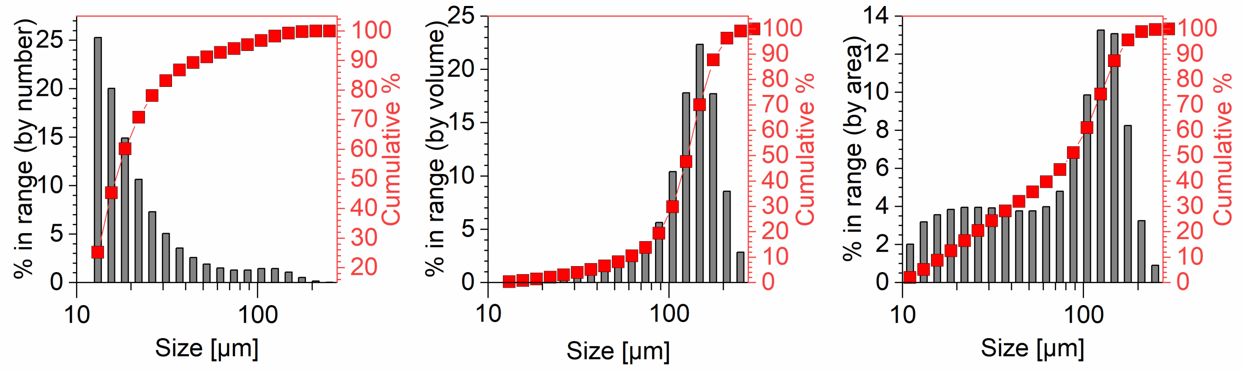

Figure 6.3: Size distribution for La(Fe,Si)$_{13}$-based powder.

6.2.2 Additional Promising MCE Materials

Though Ni-Mn-based magnetocaloric materials are beneficial for being non-rare-earth containing while maintaining favorable MCE properties, there are two other primary candidates for magnetic cooling: La(Fe,Si)$_{13}$-based and Mn-Fe-based alloys. Further investigations into binder jet printing of these two alloys would be beneficial.

Preliminary work has begun on a La(Fe,Si)$_{13}$-based alloy. Fe-La-Ce-Si-Mn powder from a collaborator has been characterized (Figure 6.3), printed, and cured. La has a high affinity for oxidation [149], which led the first BJ3DP parts to be unsuccessful when a water-based binder was used. After a switch to solvent-based binder, oxidation reduced and as-printed part quality improved. Thermal properties were then analyzed for as-received powder, powder heated to the curing temperature in air, and powder heated to the curing temperature in an argon atmosphere (Figure 6.4). Thermal transformation data collected for the as-received powder indicated a first-order transformation around 5 °C, and a Curie Temperature (T_C) around -64.4 °C on cooling. When the powder was heated to the curing temperature (180 °C for 2 h), the transformation peak on cooling shifted to around -5 °C and widened, but the T_C hardly shifted, to -64.6 °C. To test whether the temperature or the atmosphere during curing was the factor affecting the transformation temperature, the as-received powder was encapsulated in a argon-purged vacuum atmosphere and subjected to the heating process

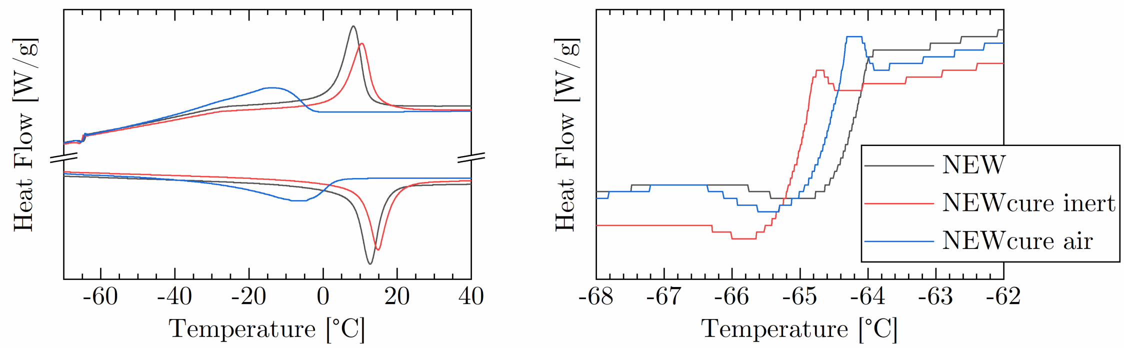

Figure 6.4: Thermal transformation data for as-received powder (NEW), as-received powder heated through curing conditions in air (NEWcure air), and as-received powder heated through curing conditions in an inert atmosphere (NEWcure inert). Full plot is on the left, and a magnified view of the low-temperature transformation is on the right.

again. Encapsulated and heated powder showed a slight increase in transformation temperature to around 10 °C on cooling, and little change in T_C, to -65 °C. This indicates a need for an inert atmosphere while curing green parts from binder jet 3D printing of Fe-La-Ce-Si-Mn.

To determine whether the thermal shift came from an obvious appearance of an oxide, or some clear change in structure, XRD analysis was conducted. Diffraction patterns as given in Figure 6.5 showed no additional phases, and no significant change in structure between the as-received powder, powder recovered from printing with either aqueous or solvent binders, and powder heated in an inert atmosphere. There was however a small shift from the aqueous and solvent residue powders (cured in air) to the as-received and inert-atmosphere heated powder.

Recognizing the need for consistent inert curing atmosphere for post-processing BJ3DP parts, I advised a team who designed an inert curing containment unit. This inert curing box is nearly completed, and a design version is shown in Figure 6.6. In addition, more consistent printing results can be obtained with a commercial BJ3DP printer, though powder bed volume requirements are higher. With limited amounts of powder, a small build bed box adapter for the commercial ExOne X-1 Lab printer is necessary. I advised a team

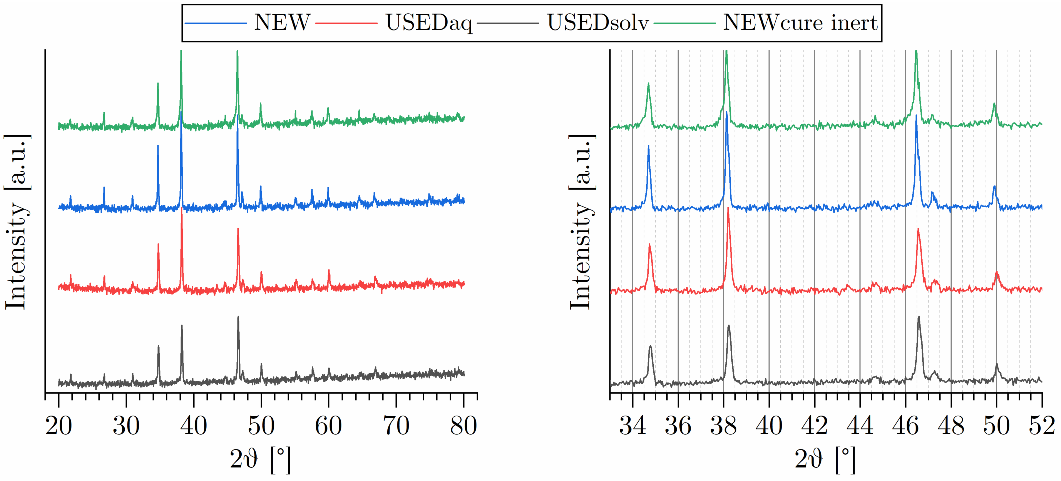

Figure 6.5: XRD plots of as-received powder (NEW), powder retrieved from prints with aqueous water-based (USEDaq) and solvent (USEDsolv) binders, and powders heated in an inert atmosphere (NEWcure inert). The right-hand plot magnifies the most interesting region from the left-hand plot.

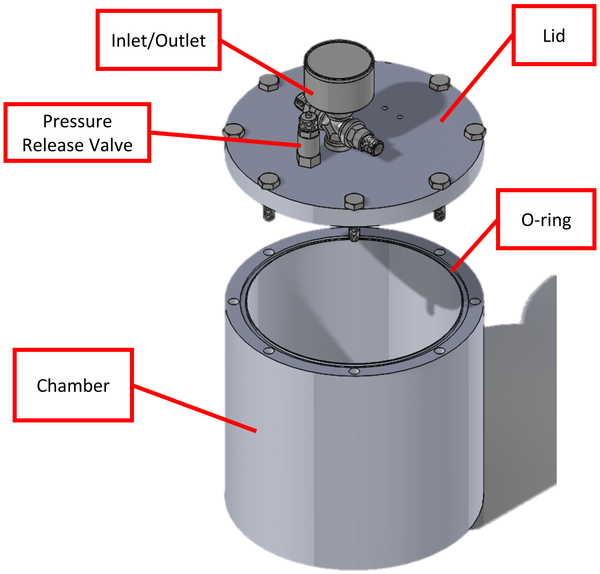

Figure 6.6: Design of inert curing box.

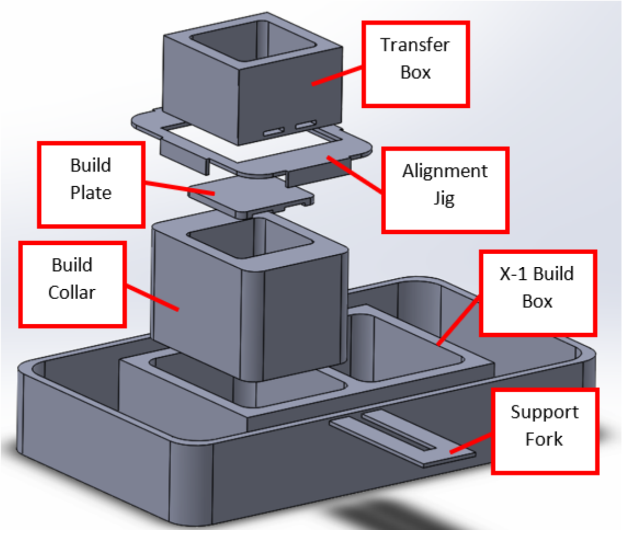

Figure 6.7: Final design of build bed reducer.

who designed such a build bed adapter and transfer system (shown in Figure 6.7), which is completed but not fully tested.

While Ni-Mn-based Heusler alloys have not yet been commercialized, Mn-Fe-P-Si alloys were sold by BASF beginning in 2013 [249] and were in a prototype wine cooler in 2015 [250]. (Mn,Fe)(P,X) alloys form a hexagonal P-62m Fe_2P-type structure that participates in a magneto-elastic, itinerant metamagnetic phase transition from paramagnetic to ferromagnetic, where the lattice parameter suddenly changes sharply but the structure remains the same [6, 59]. This category of magnetic refrigerants was first reported in 2002 by Tegus et al. as the $MnFeP_{1\text{-}x}As_x$ system, where $0.15 \leq x \leq 0.66$ and the P/As ratio could be tuned to tailor T_C [251]. Research quickly turned to the elimination of the toxic element As from the compound, and this was successfully achieved with $Mn_{1.2}Fe_{0.8}P_{1\text{-}x}Ge_x$ in 2006 [252]. Since Ge is a costly element, the compound was refined further into $MnFeP_{1\text{-}x}Si_x$ with $0.28 \leq x \leq 0.64$, and the Fe_2P-type structure was retained [253]. These acceptable concentrations were slightly different in a phase diagram published by Höglin et al in 2015 [254] where the Fe_2Si-forming range was reported to be about $0.24 \leq x < 0.5$, temperature-dependent. Off-stiochiometric $Mn_xFe_{1.95\text{-}x}P_{0.5}Si_{0.5}$ shifts from a second order to a first order phase transition with an increase in the Mn/Fe ratio, with $x < 1.40$ showing a first order transformation [59]. Further improvements to performance have been made with small alloying additions such as B or C [40, 128, 140]. Several review papers have discussed the evolution of (Mn,Fe)(P,X) materials, and the reader is referred to these for further reading [6, 60, 255]. While Mn-Fe-P-Si compounds have a lower relative cooling power compared to La-Fe-Si and Gd compounds, the major benefit to developing Mn-Fe-P-Si is the presence of only cheap and abundant elements within the composition, in contrast with those containing La or Gd. Since these compositions are commercialized and deemed quite viable, additive manufacturing investigations should be extended to Mn-Fe-based alloys.

6.2.3 Phase Transition Order and Porosity

Due to published data, it is expected that an increase in porosity will increase the magnetocaloric effect for the strong first order phase transition (FOPT) magnetocaloric material (Ni-Mn-Cu-Ga), and that an increase in porosity will decrease the magnetocaloric effect for the weak FOPT magnetocaloric material (Mn-Fe-P-Si or Fe-La-Ce-Si-Mn). Practical functionality is also a function of hysteresis losses and mechanical stability, and it is expected that hysteresis will decrease and stability can experience a moderate increase for both strong and weak FOPT materials with an ideal level of porosity.

A graphical representation of the future works project materials and experiments is shown in Figure 6.8. Two materials will be used - one a strong FOPT material, and the other a weak FOPT material (listed as Mn-Fe-based but could be La(Fe,Si)$_{13}$-based if heat treatment conditions are adjusted accordingly) - and each will undergo two experiments for response surfaces. Since the testing of functionality and stability requires an understanding of microstructure development due to sintering conditions, the first experiment is a design of experiments response surface (here referred to as the structural response surface) that will help to determine the effects of powder size, sinter temperature, and sintering time on bulk porosity and grain size. Using the results from the first response surface, the second (functional) response surface will be constructed using the input factors of bulk porosity, grain size, and cooling process to evaluate the responses of cycling cracking, ΔT_{ad}, and

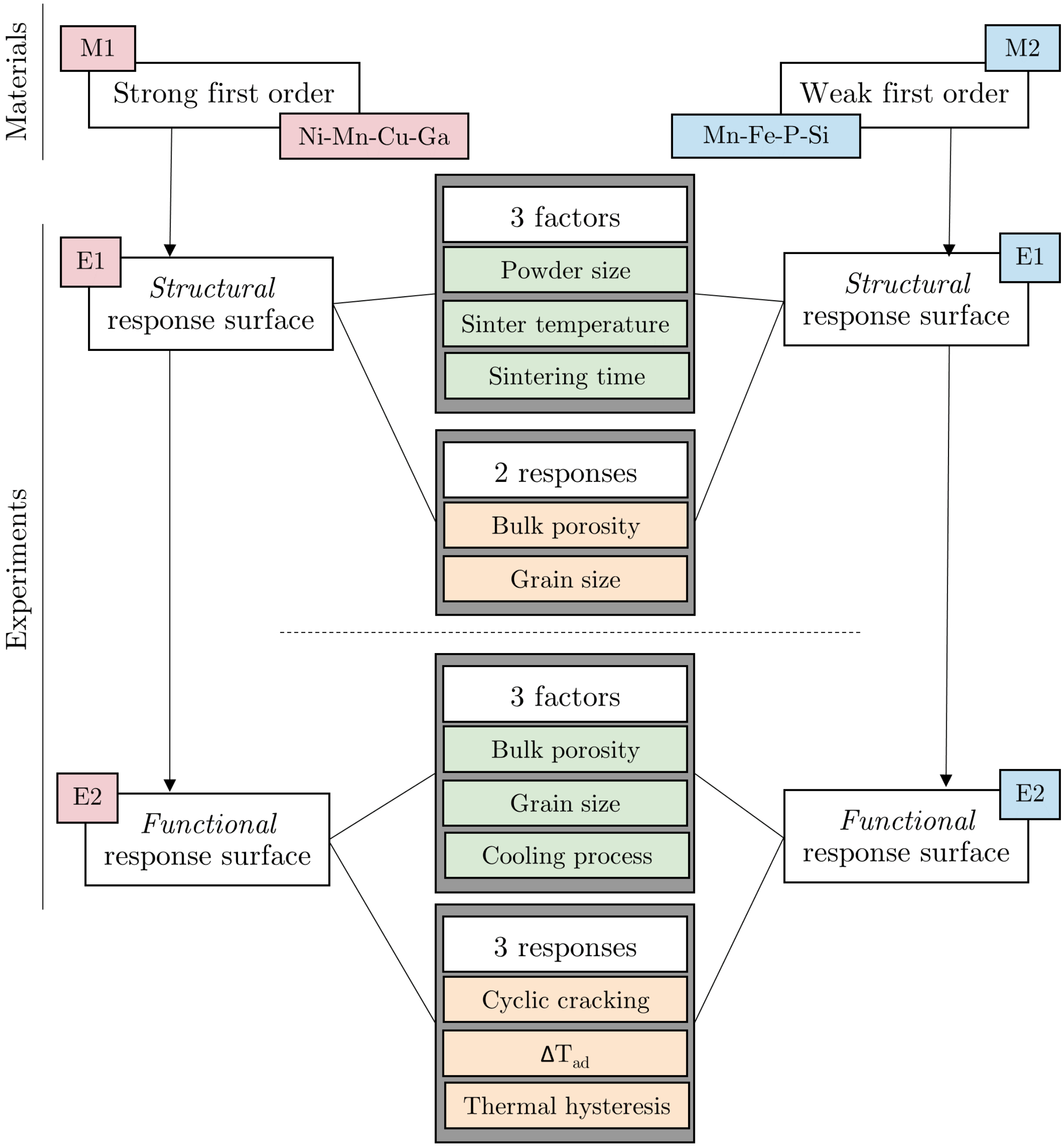

Figure 6.8: Graphical representation of the materials and experiments to study strong vs. weak first order materials.

thermal hysteresis. Experiments are denoted in Figure 6.8 by their constituent material as well as their experiment number (e.g. M1.E1 for the structural response surface for the strong FOPT material).

Aspects of the experiment that will not vary are listed below:

- For this entire study, the alloy compositions will be held constant unless the chosen compositions are not functional after printing and sintering. Knowledge gained about porosity effects is transferable to different (similar) compositions, so the additional variable of changing composition is not necessary.
- Ordering step at 400 °C for 1 h (M1) or 850 °C for 20 h (M2).
- During the sintering thermal profile, binder burnout will occur via a 30 min holding time at 700 °C.
- Samples will be cylinders of 1 mm height and diameter.

Responses will be measured in the following ways:

- **Porosity** will be measured using Archimedes' principle to determine bulk density.
- **Grain size** will be measured through mounting, polishing, and etching and subsequent image analysis of optical micrographs.
- **Cyclic cracking** will be measured using micro-computed tomography. Since unmounting and remounting during cycling can alter results, a high level of cycling will be chosen (300-500 cycles), and samples will be removed after that number of cycles and analyzed using µCT to find crack surface area per material volume.
- ΔT_{ad} will be measured using a custom-built direct MCE testing machine, which is constructed but not yet tested and calibrated. The same machine can be used to conduct cycling tests.
- **Thermal hysteresis** will be measured using an $M(T)$ test in the VSM. If temperature requirements are out of the range of VSM capabilities, hysteresis can also be measured using DSC data.

6.2.4 Magnetic Alignment in BJ3DP Parts

In accordance with a patent application filed by our group, magnetic alignment during binder jet 3D printing may improve structure and properties of MCE materials [256]. When the powder is magnetic (ball milled powder must be stress-relieved even if the composition is magnetic), it will tend to align along the field lines of an applied magnetic field. This can be expanded for Ni-Mn-based FSMAs because in the martensitic phase, the unit cell has an easy axis of magnetization. If particles can be aligned according to this easy axis of magnetization, then a textured material may result. Less variation in the unit cell alignment could improve MCE (and other magnetic functional) behavior.

Within the custom-built binder jet 3D printer, a capability was included to add an electromagnetic coil to generate a magnetic field. This field was tested for magnitude within a filled powder bed, and results are plotted in Figure 6.9. With increasing current, the field increased in a linear manner. For printing tests, the field was maintained at 8 mT by providing a 4 A current. Higher fields generated large amounts of heating, and caused the powder to stack far above the powder bed surface, which is not viable for printing. For further investigation (and currently under development) is a method to apply the magnetic field such that the field lines are parallel to the print bed rather than perpendicular.

6.2.5 Heat Transfer in 3DP Magnetocaloric Heat Exchangers

Using additive manufacturing for fabrication provides unprecedented geometrical freedom for the design of heat exchangers. Without typical constraints, new heat exchanger designs can be imagined and evaluated via constitutive equations describing heat transfer and fluid flow. I advised a team to develop a numerical model to describe a newly-designed heat exchanger geometry as shown in Figure 6.10. This model will next be further verified, refined to include full cooling cycles and the time domain, and extended to 3D simulation.

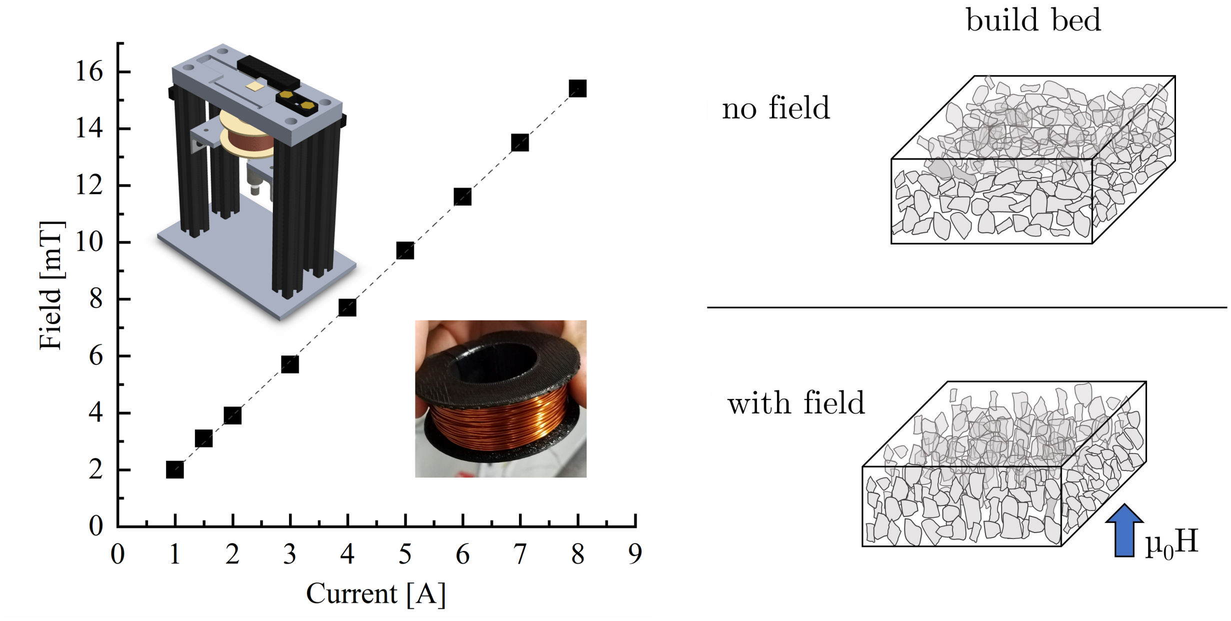

Figure 6.9: Field vs. current for powder bed of the custom binder jet printer, and schematic showing the effects of a magnetic field on the powder bed when the powder is magnetic.

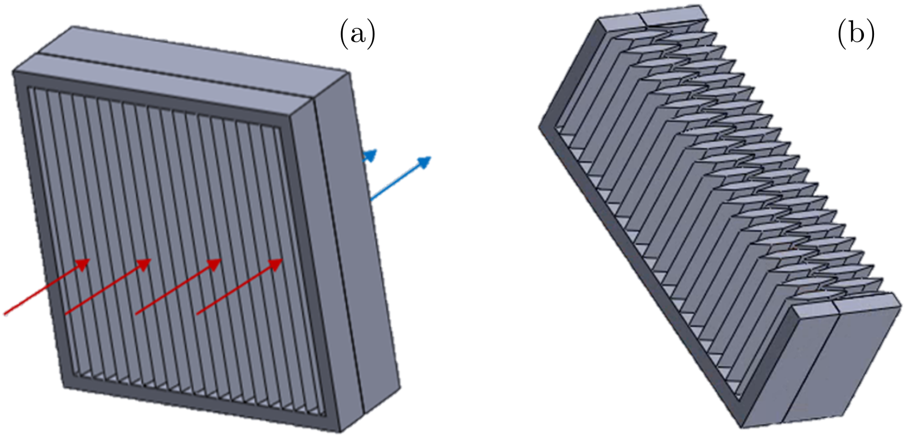

Figure 6.10: Heat exchanger design, enabled by 3D printing. (a) Flow direction indicated on the part. (b) Cross-section showing pointed fin design.

7.0 Broader Outlook

The current work has been a foray into the intersection between the large and extensive communities of magnetocaloric research and additive manufacturing, and the intended broader impact is an exchange of expertise between the MCE materials community and the additive manufacturing one. With the combined knowledge of the fields, researchers will be able to overcome the manufacturing and materials challenges presented and produce safer, more efficient cooling solutions.

Part quality is affected by a large number of factors in AM methods, and many of them are intertwined: machine parameters (laser type and optics, spot size, temperature distribution in the chamber, build plate material and temperature, powder feed method), feedstock parameters (flowability, quality, size distribution), environmental state (humidity, shielding gas), and process parameters (laser power and scan speed, scan spacing and hatch strategy, layer thickness, roller speed, binder saturation). For a set of materials systems whose functional performance depends on consistency and predictability in all aspects of composition and microstructure, AM methods present a significant challenge as a fabrication route. However, the potential is too great to ignore: AM could unlock enhanced functionality and applicability by allowing geometrical freedom, enabling gradient structures, and avoiding the need for subtractive manufacturing of brittle materials. Breaking AM into the broad categories of *laser-based* and *binder jetting*, challenges and benefits can be identified for each, and this overview is presented in Table 7.1.

To move AM of MCE and other functional magnetic materials (FMM) forward, predictability of outcomes must first be improved. Much of the current useful work in this area is individual studies of small sets of parameters, indicating the effects of and interaction between those parameters for a specific FMM (e.g. [146]). While these works are important steps on the road of progress, true leaps will be made by enabling predictive modeling of process outcomes: structural, compositional, and functional.

Process maps for individual material systems are an important aspect of advancing predictive modeling, but must be used with caution when not all other variables of the process

Table 7.1: AM methods, challenges, and benefits for MCE materials

AM Method	Challenges	Benefits	Related References
Laser-based	microsegregation	high density	[112, 143, 146, 150, 182]
	residual stress	no binder	
	phase change (liquid)	layered printing	[139, 175, 189, 191, 257]
	evaporative element loss	gradient structures	
Binder Jetting	post-processing required	structure retention	[183–185, 187, 188]
	consistency across prints	layered printing	
	diffusion during sintering	gradient structures	
	binder contamination		

are replicated [258]. Translation of optimal parameters to new materials without needing to test a wide range of parameter combinations enables smarter initial predictions [259]. Taking a more reactive approach during the printing, *in-situ* monitoring systems are being developed to tailor print quality, sometimes accompanied by the ability to automatically adapt parameters during the print [260, 261]. All of these advancements rely on processing an increasing amount of information about the manufacturing method. Integrating machine learning with more extensive metrology during the manufacturing process is likely the most promising solution for controlling the many variables in AM processes [262].

AM is a field that is advancing at an astounding pace. It is inevitable that a collective understanding of predictive modeling will emerge from the accumulation of the work done by many researchers. Once AM no longer has such an unpredictable nature, the expertise of the functional magnetic materials (FMM) community can be most effectively applied. Initial studies on AM of FMM with incremental parameters and limited sets of parameters can be used as a starting point when using machine learning tools to recognize structure and composition, providing insight into how process modifications may generate improved materials and devices. The dedicated FMM community must be prepared to take full advantage of predictive modeling and data-driven manufacturing, leveraging the ability to tailor composition and porosity while building highly efficient heat exchangers that are unconstrained by typical geometric requirements.

Appendix Time-Temperature-Parameter Plots

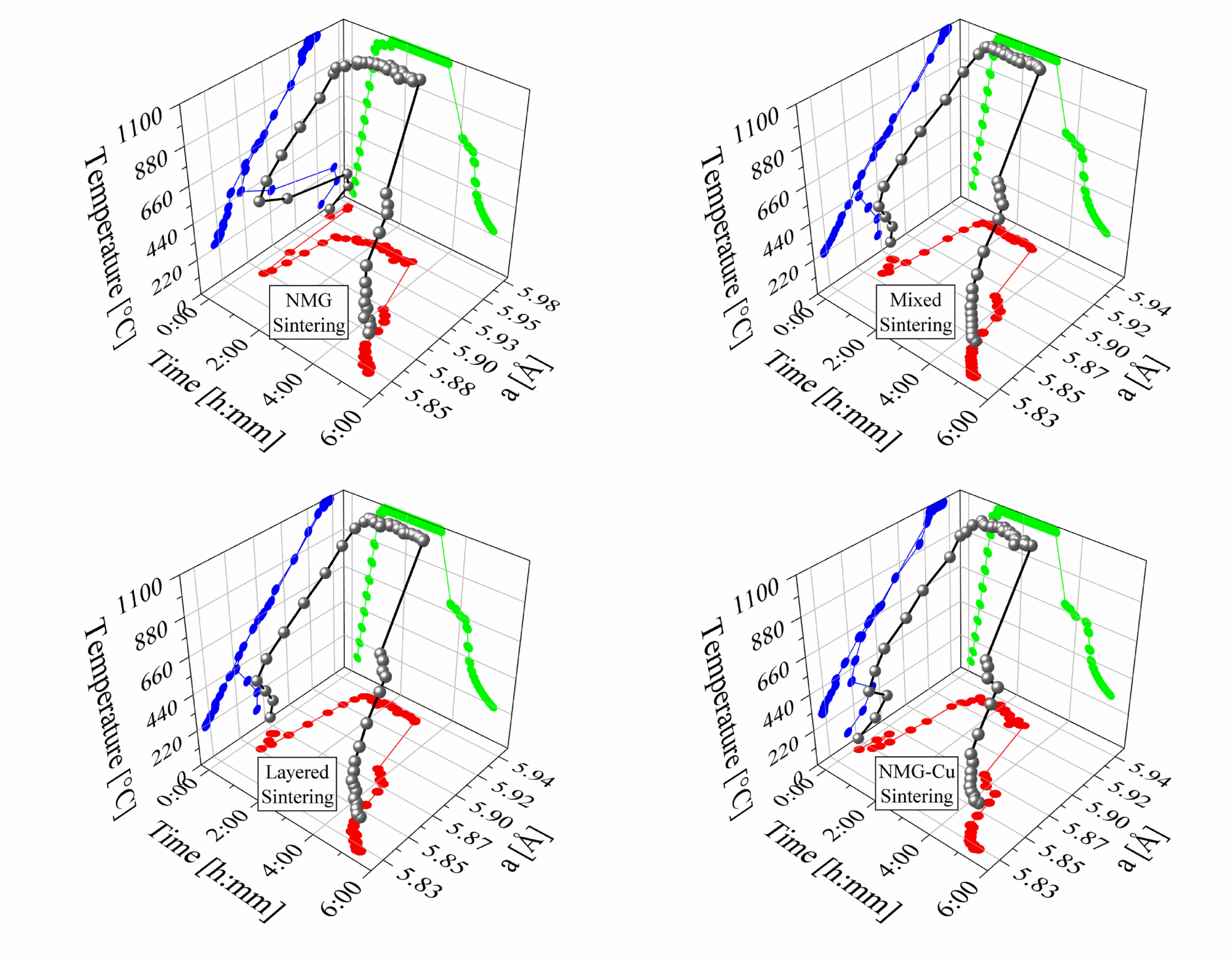

Figure A1: Time-temperature-lattice parameter plots for the sintering process.

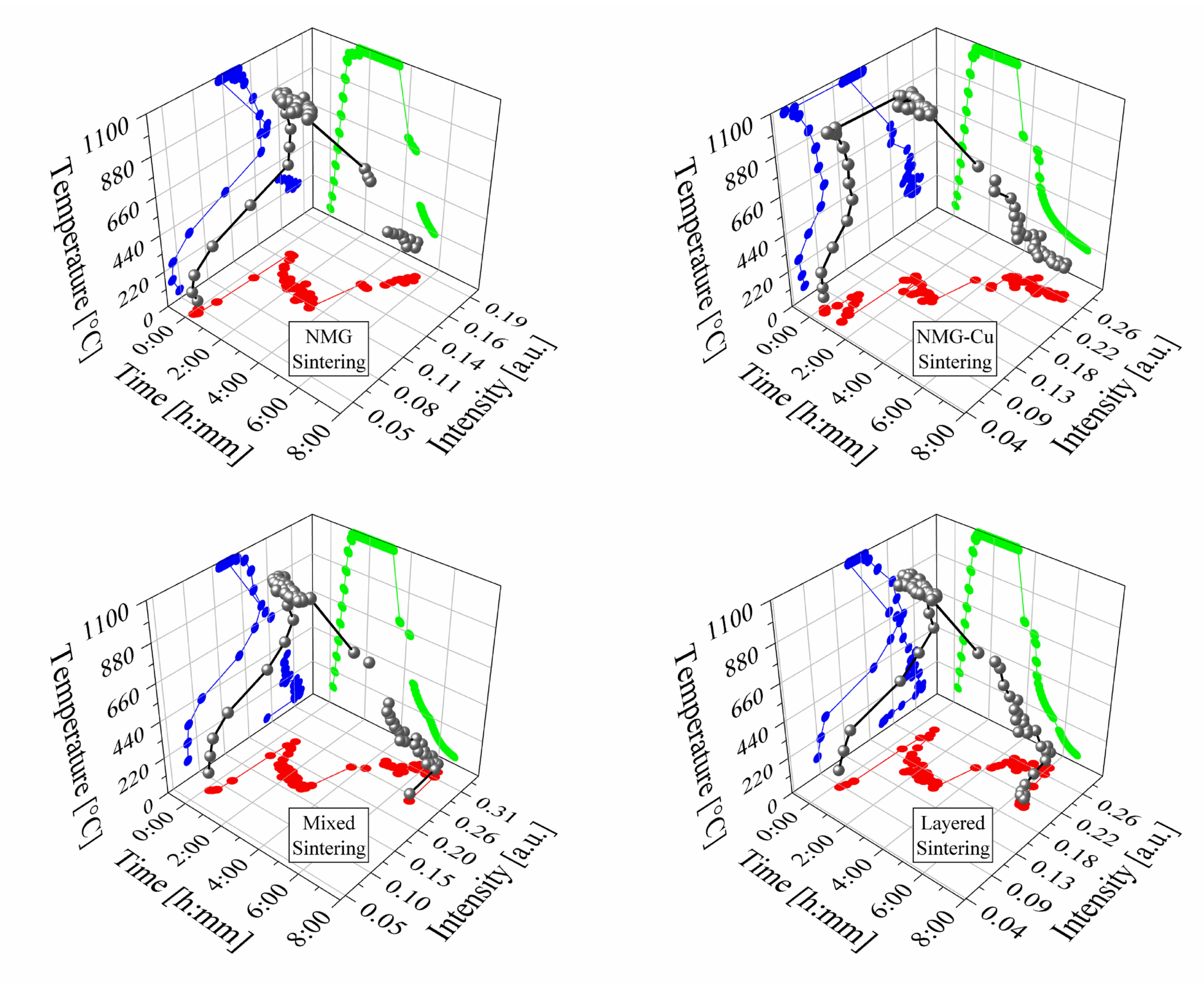

Figure A2: Time-temperature-intensity plots for the sintering process.

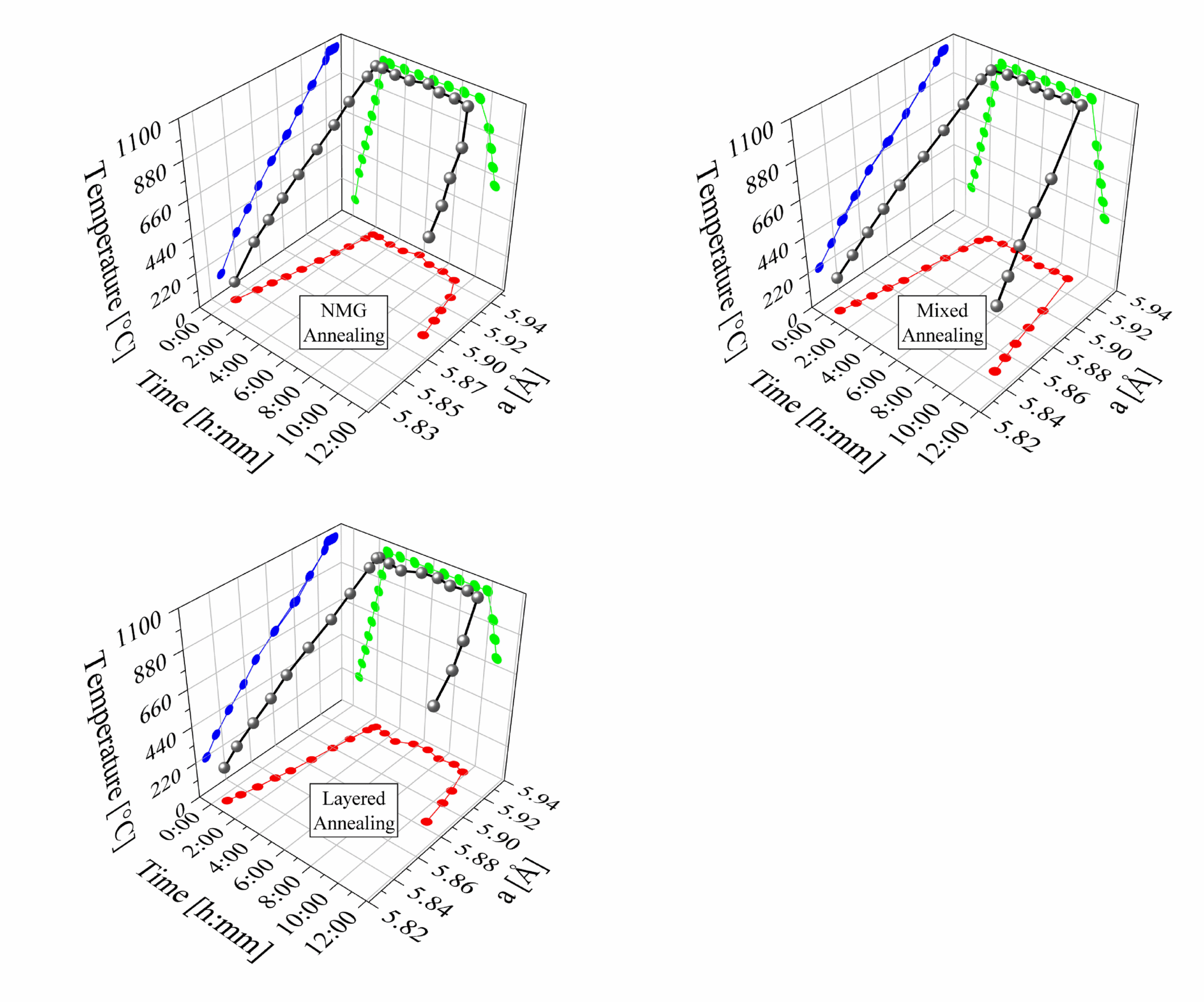

Figure A3: Time-temperature-lattice parameter plots for the annealing process.

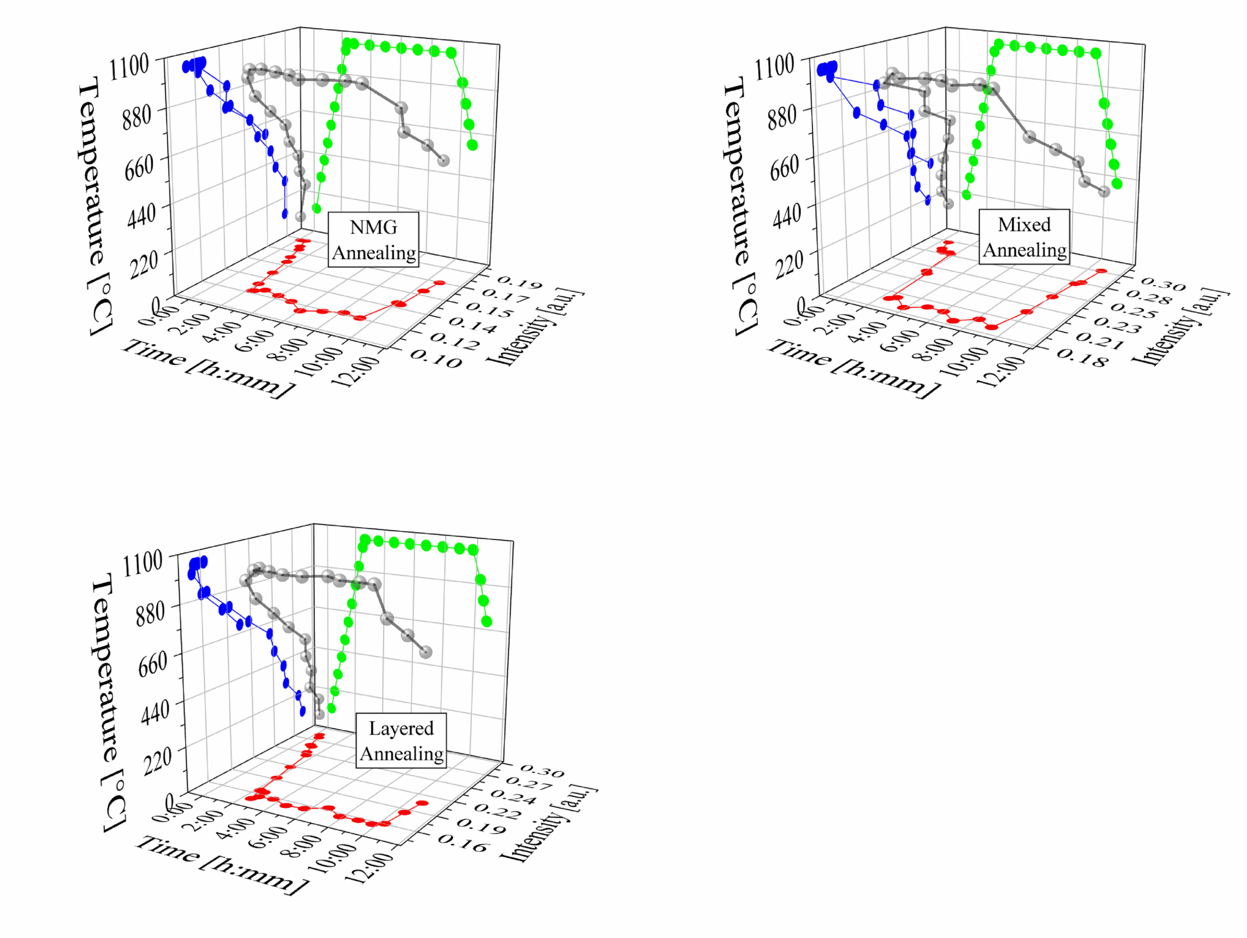

Figure A4: Time-temperature-intensity plots for the annealing process.

Bibliography

[1] International Energy Agency. *The Future of Cooling: Opportunities for energy-efficient air conditioning*. OECD, may 2018.

[2] International Energy Agency. *World Energy Outlook 2019*. World Energy Outlook. OECD, nov 2019.

[3] International Energy Agency. *World Energy Outlook 2017*. OECD, 2017.

[4] Vitalij K. Pecharsky and Karl A. Gschneidner. Magnetocaloric effect and magnetic refrigeration. *Journal of Magnetism and Magnetic Materials*, 200(1-3):44–56, 1999.

[5] Sebastian Fähler and Vitalij K. Pecharsky. Caloric effects in ferroic materials. *MRS Bulletin*, 43(4):264–268, 2018.

[6] Julia Lyubina. Magnetocaloric materials for energy efficient cooling. *Journal of Physics D: Applied Physics*, 50(5):053002, 2017.

[7] Nihar Shah, Max Wei, Virginie Letschert, and Amol Phadke. Benefits of Leapfrogging to Superefficiency and Low Global Warming Potential Refrigerants in Room Air Conditioning. *Berkeley: LBNL*, LBNL-10036, 2015.

[8] LG Electronics U.S.A. Inc. LSXS26386S: Ultra Large Side-By-Side Refrigerator with Door-in-Door™, 2015.

[9] LG Electronics U.S.A. Inc. LDS5540: Semi-Integrated Dishwasher w/ Flexible EasyRack™ Plus System, 2016.

[10] EPA. Information on Levels of Environmental Noise Requisite to Protect Public Health and Welfare with an Adequate Margin of Safety, 1974.

[11] Shin-ichi Sato, Jin You, and Jin Yong Jeon. Sound quality characteristics of refrigerator noise in real living environments with relation to psychoacoustical and autocorrelation function parameters. *The Journal of the Acoustical Society of America*, 122(1):314–325, 2007.

[12] Cooltech Applications. Magnetic Refrigeration: Study Case, 2017.

[13] John P. Rafferty. Montreal Protocol, 2011.

[14] Michael Irving. Magnetic fridge eliminates gases, drastically reduces energy use, jun 2016.

[15] Professional Services Close-Up. Cooltech Applications Unveils Magnetic Cooling System for Commercial Refrigeration, jun 2016.

[16] Camfridge. Our Technology, 2018.

[17] Jean Baptiste Chaudron, Christian Muller, Michael Hittinger, Michel Risser, and Sergiu Lionte. Performance measurements on a large-scale magnetocaloric cooling application at room temperature. *Refrigeration Science and Technology*, 2018-Janua(September):137–142, 2018.

[18] Sergiu Lionte, Alexander Barcza, Michael Hittinger, Michel Risser, Christian Muller, and Matthias Katter. Recent experimental results of first order LaFeSi-based magnetocaloric materials in an Active Magnetic Regeneration device. *Refrigeration Science and Technology*, 2018-Janua:56–61, 2018.

[19] Ilana Koegelenberg. German Researchers Developing a New Type of Magnetocaloric Heat Pump. *Accelerate Magazine*, (104):80–81, 2019.

[20] Sebastian Fähler, Ulrich K. Rößler, Oliver Kastner, Jürgen Eckert, Gunther Eggeler, Heike Emmerich, Peter Entel, Stefan Müller, Eckhard Quandt, and Karsten Albe. Caloric Effects in Ferroic Materials: New Concepts for Cooling. *Advanced Engineering Materials*, 14(1-2):10–19, feb 2012.

[21] Sean McGowan. Future focus. *HVAC&R Nation*, (111):21–22, may 2018.

[22] William Thomson. Cyclopedia of the Physical Sciences. In J.P. Nichol, editor, *Cyclopedia of the Physical Sciences*, page 838. Richard Green and Company, London and Glasgow, 1860.

[23] Emil Warburg. Über einige Wirkungen der Coërcitivkraft. *Annalen der Physik*, 249:141–164, 1881.

[24] Anders Smith. Who discovered the magnetocaloric effect? Warburg, Weiss, and the connection between magnetism and heat. *European Physical Journal H*, 38(4):507–517, 2013.

[25] Pierre Weiss and Auguste Piccard. Le phénomène magnétocalorique. *J. Phys. Theor. Appl.*, 1917.

[26] P. Debye. Einige Bemerkungen zur Magnetisierung bei tiefer Temperatur. *Annalen der Physik*, 386(1):1154–1160, 1926.

[27] W.F. Giauque. A thermodynamic treatment of certain magnetic effects. A proposed method of producing temperatures considerably below 1 K absolute. *Journal of the American Chemical Society*, 49(8):1864–1870, 1927.

[28] W. F. Giauque and D. P. MacDougall. Attainment of temperatures below 1 absolute by demagnetization of Gd2(SO4)3 - 8H2O, 1933.

[29] Georges Urbain, Pierre Weiss, and Félix Trombe. Un nouveau métal ferromagnétique, le gadolinium. *Comptes Rendus*, 200:2132–2134, 1935.

[30] G. V. Brown. Magnetic heat pumping near room temperature. *Journal of Applied Physics*, 47(8):3673–3680, aug 1976.

[31] Claudine Lacroix. Introduction to magnetism. *Lecture Notes in Physics*, 697:1–13, 2006.

[32] Anja Waske, Markus E. Gruner, Tino Gottschall, and Oliver Gutfleisch. Magnetocaloric materials for refrigeration near room temperature. *MRS Bulletin*, 43(4):269–273, 2018.

[33] T. Kihara, X. Xu, W. Ito, R. Kainuma, and M. Tokunaga. Direct measurements of inverse magnetocaloric effects in metamagnetic shape-memory alloy NiCoMnIn. *Physical Review B - Condensed Matter and Materials Physics*, 90(21):1–6, 2014.

[34] M.A. Benedict, S.A. Sherif, M. Schroeder, and D.G. Beers. The impact of magnetocaloric properties on refrigeration performance and machine design. *International Journal of Refrigeration*, 74:576–583, feb 2017.

[35] O. Gutfleisch, T. Gottschall, M. Fries, D. Benke, I. Radulov, K. P. Skokov, H. Wende, M. Gruner, M. Acet, P. Entel, and M. Farle. Mastering hysteresis in magnetocaloric materials. *Philosophical Transactions of the Royal Society A: Mathematical, Physical and Engineering Sciences*, 374(2074):20150308, 2016.

[36] Tino Gottschall, Konstantin P. Skokov, Dimitri Benke, Markus E. Gruner, and Oliver Gutfleisch. Contradictory role of the magnetic contribution in inverse magnetocaloric Heusler materials. *Physical Review B*, 93(18):2–7, 2016.

[37] V. Pecharsky, K. Gschneidner, A. Pecharsky, and A. Tishin. Thermodynamics of the magnetocaloric effect. *Physical Review B*, 64(14):144406, sep 2001.

[38] J. Romero Gómez, R. Ferreiro Garcia, A. De Miguel Catoira, and M. Romero Gómez. Magnetocaloric effect: A review of the thermodynamic cycles in magnetic refrigeration. *Renewable and Sustainable Energy Reviews*, 17:74–82, 2013.

[39] A Kitanovski, U Plaznik, J. Tušek, and A. Poredoš. New thermodynamic cycles for magnetic refrigeration. *International Journal of Refrigeration*, 37:28–35, jan 2014.

[40] F. Guillou, H. Yibole, G. Porcari, L. Zhang, N. H. Van Dijk, and E. Brück. Magnetocaloric effect, cyclability and coefficient of refrigerant performance in the MnFe(P, Si, B) system. *Journal of Applied Physics*, 116(6), 2014.

[41] Gaofeng Wang. *Magnetic and Calorimetric Study of the Magnetocaloric Effect in Intermetallics Exhibiting First-order Magnetostructural Transitions.* PhD thesis, Universidad de Zaragoza, 2012.

[42] Daniel Salazar-Jaramillo, P. Álvarez-Alonso, P. Lázpita, J.L. Sánchez-Llamazares, P. Gorria, J.A. Blanco, and V.A. Chernenko. Magnetocaloric Effect in Specially Designed Materials. In *Magnetic Nanostructured Materials: From Lab to Fab*, chapter 7, pages 199–244. Elsevier, Amsterdam, 2018.

[43] Y.I. Spichkin and R.R. Gimaev. Experimental methods of the magnetocaloric effect studies. *International Journal of Refrigeration*, 37:230–236, jan 2014.

[44] Anders Smith, Christian R.H. Bahl, Rasmus Bjork, Kurt Engelbrecht, Kaspar K. Nielsen, and Nini Pryds. Materials challenges for high performance magnetocaloric refrigeration devices. *Advanced Energy Materials*, 2(11):1288–1318, 2012.

[45] P. Álvarez-Alonso, J. López-García, G. Daniel-Perez, D. Salazar, P. Lázpita, J.P. Camarillo, H. Flores-Zuñiga, D. Rios-Jara, J.L. Sánchez-Llamazares, and V.A. Chernenko. Simple Set-Up for Adiabatic Measurements of Magnetocaloric Effect. *Key Engineering Materials*, 644(June):215–218, 2015.

[46] S. Jeppesen, S. Linderoth, N. Pryds, L. Theil Kuhn, and J. Buch Jensen. Indirect measurement of the magnetocaloric effect using a novel differential scanning calorimeter with magnetic field. *Review of Scientific Instruments*, 79(8), 2008.

[47] S. Yuce, N. M. Bruno, B. Emre, and I. Karaman. Accessibility investigation of large magnetic entropy change in CoMn1-xFexGe. *Journal of Applied Physics*, 119(13), 2016.

[48] Tomasz Plackowski, Yuxing Wang, and Alain Junod. Specific heat and magnetocaloric effect measurements using commercial heat-flow sensors. *Review of Scientific Instruments*, 73(7):2755, 2002.

[49] Mohamed Balli, Daniel Fruchart, Damien Gignoux, and Ryszard Zach. The "colossal" magnetocaloric effect in Mn1-x Fe x As: What are we really measuring? *Applied Physics Letters*, 95(7):1–4, 2009.

[50] Kun Xu, Zhe Li, Yuan Lei Zhang, and Chao Jing. An indirect approach based on Clausius-Clapeyron equation to determine entropy change for the first-order magnetocaloric materials. *Physics Letters, Section A: General, Atomic and Solid State Physics*, 379(47-48):3149–3154, 2015.

[51] A. Giguère, M. Foldeaki, B. Ravi Gopal, R. Chahine, T. K. Bose, A. Frydman, and J. A. Barclay. Direct Measurement of the "Giant" Adiabatic Temperature Change in Gd5Si2Ge2. *Physical Review Letters*, 83(11):2262–2265, sep 1999.

[52] Fèlix Casanova, Xavier Batlle, Amílcar Labarta, Jordi Marcos, Lluís Mañosa, and Antoni Planes. Change in entropy at a first-order magnetoelastic phase transition: Case study of Gd5(SixGe1-x)4giant magnetocaloric alloys. *Journal of Applied Physics*, 93(10 3):8313–8315, 2003.

[53] Lluís Mañosa, Antoni Planes, and Xavier Moya. Comment on "The Magnetocaloric Effect of LaFe 11.6 Si 1.4 , La 0.8 Nd 0.2 Fe 11.5 Si 1.5 , and Ni 43 Mn 46 Sn 11 Compounds in the Vicinity of the First-Order Phase Transition". *Advanced Materials*, 21(37):3725–3726, jul 2009.

[54] L. Caron, Z. Q. Ou, T. T. Nguyen, D. T. Cam Thanh, O. Tegus, and E. Brück. On the determination of the magnetic entropy change in materials with first-order transitions. *Journal of Magnetism and Magnetic Materials*, 321(21):3559–3566, 2009.

[55] Victorino Franco. Determination of the Magnetic Entropy Change from Magnetic Measurements : the Importance of the Measurement Protocol. pages 1–19, 2014.

[56] Anja Waske, Biswanath Dutta, Niclas Teichert, Bruno Weise, Navid Shayanfar, Andreas Becker, Andreas Hütten, and Tilmann Hickel. Coupling Phenomena in Magnetocaloric Materials. *Energy Technology*, 6(8):1429–1447, 2018.

[57] M.E. Wood and W.H. Potter. General analysis of magnetic refrigeration and its optimization using a new concept: maximization of refrigerant capacity. *Cryogenics*, 25(12):667–683, dec 1985.

[58] K. A. Gschneidner and V. K. Pecharsky. Magnetocaloric Materials. *Annual Review of Materials Science*, 30(1):387–429, aug 2000.

[59] N. H. Dung, L. Zhang, Z. Q. Ou, and E. Brck. From first-order magneto-elastic to magneto-structural transition in (Mn,Fe)1.95P0.50Si0.50 compounds. *Applied Physics Letters*, 99(9):1–4, 2011.

[60] V. Franco, J.S. Blázquez, J.J. Ipus, J.Y. Law, L.M. Moreno-Ramírez, and A. Conde. Magnetocaloric effect: From materials research to refrigeration devices. *Progress in Materials Science*, 93:112–232, apr 2018.

[61] Friedrich Heusler. Über magnetische Manganlegierungen. *Verhandlungen der Deutschen physikalischen Gesellschaft*, page 219, 1903.

[62] Friedrich Heusler, W Starck, and E Haupt. Über die Synthese ferromagnetischer Manganlegierungen. *Verhandlungen der Deutschen physikalischen Gesellschaft*, pages 220–223, 1903.

[63] W. Starck and E. Haupt. Über die magnetischen Eigenschaften von eisenfreien Manganlegierungen. *Verhandlungen der Deutschen physikalischen Gesellschaft*, 5:224–232, 1903.

[64] Tanja Graf, Claudia Felser, and Stuart S.P. Parkin. Simple rules for the understanding of Heusler compounds. *Progress in Solid State Chemistry*, 39(1):1–50, 2011.

[65] Subhradip Ghosh and Biplab Sanyal. Complex magnetic interactions in off-stoichiometric NiMnGa alloys. *Journal of Physics Condensed Matter*, 22(34), 2010.

[66] Peter Entel, V D Buchelnikov, V V Khovailo, A T Zayak, W A Adeagbo, M E Gruner, H C Herper, and E F Wassermann. Modelling the phase diagram of magnetic shape memory Heusler alloys. *Journal of Physics D: Applied Physics*, 39(5):865–889, 2006.

[67] J. Pons, R. Santamarta, V. A. Chernenko, and E. Cesari. Long-period martensitic structures of Ni-Mn-Ga alloys studied by high-resolution transmission electron microscopy. *Journal of Applied Physics*, 97:083516, 2005.

[68] R. Santamarta, E. Cesari, J. Muntasell, J. Font, J. Pons, and P. Ochin. Thermal and microstructural evolution under ageing of several high-temperature Ni-Mn-Ga alloys. *Intermetallics*, 18(5):977–983, 2010.

[69] J. Pons, V.A. Chernenko, R. Santamarta, and E. Cesari. Crystal structure of martensitic phases in Ni–Mn–Ga shape memory alloys. *Acta Materialia*, 48:3027–3038, 2000.

[70] M. Richard, J. Feuchtwanger, D. Schlagel, T. Lograsso, S.M. Allen, and R.C. O'Handley. Crystal structure and transformation behavior of Ni–Mn–Ga martensites. *Scripta Materialia*, 54(10):1797–1801, 2006.

[71] N. Lanska. Composition and temperature dependence of the crystal structure of Ni–Mn–Ga alloys. *Journal of Applied Physics*, 95(12):8074, 2004.

[72] M. Chmielus, K. Rolfs, R. Wimpory, W. Reimers, P. Müllner, and R. Schneider. Effects of surface roughness and training on the twinning stress of Ni–Mn–Ga single crystals. *Acta Materialia*, 58(11):3952–3962, 2010.

[73] Yan Xin and Ying Zhou. Martensitic transformation and mechanical properties of Ni Mn Ga V high-temperature shape memory alloys. *Intermetallics*, 73:50–57, jun 2016.

[74] Morris Cohen. Martensitic Transformations in Materials Science and Engineering. *Transactions of the Japan Institute of Metals*, 29(8):609–624, 1988.

[75] P. Müllner and G. Kostorz. Microstructure of Magnetic Shape-Memory Alloys: Between Magnetoelasticity and Magnetoplasticity. *Materials Science Forum*, 583:43–65, 2008.

[76] Markus Chmielus. *Composition, Structure and Magneto- Mechanical Properties of Ni-Mn-Ga Magnetic Shape-Memory Alloys.* Logos Verlag Berlin, Berlin, 1 edition, 2011.

[77] Vladimir Khovaylo. Inconvenient magnetocaloric effect in ferromagnetic shape memory alloys. *Journal of Alloys and Compounds*, 577(SUPPL. 1):S362–S366, 2013.

[78] Tino Gottschall, Konstantin P. Skokov, Bianca Frincu, and Oliver Gutfleisch. Large reversible magnetocaloric effect in Ni-Mn-In-Co. *Applied Physics Letters*, 106(2), 2015.

[79] Tino Gottschall, Enric Stern-Taulats, Lluís Mañosa, Antoni Planes, Konstantin P. Skokov, and Oliver Gutfleisch. Reversibility of minor hysteresis loops in magnetocaloric Heusler alloys. *Applied Physics Letters*, 110(22), 2017.

[80] Thorsten Krenke, Eyüp Duman, Mehmet Acet, Eberhard F Wassermann, Xavier Moya, Lluis Mañosa, and Antoni Planes. Inverse magnetocaloric effect in ferromagnetic Ni-Mn-Sn alloys. *Nature materials*, 4(6):450–454, 2005.

[81] Z D Han, D H Wang, C L Zhang, H C Xuan, B X Gu, and Y W Du. Low-field inverse magnetocaloric effect in Ni50-x Mn 39+x Sn11 Heusler alloys. *Applied Physics Letters*, 90(4):8–11, 2007.

[82] H. C. Xuan, L. J. Shen, T. Tang, Q. Q. Cao, D. H. Wang, and Y. W. Du. Magnetic-field-induced reverse martensitic transformation and large magnetoresistance in Ni 50-xCo xMn 32Al 18 Heusler alloys. *Applied Physics Letters*, 100(17), 2012.

[83] Thorsten Krenke, Eyüp Duman, Mehmet Acet, Xavier Moya, Lluís Mañosa, and Antoni Planes. Effect of Co and Fe on the inverse magnetocaloric properties of Ni-Mn-Sn. *Journal of Applied Physics*, 102(3):1–6, 2007.

[84] H S Liu, C L Zhang, Z D Han, H C Xuan, D H Wang, and Y W Du. The effect of Co doping on the magnetic entropy changes in Ni44-xCoxMn45Sn11 alloys. *Journal of Alloys and Compounds*, 467(1-2):27–30, 2009.

[85] Vijay Srivastava, Xian Chen, and Richard D James. Hysteresis and unusual magnetic properties in the singular Heusler alloy Ni45 Co5 Mn40 Sn10. *Applied Physics Letters*, 97(1):1–4, 2010.

[86] Nickolaus M. Bruno, Cengiz Yegin, Ibrahim Karaman, Jing-Han Chen, Joseph H. Ross, Jian Liu, and Jianguo Li. The effect of heat treatments on Ni43Mn42Co4Sn11

meta-magnetic shape memory alloys for magnetic refrigeration. *Acta Materialia*, 74:66–84, 2014.

[87] M Kataoka, K Endo, N Kudo, T Kanomata, H Nishihara, T Shishido, R Y Umetsu, M Nagasako, and R Kainuma. Martensitic transition, ferromagnetic transition, and their interplay in the shape memory alloys Ni2Mn1-xCuxGa. *Physical Review B - Condensed Matter and Materials Physics*, 82(21):1–14, 2010.

[88] Shane Stadler, Mahmud Khan, Joseph Mitchell, Naushad Ali, Angelo M. Gomes, Igor Dubenko, Armando Y. Takeuchi, and Alberto P. Guimarães. Magnetocaloric properties of Ni 2Mn1-xCuxGa. *Applied Physics Letters*, 88(19), 2006.

[89] Bhoj Raj Gautam, Igor Dubenko, James C Mabon, Shane Stadler, and Naushad Ali. Effect of small changes in Mn concentration on phase transition temperatures and magnetic entropy variations in Ni2Mn0.75Cu0.25Ga Heusler alloys. *Journal of Alloys and Compounds*, 472(1-2):35–39, 2009.

[90] Mahmud Khan, Shane Stadler, and Naushad Ali. Magnetocaloric properties of Fe and Ge doped Ni2 Mn1-x Cux Ga. In *Journal of Applied Physics*, volume 101, 2007.

[91] Sudip Kumar Sarkar, Sarita, P.D. Babu, Aniruddha Biswas, Vasudeva Siruguri, and Madangopal Krishnan. Giant magnetocaloric effect from reverse martensitic transformation in Ni–Mn–Ga–Cu ferromagnetic shape memory alloys. *Journal of Alloys and Compounds*, 670:281–288, 2016.

[92] Pan-Pan Li, Jing-Min Wang, and Cheng-Bao Jiang. Martensitic transformation in Cu-doped NiMnGa magnetic shape memory alloys. *Chinese Physics B*, 20(2):028104, 2011.

[93] Concepcio Seguí, Joan Torrens-Serra, Eduard Cesari, and Patricia Lázpita. Optimizing the Caloric Properties of Cu-Doped Ni–Mn–Ga Alloys. *Materials*, 13(2):419, 2020.

[94] Ian Gibson, David W. Rosen, and Brent Stucker. *Additive Manufacturing Technologies*. Springer US, Boston, MA, 2010.

[95] Stephen Mellor, Liang Hao, and David Zhang. Additive manufacturing: A framework for implementation. *International Journal of Production Economics*, 149:194–201, 2014.

[96] Simon Ford and Mélanie Despeisse. Additive manufacturing and sustainability: an exploratory study of the advantages and challenges. *Journal of Cleaner Production*, 137:1573–1587, 2016.

[97] Mohsen Attaran. The rise of 3-D printing: The advantages of additive manufacturing over traditional manufacturing. *Business Horizons*, 60(5):677–688, 2017.

[98] Amit Bandyopadhyay, B V Krishna, Weichang Xue, and Susmita Bose. Application of laser engineered net shaping (LENS) to manufacture porous and functionally graded structures for load bearing implants. *Journal of Materials Science: Materials in Medicine*, 20 Suppl 1:S29–S34, 2009.

[99] Linkan Bian, Scott M. Thompson, and Nima Shamsaei. Mechanical Properties and Microstructural Features of Direct Laser-Deposited Ti-6Al-4V. *Jom*, 67(3):629–638, 2015.

[100] V. D. Manvatkar, a. a. Gokhale, G. Jagan Reddy, a. Venkataramana, and a. De. Estimation of melt pool dimensions, thermal cycle, and hardness distribution in the laser-engineered net shaping process of austenitic stainless steel. *Metallurgical and Materials Transactions A: Physical Metallurgy and Materials Science*, 42:4080–4087, 2011.

[101] Erica L Stevens, Jakub Toman, Albert C To, and Markus Chmielus. Variation of hardness, microstructure, and Laves phase distribution in direct laser deposited alloy 718 cuboids. *Materials & Design*, 119:188–198, 2017.

[102] Amir Mostafaei, Amy M. Elliott, John E. Barnes, Corson L. Cramer, Peeyush Nandwana, and Markus Chmielus. Binder jet 3D printing – process parameters, materials, properties, and challenges. *Progress in Materials Science*, page 100684, 2020.

[103] Randall German. *Sintering: from Empirical Observations to Scientific Principles.* Elsevier Science & Technology, Saint Louis, MO, 2014.

[104] Randall M German. Coordination number changes during powder densification. *Powder Technology*, 253:368–376, 2014.

[105] Gaku Okuma, Daiki Kadowaki, Tsuyoshi Hondo, Akihiro Sato, Satoshi Tanaka, and Fumihiro Wakai. Computation of sintering stress and bulk viscosity from microtomographic images in viscous sintering of glass particles. *Journal of the American Ceramic Society*, 100(3):867–875, 2017.

[106] H. E. Exner and E. Arzt. Sintering Processes. In R.W. Cahn and P. Haasen, editors, *Physical Metallurgy*, chapter 31, pages 157–184. Elsevier Science B.V., 4 edition, 1996.

[107] Fumihiro Wakai, Dmitri V. Louzguine-Luzgin, and Toshio Kuroda. A microscopic model of interface-reaction-controlled sintering of spherical particles of different phases. *Journal of the American Ceramic Society*, 92(8):1663–1671, 2009.

[108] Ricardo H.R. Castro and Douglas Gouvêa. Sintering and Nanostability: The Thermodynamic Perspective. *Journal of the American Ceramic Society*, 99(4):1105–1121, 2016.

[109] F. Wakai and K. A. Brakke. Tensor virial equation of evolving surfaces in sintering of aggregates of particles by diffusion. *Acta Materialia*, 61(11):4103–4112, 2013.

[110] Fumihiro Wakai, Olivier Guillon, Gaku Okuma, and Norimasa Nishiyama. Sintering forces acting among particles during sintering by grain-boundary/surface diffusion. *Journal of the American Ceramic Society*, 102(2):38–43, 2018.

[111] Amir Mostafaei, Pierangeli Rodriguez De Vecchis, Ian Nettleship, Markus Chmielus, Pierangeli Rodriguez De Vecchis, Ian Nettleship, and Markus Chmielus. Effect of powder size distribution on densification and microstructural evolution of binder-jet 3D-printed alloy 625. *Materials & Design*, 162:375–383, jan 2019.

[112] J D Moore, D Klemm, D Lindackers, S Grasemann, R Träger, and J Eckert. Selective laser melting of La (Fe , Co , Si) 13 geometries for magnetic refrigeration. *Journal of Applied Physics*, 114(4):1–9, 2013.

[113] Barbara Pulko, Jaka Tušek, James D. Moore, Bruno Weise, Konstantin Skokov, Oleg Mityashkin, Andrej Kitanovski, Chiara Favero, Peter Fajfar, Oliver Gutfleisch, Anja Waske, and Alojz Poredoš. Epoxy-bonded La-Fe-Co-Si magnetocaloric plates. *Journal of Magnetism and Magnetic Materials*, 375:65–73, 2015.

[114] J. L. Sánchez Llamazares, P. Ibarra-Gaytán, C. F. Sánchez-Valdés, P. Álvarez-Alonso, and A. D. Martínez-Iniesta. Synthesis and magnetocaloric characterization of rapidly solidified ErMn2melt-spun ribbons. *Intermetallics*, 88(April):41–45, 2017.

[115] J. L. Sánchez Llamazares, P. Ibarra-Gaytán, C. F. Sánchez-Valdés, Pablo Álvarez-Alonso, and R. Varga. Enhanced magnetocaloric effect in rapidly solidified HoNi2melt-spun ribbons. *Journal of Alloys and Compounds*, 774:700–705, 2019.

[116] N. M. Bruno, Y. J. Huang, C. L. Dennis, J. G. Li, R. D. Shull, J. H. Ross, Y. I. Chumlyakov, and I. Karaman. Effect of grain constraint on the field requirements for magnetocaloric effect in Ni45Co5Mn40Sn10melt-spun ribbons. *Journal of Applied Physics*, 120(7), 2016.

[117] A. M. Aliev, A. B. Batdalov, I. K. Kamilov, V. V. Koledov, V. G. Shavrov, V. D. Buchelnikov, J. Garcia, V. M. Prida, and B. Hernando. Magnetocaloric effect in ribbon samples of Heusler alloys Ni-Mn-M (M=In,Sn). *Applied Physics Letters*, 97(21):35–38, 2010.

[118] Naifu Zou, Zongbin Li, Yudong Zhang, C.F. Sánchez-Valdés, J.L. Sánchez Llamazares, Claude Esling, Bo Yang, Xiang Zhao, and Liang Zuo. Transformation process dependent magnetocaloric properties of annealed Ni 50 Mn 18 Cu 7 Ga 25 ribbons. *Journal of Alloys and Compounds*, 698:731–738, mar 2017.

[119] Jian Yang, Yanyan Shao, Zaixin Feng, and Jian Liu. The effect of cooling rate on the phase formation and magnetocaloric properties in La0.6Ce0.4Fe11.0Si2.0alloys. *Journal of Magnetism and Magnetic Materials*, 452:473–476, 2018.

[120] J. J. Liu, Y. Zhang, J. Zhang, W. X. Xia, J. Du, and A. R. Yan. Systematic study of the microstructure and magnetocaloric effect of bulk and melt-spun ribbons of La-Pr-Fe-Si compounds. *Journal of Magnetism and Magnetic Materials*, 350:94–99, 2014.

[121] J. S. Blázquez, J J Ipus, L. M. Moreno-Ramírez, J. M. Álvarez-Gómez, D. Sánchez-Jiménez, S. Lozano-Pérez, V Franco, and A Conde. Ball milling as a way to produce magnetic and magnetocaloric materials: a review. *Journal of Materials Science*, 52(20):11834–11850, 2017.

[122] C Aprea, A Greco, A Maiorino, and C Masselli. A two-dimensional investigation about magnetocaloric regenerator design: parallel plates or packed bed? *Journal of Physics: Conference Series*, 796(1):012018, jan 2017.

[123] H. Sepehri-Amin, A. Taubel, T. Ohkubo, K. P. Skokov, O. Gutfleisch, and K. Hono. Microstructural origin of hysteresis in Ni-Mn-In based magnetocaloric compounds. *Acta Materialia*, 147:342–349, 2018.

[124] Ryan A. Booth and Sara A. Majetich. The magnetocaloric effect in thermally cycled polycrystalline Ni-Mn-Ga. *Journal of Applied Physics*, 111(7):1–4, 2012.

[125] Jian Liu, Pengna Zhang, Fuping Dai, and Aru Yan. A new approach to prepare spherical La–Fe–Si–Co magnetocaloric refrigerant particles. *Scripta Materialia*, 69(6):485–488, sep 2013.

[126] Pengna Zhang, Jian Liu, Yanyan Shao, and Aru Yan. Direct formation of NaZn 13 - structure La(Fe,Si) 13 phase by directional solidification. *Materials Letters*, 193:34–37, apr 2017.

[127] Julia Lyubina, Oliver Gutfleisch, Michael D. Kuz'min, and Manuel Richter. La(Fe,Si)13-based magnetic refrigerants obtained by novel processing routes. *Journal of Magnetism and Magnetic Materials*, 320(18):2252–2258, 2008.

[128] J. W. Lai, Z. G. Zheng, B. W. Huang, H. Y. Yu, Z. G. Qiu, Y. L. Mao, S. Zhang, F. M. Xiao, D. C. Zeng, K. Goubitz, and E. Brück. Microstructure formation and magnetocaloric effect of the Fe2P-type phase in (Mn,Fe)2(P, Si, B) alloys. *Journal of Alloys and Compounds*, 735:2567–2573, 2018.

[129] Xue Fei Miao, Hossein Sepehri-Amin, and Kazuhiro Hono. Structural origin of hysteresis for hexagonal (Mn,Fe)2(P,Si) magneto-caloric compound. *Scripta Materialia*, 138:96–99, 2017.

[130] T. B. Zhang, V. Provenzano, Y. G. Chen, and R. D. Shull. Magnetic properties of a high energy ball-milled amorphous Gd5Si1.8Ge1.8Sn0.4 alloy. *Solid State Communications*, 147(3-4):107–110, 2008.

[131] B. Chevalier, J. L. Bobet, J. Sánchez Marcos, J. Rodriguez Fernandez, and J. C.Gómez Sal. Magnetocaloric properties of amorphous GdNiAl obtained by mechanical grinding. *Applied Physics A: Materials Science and Processing*, 80(3):601–606, 2005.

[132] A. Rowe and A. Tura. Experimental investigation of a three-material layered active magnetic regenerator. *International Journal of Refrigeration*, 29(8):1286–1293, 2006.

[133] Wojciech Maziarz, Anna Wójcik, Paweł Czaja, Antoni Żywczak, Jan Dutkiewicz, Łukasz Hawełek, and Eduard Cesari. Magneto-structural transformations in Ni50Mn37.5Sn12.5-xInx Heusler powders. *Journal of Magnetism and Magnetic Materials*, 412:123–131, aug 2016.

[134] Heng Zhang, Jian Liu, Mingxiao Zhang, Yanyan Shao, Yang Li, and Aru Yan. LaFe11.6Si1.4Hy/Sn magnetocaloric composites by hot pressing. *Scripta Materialia*, 120:58–61, jul 2016.

[135] M.X. Zhang, J. Liu, Y. Zhang, J.D. Dong, A.R. Yan, K.P. Skokov, and O. Gutfleisch. Large entropy change, adiabatic temperature change, and small hysteresis in La(Fe,Mn)11.6Si1.4 strip-cast flakes. *Journal of Magnetism and Magnetic Materials*, 377:90–94, mar 2015.

[136] A. Ghotbi Varzaneh, P. Kameli, F. Karimzadeh, B. Aslibeiki, G. Varvaro, and H. Salamati. Magnetocaloric effect in Ni47Mn40Sn13 alloy prepared by mechanical alloying. *Journal of Alloys and Compounds*, 598:6–10, 2014.

[137] Edyta Matyja, Krystian Prusik, Maciej Zubko, Grzegorz Dercz, and Karsten Glowka. Structure of the Ni-Co-Mn-In alloy obtained by mechanical alloying and sintering. *Journal of Alloys and Compounds*, 801:529–535, sep 2019.

[138] A. L. Alves, E. C. Passamani, V. P. Nascimento, A. Y. Takeuchi, and C. Larica. Influence of grain refinement and induced crystal defects on the magnetic properties of Ni50Mn36Sn14 Heusler alloy. *Journal of Physics D: Applied Physics*, 43(34), 2010.

[139] Erica Stevens, Katerina Kimes, Volodymyr Chernenko, Patricia Lázpita, Anna Wojcik, Wojciech Maziarz, Jakub Toman, and Markus Chmielus. Effect of Homogenization on the Microstructure and Magnetic Properties of Direct Laser-Deposited Magnetocaloric Ni43Co7Mn39Sn11. *Journal of Manufacturing Science and Engineering*, 142(7):1–8, 2020.

[140] Nguyen van Thang, Niels Harmen van Dijk, and Ekkes Brück. Tuneable giant magnetocaloric effect in (Mn,Fe)2(P,Si) materials by Co-B and Ni-B co-doping. *Materials*, 10(1), 2017.

[141] A. Bartok, M. Kustov, L. F. Cohen, A. Pasko, K. Zehani, L. Bessais, F. Mazaleyrat, and M. Lobue. Study of the first paramagnetic to ferromagnetic transition in as prepared samples of Mn-Fe-P-Si magnetocaloric compounds prepared by different synthesis routes. *Journal of Magnetism and Magnetic Materials*, 400:333–338, 2016.

[142] S. Kavita, G. Anusha, Pramod Bhatt, V. Suresh, R. Vijay, K. Sethupathi, and R. Gopalan. On the giant magnetocaloric and mechanical properties of Mn–Fe–P–Si-Ge alloy. *Journal of Alloys and Compounds*, 817:153232, 2020.

[143] Xuefei Miao, Wenyao Wang, Huixin Liang, Fengjiao Qian, Mengqi Cong, Yujing Zhang, Amir Muhammad, Zongjun Tian, and Feng Xu. Printing (Mn,Fe)2(P,Si) magnetocaloric alloys for magnetic refrigeration applications. *Journal of Materials Science*, 55(15):6660–6668, 2020.

[144] F. Nilsén, I. Aaltio, Y. Ge, T. Lindroos, and S. P. Hannula. Characterization of Gas Atomized Ni-Mn-Ga Powders. *Materials Today: Proceedings*, 2:S879–S882, 2015.

[145] Frans Nilsén, Joonas Lehtonen, Yanling Ge, Ilkka Aaltio, and Simo Pekka Hannula. Highly porous spark plasma sintered Ni-Mn-Ga structures. *Scripta Materialia*, 139:148–151, 2017.

[146] Frans Nilsén, Iñigo Flores Ituarte, Mika Salmi, Jouni Partanen, and Simo Pekka Hannula. Effect of process parameters on non-modulated Ni-Mn-Ga alloy manufactured using powder bed fusion. *Additive Manufacturing*, 28(May):464–474, 2019.

[147] Kouhei Ito, Wataru Ito, Rie Y. Umetsu, Makoto Nagasako, Ryosuke Kainuma, Asaya Fujita, Katsunari Oikawa, and Kiyohito Ishida. Martensitic Transformation in NiCoMnSn Metamagnetic Shape Memory Alloy Powders. *Materials Transactions*, 49(8):1915–1918, 2008.

[148] Kouhei Ito, Wataru Ito, Rie Y. Umetsu, Ibrahim Karaman, Kiyohito Ishida, and Ryosuke Kainuma. Metamagnetic Shape Memory Effect in Porous Ni43Co7Mn39Sn11 Alloy Compacts Fabricated by Pressureless Sintering. *Materials Transactions*, 52(12):2270–2273, 2011.

[149] Sandra Wieland and Frank Petzoldt. Powder-extrusion and sintering of magnetocaloric LaCe(FeMnSi)13 alloy. *Journal of Alloys and Compounds*, 719:182–188, sep 2017.

[150] Jwalant Kagathara, Sandra Wieland, Eric Gärtner, Volker Uhlenwinkel, and Matthias Steinbacher. Heat treatment and formation of magnetocaloric 1: 13 phase in LaFe11.4Si1.2Co0.4 processed by laser beam melting. *Materials*, 13(3):1–10, 2020.

[151] W. Maziarz, A. Wójcik, J. Grzegorek, A. Żywczak, P. Czaja, M. J. Szczerba, J. Dutkiewicz, and E. Cesari. Microstructure, magneto-structural transformations and mechanical properties of Ni50Mn37.5Sn12.5-xInx(x=0, 2, 4, 6 % at.) metamagnetic shape memory alloys sintered by vacuum hot pressing. *Journal of Alloys and Compounds*, 715:445–453, 2017.

[152] Matthias Katter, Volker Zellmann, Georg Werner Reppel, and Kaan Uestuener. Magnetocaloric properties of La(Fe, Co, Si) 13 bulk material prepared by powder metallurgy. *IEEE Transactions on Magnetics*, 44(11 PART 2):3044–3047, 2008.

[153] X. C. Zhong, X. L. Feng, X. W. Huang, X. Y. Shen, and Z. W. Liu. Structure and magnetocaloric effect of La0.7Ce0.3(Fe0.92Co0.08)11.4Si1.6bulk alloy prepared by powder metallurgy. *Journal of Alloys and Compounds*, 685:913–916, 2016.

[154] Britt Rosendahl Hansen, L. Theil Kuhn, C.R.H. Bahl, M. Lundberg, C. Ancona-Torres, and M. Katter. Properties of magnetocaloric La(Fe,Co,Si)13 produced by powder metallurgy. *Journal of Magnetism and Magnetic Materials*, 322(21):3447–3454, nov 2010.

[155] X.C. Zhong, X.L. Feng, X.W. Huang, X.Y. Shen, and Z.W. Liu. Structure and magnetocaloric effect of La 0.7 Ce 0.3 (Fe 0.92 Co 0.08) 11.4 Si 1.6 bulk alloy prepared by powder metallurgy. *Journal of Alloys and Compounds*, 685:913–916, nov 2016.

[156] J. Liu, J.D. Moore, K.P. Skokov, M. Krautz, K. Löwe, A. Barcza, M. Katter, and O. Gutfleisch. Exploring La(Fe,Si)13-based magnetic refrigerants towards application. *Scripta Materialia*, 67(6):584–589, sep 2012.

[157] Kristina Navickaitė, Henrique Neves Bez, Tian Lei, Alexander Barcza, Hugo Vieyra, Christian R.H. Bahl, and Kurt Engelbrecht. Experimental and numerical comparison of multi-layered La(Fe,Si,Mn)13Hy active magnetic regenerators. *International Journal of Refrigeration*, 86:322–330, 2018.

[158] Theodor Victor Christiaanse. *Characterization, Experimentation and Modeling of Mn-Fe-Si-P Magnetocaloric Materials*. PhD thesis, University of Victoria, 2018.

[159] Alexander Funk, Michael Zeilinger, Anja Miehe, Daniel Sopu, Jürgen Eckert, Florian Dötz, and Anja Waske. MnFePSi-based magnetocaloric packed bed regenerators: Structural details probed by X-ray tomography. *Chemical Engineering Science*, 175:84–90, jan 2018.

[160] Jaime A. Lozano, Matheus S. Capovilla, Paulo V. Trevizoli, Kurt Engelbrecht, Christian R.H. Bahl, and Jader R. Barbosa. Development of a novel rotary magnetic refrigerator. *International Journal of Refrigeration*, 68:187–197, aug 2016.

[161] Michael A. Benedict, S. A. Sherif, David G. Beers, and Michael G. Schroeder. Design and performance of a novel magnetocaloric heat pump. *Science and Technology for the Built Environment*, 22(5):520–526, jul 2016.

[162] Inmyong Park, Youngkwon Kim, and Sangkwon Jeong. Development of the tandem reciprocating magnetic regenerative refrigerator and numerical simulation for the dead volume effect. *International Journal of Refrigeration*, 36(6):1741–1749, sep 2013.

[163] S. Taskaev, V. Khovaylo, D. Karpenkov, I. Radulov, M. Ulyanov, D. Bataev, A. Dyakonov, D. Gunderov, K. Skokov, and O. Gutfleisch. Plastically deformed Gd-X (X = Y, In, Zr, Ga, B) solid solutions for magnetocaloric regenerator of parallel plate geometry. *Journal of Alloys and Compounds*, 754:207–214, 2018.

[164] M. A. Richard, A. M. Rowe, and R. Chahine. Magnetic refrigeration: Single and multimaterial active magnetic regenerator experiments. *Journal of Applied Physics*, 95(4):2146–2150, 2004.

[165] Reed Teyber, Jamelyn Holladay, Kerry Meinhardt, Evgueni Polikarpov, Edwin Thomsen, Jun Cui, Andrew Rowe, and John Barclay. Performance investigation of a high-field active magnetic regenerator. *Applied Energy*, 236(December 2018):426–436, feb 2019.

[166] Mohammadreza Ghahremani. *Magnetocaloric Materials and Magnetic Refrigeration Systems*. PhD thesis, The George Washington University, 2014.

[167] K. Engelbrecht, C.R.H. Bahl, and K.K. Nielsen. Experimental results for a magnetic refrigerator using three different types of magnetocaloric material regenerators. *International Journal of Refrigeration*, 34(4):1132–1140, jun 2011.

[168] R. Kolano, A. Kolano-Burian, M. Hreczka, M. Polak, J. Szynowski, and W. Tomaka. Magnetocaloric cooling device with reciprocating motion of the magnetic field source. *Acta Physica Polonica A*, 129(6):1205–1209, 2016.

[169] J. Romero Gómez, R. Ferreiro Garcia, J. Carbia Carril, and M. Romero Gómez. Experimental analysis of a reciprocating magnetic refrigeration prototype. *International Journal of Refrigeration*, 36(4):1388–1398, jun 2013.

[170] X.N. He, M.Q. Gong, H. Zhang, W. Dai, J. Shen, and J.F. Wu. Design and performance of a room-temperature hybrid magnetic refrigerator combined with Stirling gas refrigeration effect. *International Journal of Refrigeration*, 36(5):1465–1471, aug 2013.

[171] J. Kaštil, J. Tětek, and A. Tuček. Experimental Investigation of Small-Scale Magnetocaloric Refrigerator. *Acta Physica Polonica A*, 124(4):740–744, oct 2013.

[172] Theo Christiaanse and Ekkes Brück. Proof-of-Concept Static Thermomagnetic Generator Experimental Device. *Metallurgical and Materials Transactions E*, 1(1):36–40, 2014.

[173] A. Sarlah, A. Kitanovski, A. Poredos, P. W. Egolf, O. Sari, F. Gendre, and Ch Besson. Static and rotating active magnetic regenerators with porous heat exchangers for magnetic cooling. *International Journal of Refrigeration*, 29(8):1332–1339, 2006.

[174] E. A. Périgo, J. Jacimovic, F. García Ferré, and L. M. Scherf. Additive manufacturing of magnetic materials. *Additive Manufacturing*, 30(August):100870, 2019.

[175] P.V. Trevizoli, R. Teyber, P.S. da Silveira, F. Scharf, S.M. Schillo, I. Niknia, P. Govindappa, T.V. Christiaanse, and A. Rowe. Thermal-hydraulic evaluation of 3D printed microstructures. *Applied Thermal Engineering*, 160(xxxx):113990, sep 2019.

[176] Neera Singh, Raghunandan Ummethala, Pearlin Hameed, Rathinavelu Sokkalingam, and Konda Gokuldoss Prashanth. Competition between densification and microstructure of functional materials by Selective Laser Melting. *Material Design & Processing Communications*, 2(3):1–7, jun 2020.

[177] V. Chaudhary, S. A. Mantri, R. V. Ramanujan, and R. Banerjee. Additive manufacturing of magnetic materials. *Progress in Materials Science*, 114(May):100688, 2020.

[178] Ville Laitinen, Mahdi Merabtene, Erica Stevens, Markus Chmielus, Jan Van Humbeeck, and Kari Ullakko. *Technical, Economic and Societal Effects of Manufacturing 4.0.* Springer International Publishing, Cham, 2020.

[179] Sandra Wieland, Jwalant Kagathara, Eric Gärtner, Volker Uhlenwinkel, and Matthias Steinbacher. Powder, process parameters and heat treatment conditions for Laser Beam Melting of LaFeSi-based alloys. In *8th International Conference on Caloric Cooling (Thermag VIII)*, pages 27–32, Darmstadt, Germany, 2018. International Institute of Refrigeration.

[180] S. Wieland, N. Goossense, C. Weck, and S.B. Hein. Additive manufacturing of metallic materials. In *EuroPM 2019*, pages 1–6, Maastricht, Netherlands, 2019. European Powder Metallurgy Association.

[181] Ville Laitinen, Antti Salminen, and Kari Ullakko. First investigation on processing parameters for laser powder bed fusion of Ni-Mn-Ga magnetic shape memory alloy. *Journal of Laser Applications*, 31(2):022303, may 2019.

[182] Ville Laitinen, Alexei Sozinov, Andrey Saren, Antti Salminen, and Kari Ullakko. Laser powder bed fusion of Ni-Mn-Ga magnetic shape memory alloy. *Additive Manufacturing*, 30(July):100891, dec 2019.

[183] Amir Mostafaei, Pierangeli Rodriguez De Vecchis, Erica L. Stevens, and Markus Chmielus. Sintering regimes and resulting microstructure and properties of binder jet 3D printed Ni-Mn-Ga magnetic shape memory alloys. *Acta Materialia*, 154:355–364, aug 2018.

[184] Amir Mostafaei, Katerina A. Kimes, Erica L. Stevens, Jakub Toman, Yuval L. Krimer, Kari Ullakko, and Markus Chmielus. Microstructural evolution and magnetic properties of binder jet additive manufactured Ni-Mn-Ga magnetic shape memory alloy foam. *Acta Materialia*, 131:482–490, jun 2017.

[185] Matthew P. Caputo, Ami E. Berkowitz, Andrew Armstrong, Peter Müllner, and C. Virgil Solomon. 4D printing of net shape parts made from Ni-Mn-Ga magnetic shape-memory alloys. *Additive Manufacturing*, 21(2010):579–588, may 2018.

[186] Shannon L. Taylor, Ramille N. Shah, and David C. Dunand. Ni-Mn-Ga micro-trusses via sintering of 3D-printed inks containing elemental powders. *Acta Materialia*, 143:20–29, 2018.

[187] Erica Stevens, Daniel Salazar, Katerina Kimes, Rafael Rodriguez de Vecchis, Volodymyr Chernenko, and Markus Chmielus. Additive Manufacturing of Ni-Mn-Cu-Ga: Influence of Sintering Temperature on Magnetocaloric Effect and Microstructure. *Microscopy and Microanalysis*, 25(S2):2578–2579, 2019.

[188] Erica Stevens, Katerina Kimes, Jeffrey Martin, and Markus Chmielus. Multi-Material Binder Jet Printing of Functional Ni-Mn-Ga Alloys. *Microscopy and Microanalysis*, pages 1–4, jul 2020.

[189] E. Stevens, K. Kimes, V. Chernenko, A. Wojcik, W. Maziarz, J. Toman, and M. Chmielus. Characterization of direct laser deposited magnetocaloric Ni-Co-Mn-Sn. *Materials Science and Technology Conference and Exhibition 2017, MS&T 2017*, 1(M):430–432, 2017.

[190] Erica L Stevens, Samantha Schloder, Eric Bono, David E Schmidt, and Markus Chmielus. Density variation in binder jetting 3D-printed and sintered Ti-6Al-4V. *Additive Manufacturing*, 22:746–752, aug 2018.

[191] Erica Stevens, Jakub Toman, Katarina Kimes, Volodymyr Chernenko, Anna Wojcik, and Markus Chmielus. Microstructural Evaluation of Magnetocaloric Ni-Co-Mn-Sn Produced by Directed Energy Deposition. *Microscopy and Microanalysis*, 22(Suppl 3):1774–1775, 2016.

[192] Jakub Toman, Peter Müllner, and Markus Chmielus. Properties of as-deposited and heat-treated Ni-Mn-Ga magnetic shape memory alloy processed by directed energy deposition. *Journal of Alloys and Compounds*, 752:455–463, jul 2018.

[193] K. Vallal Peruman, M. Mahendran, S. Seenithurai, R. Chokkalingam, R. K. Singh, and V. Chandrasekaran. Internal stress dependent structural transition in ferromagnetic Ni-Mn-Ga nanoparticles prepared by ball milling. *Journal of Physics and Chemistry of Solids*, 71(11):1540–1544, 2010.

[194] Pierre Hovington, Dominique Drouin, Raynald Gauvin, David C. Joy, and Neal Evans. CASINO: A new Monte Carlo code in C language for electron beam interactions - Part III: Stopping power at low energies. *Scanning*, 19(1):29–35, 1997.

[195] B.D. Cullity. *Elements of X-ray Diffraction.* Addison-Wesley Publishing Company, 1978.

[196] H. N. Southworth. Scanning Electron Microscopy and Microanalysis. In *Physicochemical Methods of Mineral Analysis*, pages 421–450. Springer US, Boston, MA, 1975.

[197] Johann Radon. Über die Bestimmung von Funktionen durch ihre Integralwerte längs gewisser Mannigfaltigkeiten. *Ber. über Verh. Königlich-Sächsischen Ges. Wiss. Leipzig*, 69:262–277, 1917.

[198] Hrvoje Lusic and Mark W. Grinstaff. X-ray-Computed Tomography Contrast Agents. *Chemical Reviews*, 113(3):1641–1666, mar 2013.

[199] Julia F. Barrett and Nicholas Keat. Artifacts in CT: Recognition and avoidance. *Radiographics*, 24(6):1679–1691, 2004.

[200] Yiannis Kyriakou, Daniel Prell, and Willi A. Kalender. Ring artifact correction for high-resolution micro CT. *Physics in Medicine and Biology*, 54(17), 2009.

[201] Miklós Kovács, Róbert Danyi, Miklós Erdélyi, Pál Fejérdy, and Csaba Dobó-Nagy. Distortional effect of beam-hardening artefacts on microCT: a simulation study based on an in vitro caries model. *Oral Surgery, Oral Medicine, Oral Pathology, Oral Radiology, and Endodontology*, 108(4):591–599, oct 2009.

[202] F. Edward Boas and Dominik Fleischmann. CT artifacts: Causes and reduction techniques. *Imaging in Medicine*, 4(2):229–240, 2012.

[203] W.E. Case and R.D. Harrington. Calibration of vibrating-sample magnetometers. *Journal of Research of the National Bureau of Standards, Section C: Engineering and Instrumentation*, 70C(4):255, 1966.

[204] Pavel Holba, Jaroslav Šesták, and David Sedmidubský. Heat Transfer and Phase Transition in DTA Experiments. In J. Šesták and P. Šimon, editors, *Thermal analysis of Micro, Nano- and Non-Crystalline Materials. Hot Topics in Thermal Analysis and Calorimetry*, volume 9, chapter 5, pages 99–133. Springer, Dordrecht, 2012.

[205] Stefan Mathias Sarge, Wolfgang Hemminger, and Günther W. H. Höhne. Part Two: Practice of Calorimetry. In *Calorimetry : Fundamentals, Instrumentation and Applications*, chapter 2, pages 123–270. John Wiley & Sons, Incorporated, 2 edition, 2014.

[206] Matthias Wagner. Differential Scanning Calorimetry. In *Thermal Analysis in Practice - Fundamental Aspects*, chapter 7, pages 67–142. Hanser Publishers, 2018.

[207] Caroline A. Schneider, Wayne S. Rasband, and Kevin W. Eliceiri. NIH Image to ImageJ: 25 years of image analysis. *Nature Methods*, 9(7):671–675, 2012.

[208] Curtis T. Rueden, Johannes Schindelin, Mark C. Hiner, Barry E. DeZonia, Alison E. Walter, Ellen T. Arena, and Kevin W. Eliceiri. ImageJ2: ImageJ for the next generation of scientific image data. *BMC Bioinformatics*, 18(1):1–26, 2017.

[209] Johannes Schindelin, Ignacio Arganda-Carreras, Erwin Frise, Verena Kaynig, Mark Longair, Tobias Pietzsch, Stephan Preibisch, Curtis Rueden, Stephan Saalfeld, Benjamin Schmid, Jean Yves Tinevez, Daniel James White, Volker Hartenstein, Kevin Eliceiri, Pavel Tomancak, and Albert Cardona. Fiji: An open-source platform for biological-image analysis. *Nature Methods*, 9(7):676–682, 2012.

[210] Melissa Linkert, Curtis T. Rueden, Chris Allan, Jean Marie Burel, Will Moore, Andrew Patterson, Brian Loranger, Josh Moore, Carlos Neves, Donald MacDonald, Alek-

sandra Tarkowska, Caitlin Sticco, Emma Hill, Mike Rossner, Kevin W. Eliceiri, and Jason R. Swedlow. Metadata matters: Access to image data in the real world. *Journal of Cell Biology*, 189(5):777–782, 2010.

[211] J. Rodriguez-Carvajal. Fullprof: A Program for Rietveld Refinement and Pattern Matching Analysis. In *Abstract of the Satellite Meeting on Powder Diffraction of the XV Congress of the IUCr*, page 127, Toulouse, France, 1990.

[212] T. Roisnel and Juan Rodríquez-Carvajal. WinPLOTR: A Windows Tool for Powder Diffraction Pattern Analysis. *Materials Science Forum*, 378-381:118–123, oct 2001.

[213] R.C. Wimpory, P. Mikula, Jan Šaroun, T. Poeste, Junhong Li, M. Hofmann, and R. Schneider. Efficiency Boost of the Materials Science Diffractometer E3 at BENSC: One Order of Magnitude Due to a Horizontally and Vertically Focusing Monochromator. *Neutron News*, 19(1):16–19, jan 2008.

[214] Mirko Boin and Robert C. Wimpory. E3: Residual Stress Neutron Diffractometer at BER II. *Journal of large-scale research facilities JLSRF*, 2:A100, dec 2016.

[215] C. Randau, U. Garbe, and H.-G. Brokmeier. StressTextureCalculator : a software tool to extract texture, strain and microstructure information from area-detector measurements. *Journal of Applied Crystallography*, 44(3):641–646, jun 2011.

[216] D D Gu, W Meiners, K Wissenbach, and R Poprawe. Laser additive manufacturing of metallic components: materials, processes and mechanisms. *International Materials Reviews*, 57(3):133–164, may 2012.

[217] Yasuhiro Kakinuma, Masahiko Mori, Yohei Oda, Takanori Mori, Makoto Kashihara, Adam Hansel, and Makoto Fujishima. Influence of metal powder characteristics on product quality with directed energy deposition of Inconel 625. *CIRP Annals - Manufacturing Technology*, 65(1):209–212, 2016.

[218] Zhongkai Guo, Jinchuan Jie, Shichao Liu, Jiaming Liu, Shipeng Yue, Yubo Zhang, and Tingju Li. Solidification Characteristics and Segregation Behavior of Cu-15Ni-8Sn Alloy. *Metallurgical and Materials Transactions A: Physical Metallurgy and Materials Science*, 51(3):1229–1241, 2020.

[219] Jianyi Li, Qian Wang, and Panagiotis Michaleris. An analytical computation of temperature field evolved in directed energy deposition. *Journal of Manufacturing Science and Engineering, Transactions of the ASME*, 140(10), 2018.

[220] A.M. Pérez-Sierra, J. Pons, R. Santamarta, P. Vermaut, and P. Ochin. Solidification process and effect of thermal treatments on Ni–Co–Mn–Sn metamagnetic shape memory alloys. *Acta Materialia*, 93:164–174, jul 2015.

[221] P. Lázpita, M. Sasmaz, E. Cesari, J.M. Barandiarán, J. Gutiérrez, and V.A. Chernenko. Martensitic transformation and magnetic field induced effects in Ni42Co8Mn39Sn11 metamagnetic shape memory alloy. *Acta Materialia*, 109:170–176, may 2016.

[222] F. Chen, Y. X. Tong, Y. J. Huang, B. Tian, L. Li, and Y. F. Zheng. Suppression of γ phase in Ni 38 Co 12 Mn 41 Sn 9 alloy by melt spinning and its effect on martensitic transformation and magnetic properties. *Intermetallics*, 36:81–85, 2013.

[223] D. Y. Cong, S. Roth, and L. Schultz. Magnetic properties and structural transformations in Ni-Co-Mn-Sn multifunctional alloys. *Acta Materialia*, 60(13-14):5335–5351, 2012.

[224] P. Lázpita, J.M. Barandiarán, V.A. Chernenko, B. Valle García, E. Díaz Tajada, T. Lograsso, and D.L. Schlagel. Magnetic properties of Ni40+xMn39-xSn21 (x=0, 2, 4, 6 and 8at.%) Heusler alloys. *Journal of Alloys and Compounds*, 594:171–174, may 2014.

[225] J. Svoboda, H. Riedel, and H. Zipse. Equilibrium pore surfaces, sintering stresses and constitutive equations for the intermediate and late stages of sintering—I. computation of equilibrium surfaces. *Acta Metallurgica et Materialia*, 42(2):435–443, feb 1994.

[226] S. Roy, E. Blackburn, S. M. Valvidares, M. R. Fitzsimmons, S. C. Vogel, M. Khan, I. Dubenko, S. Stadler, N. Ali, S. K. Sinha, and J. B. Kortright. Delocalization and hybridization enhance the magnetocaloric effect in Cu-doped Ni2 MnGa. *Physical Review B - Condensed Matter and Materials Physics*, 79(23):1–5, 2009.

[227] R. Bjørk, C. R H Bahl, A. Smith, and N. Pryds. Review and comparison of magnet designs for magnetic refrigeration. *International Journal of Refrigeration*, 33(3):437–448, 2010.

[228] R. Wroblewski, K. Sielicki, and M. Leonowicz. Magnetocaloric properties of Ni49.9Mn19.6Cu5.7Ga24.8single crystal processed by Bridgman method with stationary crucible. *Materials Letters*, 218:83–85, 2018.

[229] V. Sokolovskiy, V. Buchelnikov, K. Skokov, O. Gutfleisch, D. Karpenkov, Yu Koshkid'Ko, H. Miki, I. Dubenko, N. Ali, S. Stadler, and V. Khovaylo. Magnetocaloric and magnetic properties of Ni2Mn1-xCuxGa Heusler alloys: An insight from the direct measurements and ab initio and Monte Carlo calculations. *Journal of Applied Physics*, 114(18), 2013.

[230] Zongbin Li, Zhenzhuang Li, Bo Yang, Yudong Zhang, Claude Esling, Xiang Zhao, and Liang Zuo. Large low-field magnetocaloric effect in a directionally solidified Ni50Mn18Cu7Ga25 alloy. *Intermetallics*, 88(December 2016):31–35, 2017.

[231] P. La Roca, L. Isola, Ph Vermaut, and J. Malarría. Relationship between grain size and thermal hysteresis of martensitic transformations in Cu-based shape memory alloys. *Scripta Materialia*, 135:5–9, 2017.

[232] V. V. Kokorin, L. E. Kozlova, and A. N. Titenko. Temperature hysteresis of martensite transformation in aging Cu-Mn-Al alloy. *Scripta Materialia*, 47(8):499–502, 2002.

[233] Prashanth Konda Gokuldoss, Sri Kolla, and Jürgen Eckert. Additive manufacturing processes: Selective laser melting, electron beam melting and binder jetting-selection guidelines. *Materials*, 10(6), 2017.

[234] O. A. Likhachev and Yu M. Koval. Hysteresis phenomena and their modelling in martensitic transformation thermodynamics. *Uspehi Fiziki Metallov*, 16(1):23–34, 2015.

[235] Tino Gottschall, Konstantin P. Skokov, Ramon Burriel, and Oliver Gutfleisch. On the S(T) diagram of magnetocaloric materials with first-order transition: Kinetic and cyclic effects of Heusler alloys. *Acta Materialia*, 107:1–8, 2016.

[236] Haile Yan. *Crystal structure, martensitic transformation crystallography, mechanical and magnetocaloric performance of Ni(Co)MnIn multifunctional alloys.* PhD thesis, University of Lorraine and Northeastern University, 2016.

[237] I. Ruiz-Larrea, A. López-Echarri, J. F. Gómez-Cortés, M. L. Nó, D. W. Brown, L. Balogh, T. Breczewski, and J. San Juan. Strain relaxation in Cu-Al-Ni shape memory alloys studied by in situ neutron diffraction experiments. *Journal of Applied Physics*, 125(8), 2019.

[238] Jian Liu, Tino Gottschall, Konstantin P Skokov, James D Moore, and Oliver Gutfleisch. Giant magnetocaloric effect driven by structural transitions. *Nature materials*, 11(7):620–6, 2012.

[239] K. P. Skokov, D. Yu Karpenkov, M. D. Kuz'Min, I. A. Radulov, T. Gottschall, B. Kaeswurm, M. Fries, and O. Gutfleisch. Heat exchangers made of polymer-bonded La(Fe,Si)13. *Journal of Applied Physics*, 115(17):2012–2015, 2014.

[240] A. Gebert, S. Roth, S. Oswald, and L. Schultz. Passivity of polycrystalline NiMnGa alloys for magnetic shape memory applications. *Corrosion Science*, 51(5):1163–1171, may 2009.

[241] Motohiko Suzuki, Makoto Ohtsuka, Minoru Matsumoto, Yasukazu Murakami, Daisuke Shindo, and Kimio Itagaki. Effect of aging time on shape memory properties of sputtered Ni-rich Ni2MnGa alloy films. *Materials Transactions*, 43(5):861–866, 2002.

[242] N. Jetta, N. Ozdemir, S. Rios, D. Bufford, I. Karaman, and X. Zhang. Phase transformations in sputtered Ni–Mn–Ga magnetic shape memory alloy thin films. *Thin Solid Films*, 520(9):3433–3439, feb 2012.

[243] Markus Chmielus, Cassie Witherspoon, Robert C. Wimpory, Andreas Paulke, Andŕ Hilger, Xuexi Zhang, David C. Dunand, and Peter Müllner. Magnetic-field-induced recovery strain in polycrystalline Ni-Mn-Ga foam. *Journal of Applied Physics*, 108(12):1–7, 2010.

[244] R.W. Overholser, Manfred Wuttig, and D.A. Neumann. Chemical ordering in Ni-Mn-Ga Heusler alloys. *Scripta Materialia*, 40(10):1095–1102, 1999.

[245] Le Zhou, Catherine Kammerer, Anit Giri, Kyu Cho, and Yongho Sohn. Microstructural Development and Ternary Interdiffusion in Ni-Mn-Ga Alloys. *Metallurgical and Materials Transactions A: Physical Metallurgy and Materials Science*, 46(12):5572–5587, 2015.

[246] Dean Snelling, Christopher Williams, and Alan Druschitz. A comparison of binder burnout and mechanical characteristics of printed and chemically bonded sand molds. *25th Annual International Solid Freeform Fabrication; An Additive Manufacturing Conference, SFF 2014*, pages 197–209, 2014.

[247] Dustin Gilmer, Lu Han, Eunice Hong, Derek Siddel, Alexander Kisliuk, Shiwang Cheng, Dan Brunermer, Amy Elliott, and Tomonori Saito. An in-situ crosslinking binder for binder jet additive manufacturing. *Additive Manufacturing*, 35(February):101341, 2020.

[248] Sandra Wieland and Sebastian Boris Hein. Metal powder extrusion of magnetocaloric heat exchanger structures. In *EuroPM 2018*, pages 1–6, Bilbao, Spain, 2018. European Powder Metallurgy Association.

[249] Vanessa Holzhäuser. BASF obtains exclusive rights to market magnetocaloric materials, oct 2013.

[250] Veronika Belusa. Prototype of Magnetocaloric Wine Cooler, jan 2015.

[251] O. Tegus, E. Brück, K. H.J. Buschow, and F. R. De Boer. Transition-metal-based magnetic refrigerants for room-temperature applications. *Nature*, 415(6868):150–152, 2002.

[252] Z. Q. Ou, G. F. Wang, S. Lin, O. Tegus, E. Brück, and K. H.J. Buschow. Magnetic properties and magnetocaloric effects in Mn1.2Fe 0.8P1-xGex compounds. *Journal of Physics Condensed Matter*, 18(50):11577–11584, 2006.

[253] D. T. Cam Thanh, E. Brück, N. T. Trung, J. C.P. Klaasse, K. H.J. Buschow, Z. Q. Ou, O. Tegus, and L. Caron. Structure, magnetism, and magnetocaloric properties of MnFe P1-xSixcompounds. *Journal of Applied Physics*, 103(7):2006–2009, 2008.

[254] Viktor Höglin, Johan Cedervall, Mikael Svante Andersson, Tapati Sarkar, Matthias Hudl, Per Nordblad, Yvonne Andersson, and Martin Sahlberg. Phase diagram, structures and magnetism of the FeMnP1-xSix-system. *RSC Advances*, 5(11):8278–8284, 2015.

[255] O. Tegus, Li Hong Bao, and Lin Song. Phase transitions and magnetocaloric effects in intermetallic compounds MnFeX (X=P, As, Si, Ge). *Chinese Physics B*, 22(3), 2013.

[256] M Chmielus, Y Krimer, A Mostafaei, E Stevens, and J Toman. Application WO 2018/218199 Al: Alignment of magnetic materials during powder deposition or spreading in additive manufacturing, 2020.

[257] E. Stevens, K. Kimes, V. Chernenko, P. Lazpita, A. Wojcik, W. Maziarz, and M. Chmielus. Direct laser deposition and homogenization of Ni-Co-Mn-Sn magnetoaloric materials. *Microscopy and Microanalysis*, 2018.

[258] Daniel R. Clymer, Jonathan Cagan, and Jack Beuth. Power-velocity process design charts for powder bed additive manufacturing. *Journal of Mechanical Design, Transactions of the ASME*, 139(10):1–7, 2017.

[259] Hossein Ghasemi-Tabasi, Jamasp Jhabvala, Eric Boillat, Toni Ivas, Rita Drissi-Daoudi, and Roland E. Logé. An effective rule for translating optimal selective laser melting processing parameters from one material to another. *Additive Manufacturing*, 36(August):101496, 2020.

[260] Sarah K. Everton, Matthias Hirsch, Petros I. Stavroulakis, Richard K. Leach, and Adam T. Clare. Review of in-situ process monitoring and in-situ metrology for metal additive manufacturing. *Materials and Design*, 95:431–445, 2016.

[261] Vivek Thampy, Anthony Y. Fong, Nicholas P. Calta, Jenny Wang, Aiden A. Martin, Philip J. Depond, Andrew M. Kiss, Gabe Guss, Qingfeng Xing, Ryan T. Ott, Anthony van Buuren, Michael F. Toney, Johanna Nelson Weker, Matthew J. Kramer, Manyalibo J. Matthews, Christopher J. Tassone, and Kevin H. Stone. Subsurface Cooling Rates and Microstructural Response during Laser Based Metal Additive Manufacturing. *Scientific Reports*, 10(1):1–9, 2020.

[262] Ke Xu, Yingguang Li, Changqing Liu, Xu Liu, Xiaozhong Hao, James Gao, and Paul G. Maropoulos. Advanced Data Collection and Analysis in Data-Driven Manufacturing Process. *Chinese Journal of Mechanical Engineering (English Edition)*, 33(1), 2020.